Springer Theses
Recognizing Outstanding Ph.D. Research

Xin Zhang

Multistate GTPase Control Co-translational Protein Targeting

Springer

Springer Theses

Recognizing Outstanding Ph.D. Research

For further volumes:
http://www.springer.com/series/8790

Aims and Scope

The series "Springer Theses" brings together a selection of the very best Ph.D. theses from around the world and across the physical sciences. Nominated and endorsed by two recognized specialists, each published volume has been selected for its scientific excellence and the high impact of its contents for the pertinent field of research. For greater accessibility to non-specialists, the published versions include an extended introduction, as well as a foreword by the student's supervisor explaining the special relevance of the work for the field. As a whole, the series will provide a valuable resource both for newcomers to the research fields described, and for other scientists seeking detailed background information on special questions. Finally, it provides an accredited documentation of the valuable contributions made by today's younger generation of scientists.

Theses are accepted into the series by invited nomination only and must fulfill all of the following criteria

- They must be written in good English.
- The topic should fall within the confines of Chemistry, Physics and related interdisciplinary fields such as Materials, Nanoscience, Chemical Engineering, Complex Systems and Biophysics.
- The work reported in the thesis must represent a significant scientific advance.
- If the thesis includes previously published material, permission to reproduce this must be gained from the respective copyright holder.
- They must have been examined and passed during the 12 months prior to nomination.
- Each thesis should include a foreword by the supervisor outlining the significance of its content.
- The theses should have a clearly defined structure including an introduction accessible to scientists not expert in that particular field.

Xin Zhang

Multistate GTPase Control Co-translational Protein Targeting

Doctoral Thesis for Chemistry accepted by
California Institute of Technology, Pasadena, CA, USA

Springer

Author
Dr. Xin Zhang
The Scripps Research Institute
North Torrey Pines Rd 10550
Mail Stop: BCC265, La Jolla
CA 92037
USA
e-mail: xinzhang@scripps.edu

Supervisor
Shu-ou Shan
Assistant Professor
Division of Chemistry and Chemical Engineering
California Institute of Technology
Pasadena, CA 91125
USA

ISSN 2190-5053
ISBN 978-1-4419-7807-3
DOI 10.1007/978-1-4419-7808-0
Springer New York Dordrecht Heidelberg London

e-ISSN 2190-5061
e-ISBN 978-1-4419-7808-0

Cover design: eStudio Calamar, Berlin/Figueres

Printed on acid-free paper

Springer is part of Springer Science+Business Media (www.springer.com)

Contents

Chapter 1
Introduction

We now know that almost every major biological process is controlled by protein assemblies composed of two or more proteins that interact with one another to exert their regulatory function [1]. These assemblies are called protein machineries because the way that they work at a microscopic scale resembles the way that machines work at a macroscopic scale. Underlying these highly controlled activities are the ordered conformational changes that take place in the protein components of the machineries. These conformational changes often lead to molecular events that drive efficient regulation of the biological processes.

One key process in protein biogenesis is cotranslational protein targeting [2]. This process transports roughly one-third of proteins in a cell's genome from cytoplasmic space to the membrane compartments. This process, like many others, is controlled by the protein machinery in which the protein components interact with one another. This machinery is composed primarily of the signal recognition particle (SRP) and its signal receptor (SR). In all cells, the SRP machinery carries out targeting of secretory and membrane proteins to the endoplasmic reticulum membrane in eukaryotic cells or to the plasma membrane in bacteria.

Although the SRP machinery varies widely in size and composition due to evolution, the functional core of the SRP machinery is well conserved in a variety of organisms. The center of the SRP is comprised of the universally conserved SRP54 guanosine 5′-triphosphatases (GTPases) in complex with the SRP RNA. The SRP receptor also contains a highly conserved SR GTPase (SRα) subunit that serves as a connector between the SRP and the cellular membrane. Thus, SRP and SR GTPases together form the center of the SRP machinery and provide exquisite spatial and temporal controls to the protein targeting process.

The SRP-dependent protein targeting process involves a series of highly ordered molecular events [3]. These events begin when a nascent polypeptide chain destined for the endoplasmic reticulum (ER) or the secretory pathway emerges from a translating ribosome. The signal sequence that specifies its cellular localization is recognized by the SRP. The ribosome nascent chain complex (RNC),

X. Zhang, *Multistate GTPase Control Co-translational Protein Targeting*,
Springer Theses, DOI: 10.1007/978-1-4419-7808-0_1,

herein denoted as cargo, is then directed to the cellular membrane by the interaction between the SRP and the SR. Upon arrival at the membrane, the conformation of the SRP–RNC complex switches from a cargo-loading mode to a cargo-releasing mode in which the RNC is unloaded from the SRP and passed on the protein conducting channel, or the translocon, on the membrane. After the cargo is released, the SRP dissociates from the SR to allow the cargo to be recycled in the next round of protein targeting. Meanwhile, the synthesis of the nascent polypeptide is finished and the nascent protein is either integrated into the membrane or translocated through the membrane to enter its journey to the destined cellular compartment.

SRP and SR GTPases together compose a class of noncanonical GTPases in comparison to the classical GTPases such as Ras, Gα, and EF-Tu [3]. They do not exhibit significant conformational changes among the apo, guanosine 5′-diphosphate (GDP)-bound and guanosine 5′-triphosphate (GTP)-bound states. Further, these GTPases bind to nucleotides weakly and exchange from GDP to GTP rapidly. However, free SRP and SR GTPases bound to GTP have a low basal activity to hydrolyze GTP because the key catalytic residues for GTP hydrolysis are not correctly aligned with the bound nucleotide. Instead, GTP binding enables the SRP and SR GTPases to form a thermodynamically stable heterodimeric complex. In this complex, the two GTPases reciprocally activate the GTP hydrolysis activity of one another by two to four orders of magnitude. Following GTP hydrolysis, the GDP-bound SRP–SR complex would lose its affinity and quickly dissociate to regenerate free SRP and SR GTPases for the next cycle.

Since the SRP and SR GTPase are intrinsically capable of multiple rounds of dimerization and GTP hydrolysis, it is of interest to understand how the complex assembly and GTPase activation are controlled so that these GTPase function as molecular switches to regulate the series of molecular events in space and time. The goal of this dissertation is to elucidate the "hidden facts" inside the SRP machinery that control the protein targeting process both efficiently and faithfully. In particular, most efforts have been made to understand how the SRP and SR interact with one another to coordinate the ordered series of molecular events during the protein targeting. Thus, the studies that were carried out in this dissertation focus on the molecular mechanism of the interaction between the SRP and the SR GTPases, and on how this interaction responds actively to the cues such as cargos and thus how this interaction helps maintain the efficiency and fidelity of the protein targeting process.

Chapter 2 [4] defines the kinetic and thermodynamic framework of the SRP–SR interaction. A transient, GTP-independent early intermediate during the assembly of a stable SRP–SR complex is discovered by a highly sensitive fluorescence assay in real time. This further demonstrates that the SRP–SR complex assembly is a complex process that involves at least two steps. In the initial step, an early, GTP-independent SRP–SR complex is formed via the fast association between the SRP and the SR. In the second step, the GTP-dependent conformational rearrangements precede the formation of a stable complex. The SRP RNA significantly stabilizes the early, GTP-independent intermediate. Further, mutational analyses show that

there is a strong correlation between the ability of the mutant SRP RNAs to stabilize the early intermediate and their ability to accelerate the SRP–SR complex formation. Thus, the SRP RNA is proposed to stabilize the transient early intermediate to give it a longer dwell time and therefore a higher probability to rearrange to the stable complex.

Chapter 3 defines the landscape of the transient intermediate during assembly of a stable SRP–SR complex. Direct structural characterization of an transient intermediate ensemble is challenging because the intermediate tends to either dissociate or rearrange to the stable complex. In this work, an ensemble of the SRP–SR early intermediate is generated by stalling the conformational rearrangements to form the stable complex. Thus, the structural properties of the early intermediate can be directly characterized under equilibrium condition. The interaction surface of the early intermediate is both similar to and different from that of the stable complex. Further, a nanosecond timescale experiment reveals a broad conformational distribution of the early intermediate. These conformational states allow the free SRP and SR GTPases to search the optimal routes in the configurational space toward an efficient assembly of the stable complex. Interestingly, the landscape of the early intermediate actively responds to the cargos, suggesting that the early intermediate could potentially serve as a control point to the protein targeting process.

Chapter 4 [5] focuses on how SRP machinery ensures the efficiency of the protein targeting reaction by examining the effect of cargos on the SRP–SR interaction. Since the conformational dynamics of the early intermediate actively responds to the cargos, I investigate how the cargos kinetically and thermodynamically modulate a series of discrete conformational rearrangements during the SRP–SR interaction. The cargo for SRP is found to accelerate the SRP–SR complex assembly by over two orders of magnitude, thereby driving rapid and efficient delivery of cargo to the membrane. A series of subsequent rearrangements in the SRP–SR GTPase complex switch the SRP from the cargo-binding mode to the cargo-releasing mode where the cargo can be unloaded during the late stages of protein targeting. Further, the cargo delays GTPase activation in the SRP–SR complex by an order of magnitude. The slower GTP hydrolysis in a RNC–SRP–SR complex creates an important time window that could further improve the efficiency of protein targeting. This work shows that the SRP and SR GTPases constitute a self-sufficient system that provides exquisite spatial and temporal control points to maintain the efficiency of protein targeting.

Chapter 5 answers how SRP machinery maintains the fidelity of the substrate selection in the protein targeting process. The “signal hypothesis” postulates that the signal sequence on a protein allows it to be specifically recognized by targeting factors such as SRP, which mediates the delivery of the protein to the correct cellular compartments. It was generally thought that fidelity arises from the inability of SRP to bind strongly to incorrect cargos. Instead, I show that incorrect cargos are further rejected through a series of fidelity checkpoints during subsequent steps of targeting, including complex formation between the SRP and the SR and kinetic proofreading through GTP hydrolysis. Thus, the SRP pathway achieves high fidelity of substrate selection through the cumulative effect of

multiple checkpoints; this principle may be generally applicable to other complex cellular pathways that need to recognize degenerate signals or discriminate between correct and incorrect substrates based on minor differences.

Overall, this dissertation establishes the framework of how the SRP machinery achieves an efficient and faithful co-translational protein targeting process. In particular, I show that the function of the SRP machinery is governed by a series of ordered conformational changes during the SRP–SR interaction that culminates in their GTPase activation. These conformational changes respond actively to the cargos so that they could provide discrete control points at which regulation can be exerted on the protein targeting process spatially and temporally. The paradigm provided in this dissertation adds to an increasing collection of knowledge on how critical biological processes are regulated by multistate protein machineries.

References

1. Alberts B (1998) Cell 92:291
2. Walter P, Johnson AE (1994) Annu Rev Cell Biol 10:87
3. Shan SO, Schmid SL, Zhang X (2009) Biochem 48:6696
4. Zhang X, Kung S, Shan SO (2008) J Mol Biol 381:581
5. Zhang X, Schaffitzel C, Ban N, Shan SO (2009) Proc Natl Acad Sci U S A 106:1754

Chapter 2
A Multistep Mechanism for Assembly of the SRP–SR Complex

2.1 Introduction

To maintain proper cellular function, a cell needs to efficiently and accurately deliver all its proteins to the different subcellular organelles. The signal recognition particle (SRP) and its receptor (SR) constitute a universally conserved machinery to deliver newly synthesized proteins from the cytoplasm to the eukaryotic endoplasmic reticulum (ER) membrane, or the bacterial plasma membrane [1–3]. The protein targeting reaction consists of several ordered steps that ensure the efficiency and fidelity of this process [4, 5]. At the beginning of the targeting cycle, the SRP recognizes translating ribosome that carries a signal sequence on the nascent chain. The SRP then forms a complex with SR localized on the target membrane; this process brings the ribosome–nascent chain complex (RNC) to the membrane surface. Upon arrival at the membrane, conformational changes in the SRP–SR complex drive the release of the RNC from the SRP to a protein conducting channel composed of the sec61p (or secYEG in bacteria) complex [6]. Once the RNC is released, the SRP and SR dissociate into free components, allowing a new round of the protein targeting reaction. Thus, the ordered assembly and disassembly of the SRP–SR complex control the delivery of proteins to their proper cellular destinations.

In eukaryotes, SRP is a universally conserved ribonucleoprotein complex consisting of six proteins and an SRP RNA [7–9]. The functional core of the SRP requires only two components: the conserved SRP54 protein in complex with the SRP RNA. The SRP54 (called Ffh in *E. coli*) is composed of two structurally and functionally distinct domains: a methionine-rich M domain and an NG domain. The M domain recognizes the signal sequences and binds the SRP RNA [10–14]. A GTPase, G-domain and an N-terminal four helix bundle (the N-domain) together

A version of this chapter has been published as Zhang X, Kung S, Shan S-O (2008) J Mol Biol 381:581–593

X. Zhang, *Multistate GTPase Control Co-translational Protein Targeting*,
Springer Theses, DOI: 10.1007/978-1-4419-7808-0_2,

form a structural and functional unit called the NG domain, which binds and hydrolyzes GTP and forms a complex with SR (called FtsY in bacteria) [15–18]. The NG domain was also suggested to play a role in signal peptide recognition [19]. The SRP and SR GTPases use a regulatory mechanism distinct from that of classical signaling GTPases such as Ras, Rho, and Ran [20]. The structure of both GTPases are similar regardless of whether GTP or GDP is bound [21–24]. Thus, the SRP and SR do not switch between active and inactive states depending on whether GTP or GDP is bound. Moreover, these GTPases bind nucleotides weakly and exchange nucleotides quickly, so that no external nucleotide exchange factors are required to switch these GTPases from the GDP- to the GTP-bound state [25]. In addition, the SRP and SR reciprocally stimulate each other's GTPase activity upon formation of the SRP–SR complex [17]. Therefore, no external GTPase activating proteins are required to regulate the switch of these GTPases from the GTP- to the GDP-bound state. Instead, recent biochemical and biophysical analyses suggest that several discrete conformational changes occur during the binding and reciprocal activation between the two proteins, and each of these conformation may provide a potential point for regulation during the protein targeting reaction [5, 6].

The SRP RNA has been shown to play an indispensable role in protein targeting both in vitro and in vivo [26–31]. The size of the SRP RNA varies widely from bacteria to yeast and mammalian cells; nevertheless, the most phylogenetically conserved region of the SRP RNA, domain IV, has been maintained in all three kingdoms of life [32, 33]. The role of SRP RNA may involve recognition and binding of the ribosome and signal sequences [11, 26, 34], and stabilization of the folding of the M-domain. In addition, it was also proposed to bind to and stabilize the NG domain of Ffh [35]. Intriguingly, kinetic analyses of the role of the 4.5S SRP RNA on the GTPase cycles of Ffh and FtsY showed that the RNA also plays a critical role in the interaction between the two GTPases [17, 25]. In the absence of the SRP RNA, Ffh-FtsY association is extremely slow, with a rate constant of $5 \times 10^3\ M^{-1}\ s^{-1}$, and the SRP RNA accelerates their association kinetics by 400-fold [17, 25, 36]. An additional step, GTP hydrolysis after the complex is formed, is also enhanced eightfold by the 4.5S RNA [25]. Thus, the presence of the SRP RNA brings the interaction kinetics between the SRP and SR to an appropriate range for their biological functions. The SRP RNA contains a highly conserved GNRA tetraloop that was shown to be essential for the interaction between the SRP and SR. Tetraloop mutants were reported to impair the binding between SRP and SR, cause a reduction in the GTPase activity of the SRP–SR complex, as well as fail to support normal cell growth in vivo [27, 30]. A site-directed hydroxyl radical probing study further suggest that the tetraloop is located close to the heterodimer interface of the SRP–SR GTPase complex [37].

To probe the conformational dynamics during the SRP–SR interaction and to elucidate how the SRP RNA exerts its catalytic role on SRP–SR complex assembly, we developed a highly sensitive FRET assay to monitor the interaction between the SRP and SR in real time. This new assay led to the discovery of a new SRP–SR complex that forms independently of GTP. This GTP-independent

complex has been observed only once in a surface-resonance experiment using mammalian SRP and SR [38]. Further characterization identifies this GTP-independent complex as an early intermediate during the initial stage of the SRP–SR interaction. Formation of the early intermediate is substantially stabilized by the 4.5S RNA, and 4.5S RNA tetraloop mutants that fail to stabilize this intermediate also fail to accelerate SRP–SR complex assembly. We propose that the catalytic role of 4.5S RNA on complex assembly can be explained by its stabilizing effect on the early intermediate, which increases its probability to rearrange to the final, GTP-stabilized complex.

2.2 Results

To characterize the conformational dynamics during the SRP–SR interaction, we developed a real time assay based on fluorescence resonance energy transfer (FRET). The basic strategy is to engineer a single cysteine residue on cysteine-less Ffh and FtsY proteins, and label the single cysteines with thio-reactive fluorescent probes (Fig. 2.1a). In Ffh, the intrinsic cysteine at position 406 can be replaced with serine without disrupting its function [37, 39]. A cysteine was introduced at position 153 of cysteine-less Ffh and labeled with maleimide-coumarin (DACM) as the FRET donor. FtsY does not contain any cysteine residue; thereby a cysteine was introduced at position 345 and labeled with maleimide-BODIPY-fluorescein (BODIPY-FL) as the FRET acceptor. These probes are close to the nucleotide binding pocket in the G domains of both proteins, and are 31 Å apart as estimated from the crystal structure of the *Thermus aquaticus* Ffh–FtsY complex (Fig. 2.1a) [16]. The cysteine mutation and fluorescence labeling do not alter the ability of Ffh and FtsY to bind and activate each other's GTPase activity (Fig. 2.2), nor do they affect their ability to translocate model SRP substrates into ER microsomal membranes.

2.2.1 A GTP-Independent Complex is Detected by the FRET Assay

Previous studies have shown that SRP and SR form a stable complex in the presence of GTP or non-hydrolyzable GTP analogues such as 5′-guanylylimidodiphosphate (GppNHp), with dissociation constants of 16–30 nM [17]. As expected, a significant amount of FRET was observed upon assembly of the SRP–SR complex in the presence of GppNHp (Fig. 2.1b). At saturating protein concentrations, the FRET efficiency was 0.80 (Fig. 2.3a), in good agreement with the distance between the two residues in the crystal structure and the Förster radius of this donor–acceptor pair. To our surprise, when GppNHp was either removed from the reaction mix or replaced by GDP, efficient FRET was also observed (Fig. 2.1c), suggesting that an SRP–SR complex can be formed independently of GTP.

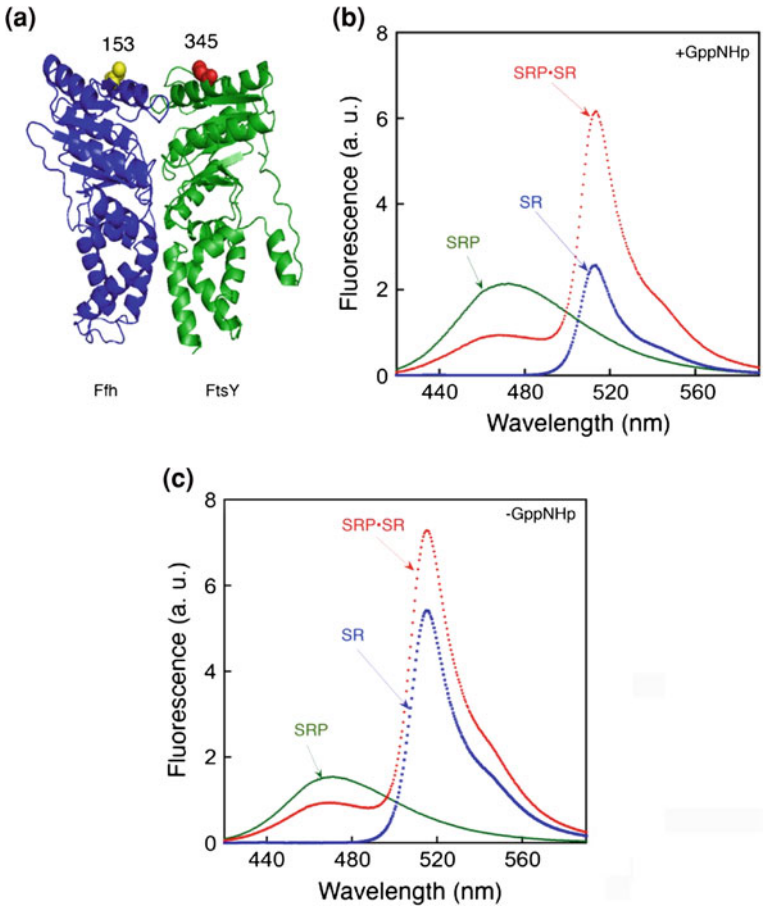

Fig. 2.1 SRP and SR can form a complex independently of GTP. **a** Position of FRET donor (*yellow circles*) and acceptor (*red circles)* probes on the SRP (Ffh) and SR (FtsY) on a co-crystal structure of the Ffh–FtsY complex [16]. **b** Fluorescence emission spectrum of SRP–SR complex in the presence of 100 microM GppNHp. 0.5 microM SRP and 2 microM SR were incubated for 10 min at 25 °C to form the SRP–SR complex (*red*). SRP- and SR-only spectra (*green* and *blue*, respectively) were obtained by incubating fluorescently labeled SRP (or SR) with unlabeled SR (or SRP). **c** Fluorescence emission spectrum of SRP–SR complex in the absence of GppNHp. 5 microM SRP and 15 microM SR were incubated at 25 °C for 10 min. SRP or SR-only spectra were obtained as in **b**

The affinities of the GTP-dependent and GTP-independent complexes were measured by equilibrium titration. The dissociation constant of the complex formed in the presence of GppNHp was determined to be 16 nM using this FRET assay (Fig. 2.3a, circles), consistent with previous studies [17]. In contrast, a dissociation constant of 4–10 microM was observed for the complex assembled in the presence of GDP or no nucleotide (Fig. 2.3a, squares and triangles,

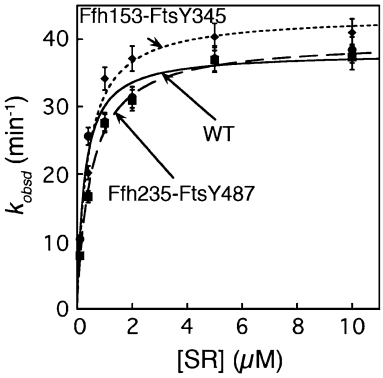

Fig. 2.2 Reciprocally stimulated GTPase activity between SRP and FtsY are unaffected in fluorescently labeled proteins. The reaction rate constants were measured and analyzed as described in Materials and Methods using 100 nM SRP and 100 microM GTP. The maximal GTP hydrolysis rate constants at saturating protein concentrations are 37.9, 42.2, and 38.9 min^{-1} for wild-type (*solid line*), Ffh 153C and FtsY 345C (*dotted line*), and Ffh 235C and FtsY 487C (*broken line*), respectively

respectively). Thus, the γ-phosphate of GTP contributes over 250-fold to the stability of the SRP–SR complex. In these titration experiments, the FRET value at saturating protein concentrations represent the FRET efficiency of the two probes in their respective complexes: the GTP-independent complex has a FRET efficiency of 0.62, which is $\sim$25% lower than that of the GTP-dependent complex (0.80). The different FRET values suggest that these two complexes have different conformations in which the donor and acceptor fluorophores are positioned or oriented differently. Similar results were observed when another FRET pair was engineered near the N-domain of each protein (Fig. 2.4).

In addition to equilibrium measurements, we also determined the kinetics for assembly and disassembly of the GTP-independent complex by following fluorescence emission from the FRET donor over time. The time course for assembly of the GTP-independent complex fits well to single exponential kinetics (Fig. 2.5, blue); plots of the observed rate constant against the concentration of SR gave an association rate constant k_{on} of 5.7 $\pm$ 0.5 $\times$ 10^6 M^{-1} s^{-1} (Fig. 2.3b). This is over 50 times faster than the association kinetics for formation of the GTP-dependent complex previously determined [17]. The dissociation rate constant of the GTP-independent complex is 60 $\pm$ 6 s^{-1} (Fig. 2.3c), which is 2 $\times$ 10^4-fold faster than that of the GTP-dependent complex [17]. Thus in addition to the lower equilibrium stability, the GTP-independent complex is also kinetically much less stable than the GTP-dependent complex previously characterized [17]. This explains why this complex was not observed previously based on gel filtration analyses [16], which can only detect kinetically stable complexes.

The following observations strongly suggest that the GTP-independent complex is not an artifact introduced by dye labeling: (1) the FRET value is dependent on

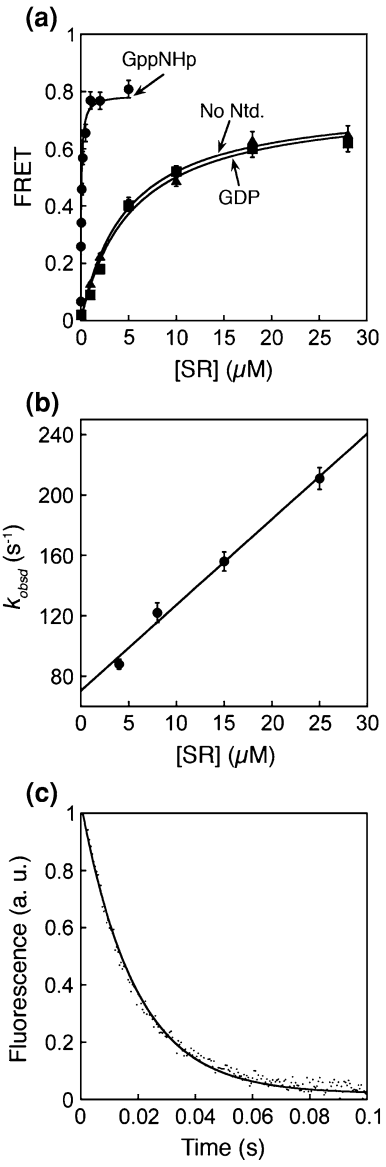

Fig. 2.3 Stability and kinetics for formation of the GTP-independent complex. **a** Equilibrium titration of SRP–SR complex with GppNHp (*closed circles*), GDP (*closed squares*), and without nucleotide (*closed triangles*). The data were fit to a single binding equation and gave dissociation constants of 16 nM (GppNHp), 4 microM (GDP) and 4.2 microM (no nucleotide). **b** Association kinetics of GTP-independent complex was measured as described in Materials and Methods. Values of observed rate constants were plotted against SR concentration and a linear fit of the data gave an association rate constant of 5.6×10^6 M^{-1} s^{-1}. **c** Dissociation kinetics was determined in a pulse-chase experiment described in Materials and Methods. The data were fit to a single exponential equation and gave a dissociation rate constant of 60 s^{-1}

protein concentration and is saturable, suggesting that the FRET signal arises from complex formation, rather than nonspecific interactions between the dyes; (2) FRET from the GTP-independent complex can be competed away by unlabeled protein (Fig. 2.3c); and (3) SR labeled with an environmentally sensitive probe (acrylodan) on position 242 also showed a fluorescence change when the complex was formed in GDP. Thus, FRET provides a robust and highly sensitive assay that allows us to detect, for the first time, a transient GTP-independent SRP–SR

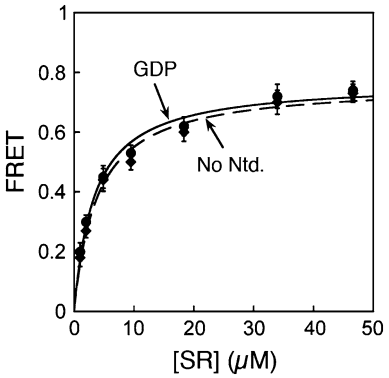

Fig. 2.4 Equilibrium titration of SRP–SR (Ffh 235C and FtsY 487C) complex with 100 microM GDP (*closed circles*), and without nucleotide (*closed diamonds*). The data were fit to a single binding equation and gave dissociation constants of 3.9 microM (GDP) and 3.6 microM (without nucleotide)

complex that has a different conformation than that observed previously for the GTP-dependent complex.

2.2.2 The GTP-Independent Complex Represents a Transient Intermediate on the Pathway for Formation of the GTP-Stabilized Complex

In this section we provide two lines of evidence that strongly suggest that the GTP-independent complex is an on-pathway intermediate preceding the formation of the GTP-dependent complex: (1) an intermediate can be directly detected in the time course for formation of the GTP-dependent complex, and the kinetics for formation of this intermediate agrees with the kinetics for assembly of the GTP-independent complex, and (2) stabilization of the GTP-independent intermediate by the SRP RNA also accelerates the rate for formation of the final, GTP-dependent complex, consistent with the notion that the GTP-independent complex in an on-pathway intermediate.

The first piece of evidence was obtained from comparison of the kinetics of complex formation in the presence or absence of GppNHp. To ensure that low affinity intermediates can accumulate and be detected, we used a high concentration of SR during complex assembly, and fluorescence emission from the FRET donor was followed over time. The time course for complex formation in the presence of GppNHp exhibits bi-phasic kinetics (Fig. 2.5a, red), indicating that there are at least two steps involved in the assembly of the GTP-dependent complex. The first kinetic phase is dependent on SR concentration (Fig. 2.5b), and therefore represents fast, bimolecular association between SRP and SR to form an intermediate that has a lower FRET value. The second kinetic phase is concentration independent (Fig. 2.5c) and thus represents the unimolecular rearrangement of this intermediate to a complex that has a higher FRET value. Remarkably, the

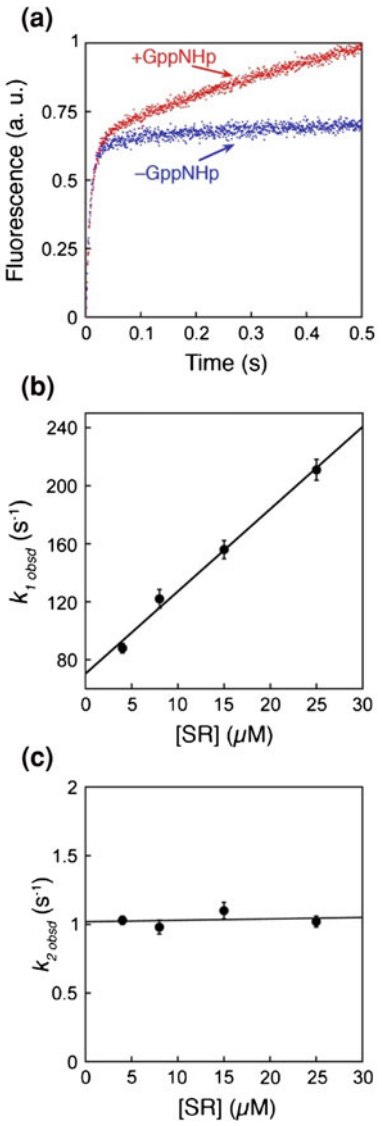

Fig. 2.5 Formation of an SRP–SR complex in the presence of GppNHp involves two discrete steps. **a** Comparison of the time courses for complex formation in the absence (*blue*) and presence of 100 microM GppNHp (*red*). Data were obtained with 4 microM SRP and 8 microM SR. **b** The observed rate constants of the first kinetic phase during SRP-SR association in the presence of GppNHp were plotted against SR concentration. A linear fit of the data gave an association rate constant of $5.8 \times 10^6\ M^{-1}\ s^{-1}$ (k_1 in Scheme 2.1). **c** The observed rate constants of the second kinetic phase during SRP–SR association in the presence of GppNHp are independent of SR concentration. The average of these rate constants is $1.03\ s^{-1}$ (k_2 in Scheme 2.1)

rate constant of the first kinetic phase coincides very well with that for formation of the GTP-independent complex (Fig. 2.5a, blue), with observed rate constants of 118 and 122 s^{-1} at 8 microM SR (Fig. 2.5a). This strongly suggests that the GTP-independent complex is the intermediate observed in the first kinetic phase during complex assembly in the presence of GppNHp. In contrast to the biphasic kinetic behavior during assembly of the GTP-dependent complex, formation of the GTP-independent complex does not have a second kinetic phase (Fig. 2.5a, blue),

$$\text{SRP} + \text{SR} \underset{k_{-1}}{\overset{k_1}{\rightleftharpoons}} \textit{early}\ \text{intermediate} \overset{k_2}{\rightleftharpoons} \textit{closed}, \text{stable complex}$$

Scheme 2.1 Schematic representation of the two-step SRP-SR interaction

suggesting that the rearrangement represented in the second kinetic phase is strictly GTP-dependent.

A classical criterion for an on-pathway intermediate is that stabilization of the intermediate accelerates the reaction to form the final product. This criterion was satisfied by the effects of the 4.5S SRP RNA on the GTP-independent and GTP-dependent complexes. The GTP-independent complex could not be formed in the absence of the 4.5S RNA (Fig. 2.6a), even after long periods of incubation when equilibrium had been reached (Fig. 2.6b). Thus, the 4.5S RNA increases the equilibrium stability of the GTP-independent complex. In contrast, it was shown that a stable GTP-dependent Ffh–SR complex can be formed with or without the 4.5S RNA, but the RNA accelerates the association rate of this complex by 200 fold (cf. Figs. 2.6c and 2.6d) [17]. The results presented here and in the next section show that there is a strong correlation between the ability of the 4.5S RNA to stabilize the GTP-independent complex and its ability to accelerate formation of the GTP-dependent complex. This provides independent evidence that the GTP-independent complex is an on-pathway intermediate. If the GTP-independent complex were off the pathway, then its stabilization by the 4.5S RNA would compromise formation of the native complex in the presence of GppNHp.

Taken together, these results demonstrate that formation of the GTP-stabilized SRP–SR complex involves at least two steps (Scheme 2.1): (1) GTP-independent bi-molecular association between the SRP and SR to form a transient intermediate (referred to as the early intermediate); and (2) GTP-dependent rearrangement of the early intermediate to form the stable complex previously observed. As demonstrated previously, additional conformational stages are present even after the stable complex is formed (Fig. 2.7) [5]. Thus, the interaction between the SRP and SRP receptor is a highly dynamic process involving multiple conformational changes during complex assembly and activation.

2.2.3 Defects of Mutant 4.5S RNAs in Formation of the Early Intermediate Correlates with Defects in Accelerating SRP–SR Complex Formation

The observation that the 4.5S RNA can stabilize the early intermediate suggests that the RNA may exert its catalytic effect on SRP–SR complex formation by prolonging the lifetime of the intermediate, thereby increasing its probability to rearrange to the final stable complex. If this were true, then mutant RNAs that are defective in accelerating SRP–SR complex formation would also be predicted to

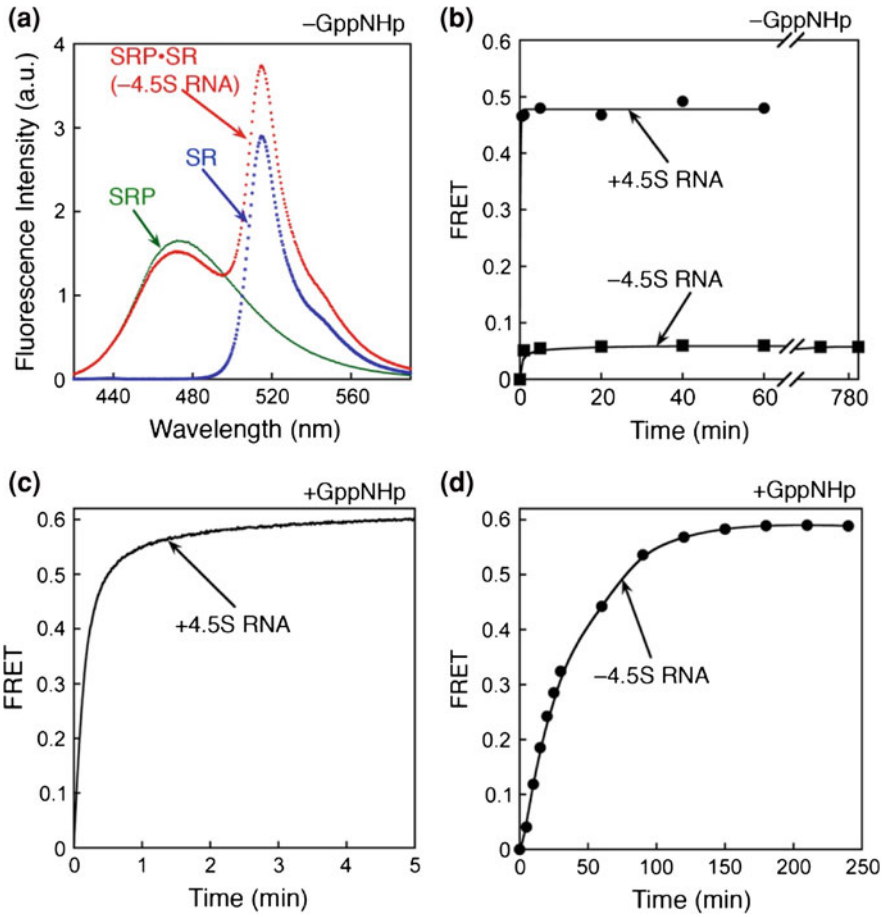

Fig. 2.6 The GTP-independent complex is stabilized by the 4.5S RNA. **a** Spectrum of the GTP-independent complex in the absence of 4.5S RNA. The experiment setup is the same as in Fig. 2.1c except that the 4.5S RNA was not included. **b** Formation of the GTP-independent complex was monitored in the presence (*closed circles*) and absence (*closed squares*) of the 4.5S RNA. **c**, **d** The time course for formation of the GTP-dependent complex was monitored in the presence (**c**) and absence (**d**) of 4.5S RNA. In **c**, 0.5 microM SRP and 2 microM SR were used. In **d**, 2 microM Ffh and 10 microM SR were used to obtain a faster reaction rate. Note the difference in time scales in **c** and **d**

be defective in stabilizing the early intermediate. To test this model, we reexamined mutations in the universally conserved GGAA tetraloop of SRP RNA (Fig. 2.8a) that have previously been shown to impair formation of the SRP–SR complex [27, 30].

To this end, eight tetraloop mutants were constructed with various base substitutions: GNRA-type, UNCG-type and mutations that do not form a tetraloop

(Fig. 2.8a). Mutant RNAs were assembled into SRPs with Ffh under the same conditions as wild-type 4.5S RNA, as previous results have shown that mutations in the RNA tetraloop does not affect its ability to bind Ffh [27, 30]. Although the effects of these mutations on SRP–SR complex have been characterized before, the earlier study described these effects as a deficiency in forming a stable SRP–SR complex [30]. However, kinetic analyses subsequently showed that a stable Ffh–SR complex can be formed without the SRP RNA; the role of RNA is to accelerate the kinetics of complex formation [17]. Therefore, we recharacterized these RNA tetraloop mutants to test whether the defects arise from altered kinetics or stability of complex formation.

We first analyzed SRP–SR complex formation using the well-characterized GTPase assay; stimulation of the GTPase activity in the SRP–SR complex provides a convenient assay for protein–protein interactions. In this assay, the rate constants of two molecular events can be measured. First, at low concentrations of SR, the reaction is rate limited by SRP-SR association to form an activated SRP–SR complex. Therefore the slope of the initial linear portion of the concentration dependence, which represents the reaction: SRP + SR → products (k_{cat}/K_M), is equal to the rate constant for formation of a stable, active complex. Second, at saturating protein concentrations, the reaction is rate-limited by a different step, the activated GTP hydrolysis after a stable SRP–SR is formed. Therefore, the rate constant at saturating FtsY concentrations, k_{cat}, represents the rate constant of GTP hydrolysis from the activated SRP–SR complex. Most of the tetraloop mutants show defects in the rate of complex formation (k_{cat}/K_M, Fig. 2.8b–d and Table 2.1). Moderate mutants GAAA, UGAA, and GUAA exhibit 8- to 15-fold defects (bold in Table 2.1 and blue in Fig. 2.8) and severe mutants CUUC, GUCG, GAAU, and UUCG exhibit 45- to 224-fold defects (italic in Table 2.1 and red in Fig. 2.8). GUUG is the only neutral mutant that exhibits no functional defect in this assay (green in Fig. 2.8). In contrast, most of the mutant RNAs do not significantly impair the activated GTPase reaction in the SRP–SR complex (k_{cat}, Fig. 2.8b and Table 2.1), with some mutants exhibiting even higher GTPase activity than wild-type SRP. Only the most severe mutants GAAU and UUCG showed a modest reduction (1.8- and 1.2-fold, respectively) in the stimulated GTPase activity. These data showed that the primary defect of the RNA tetraloop mutants is the slower kinetics to form the SRP–FtsY complex.

We also used the FRET assay to independently determine the effect of mutant RNAs on formation of the GTP-dependent SRP–SR complex. Consistent with the results from the GTPase assay, mutant SRPs form GTP-dependent complexes with SR much more slowly than wild-type SRP (Fig. 2.9a). In addition, the FRET assay directly demonstrates that SRP–SR complexes can be formed with the mutant RNAs, given that sufficient time is provided to allow complex formation.

We then tested whether the mutant RNAs can allow formation of the GTP-independent early intermediate using the FRET assay (Fig. 2.9b). The severe mutants GAAU, CUUC, GUCG, and UUCG, which cause the most deleterious defect on the assembly rate of the GTP-dependent SRP–SR complex, also severely block the formation of the GTP-independent early intermediate, with the observed

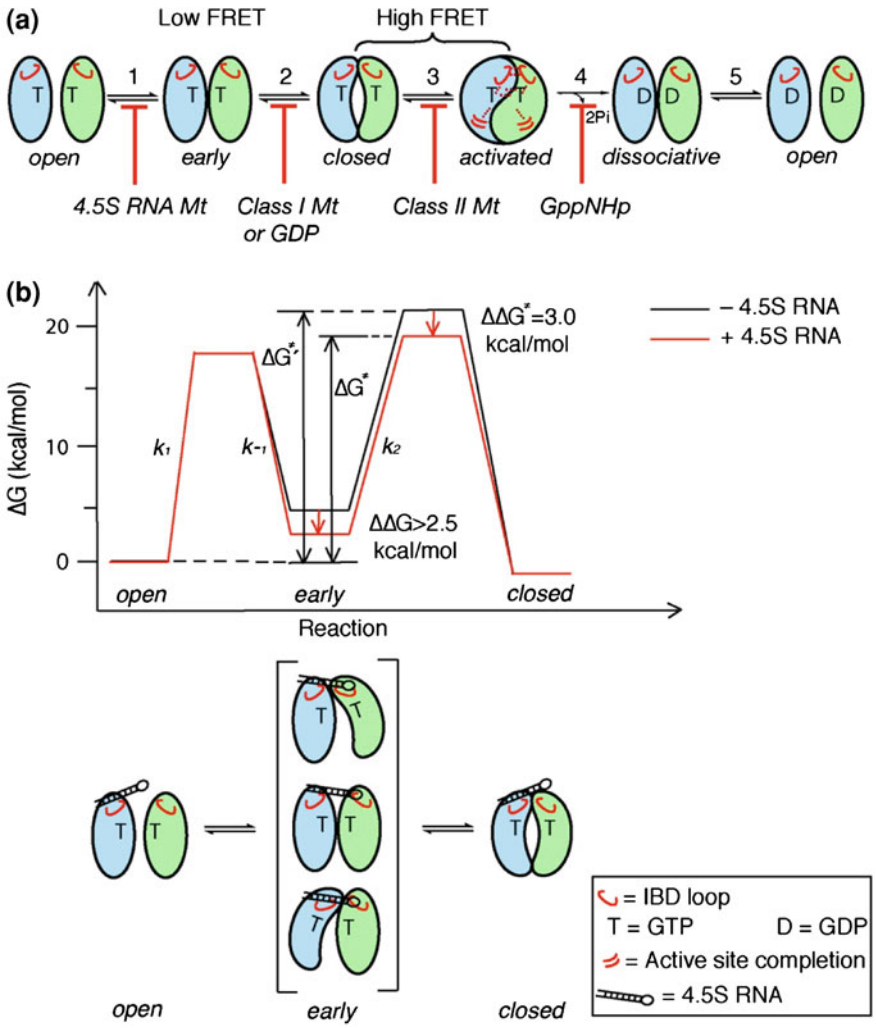

Fig. 2.7 Multiple conformational changes during SRP–SR complex formation and activation. **a** SRP and SR GTPases form an early GTP-independent intermediate that exhibits a low FRET (step 1). In the presence of GTP, early rearranges to a more stable, *closed* complex that exhibits a high FRET (step 2). Additional rearrangements in the catalytic loops activate GTP hydrolysis (step 3). GTP hydrolysis drives the dissociation of the SRP–SR complex (steps 4 and 5). Each step can be blocked using specific mutants or nucleotides. 4.5S RNA tetraloop mutants block formation of the early intermediate. Class I mutants of SR [5] or GDP blocks formation of a *closed* complex. Class II mutants on SRP or SR [5] block the rearrangement that activates GTP hydrolysis. GppNHp blocks the chemical step. **b** Top panel: free energy profile for the SRP–SR interaction in the absence (*black*) and presence (*red*) of the 4.5S RNA for a standard state of 200 nM. Activation energies were calculated from the observed association and dissociation rate constants using $\Delta G = -RT \ln(kh/k_B T)$, where $R = 1.987$ cal K^{-1} mol^{-1}, $-h = 1.58 \times 10^{-37}$ kcal s^{-1}, $k_B = 3.3 \times 10^{-27}$ kcal K^{-1}, and $T = 298$ K. The relative energies of the different complexes were calculated from the observed equilibrium stabilities using $\Delta G = -RT \ln K$. The 4.5S RNA

◀ **Fig. 2.7** (continued)
stabilizes the early intermediate (in bracket) by > 2.5 kcal mol^{-1}, and the overall activation energy is subsequently lowered by ~ 3 kcal mol^{-1}. $\Delta G^{\neq}$ and $\Delta G^{\neq\prime}$ defines the overall activation energy for forming the GTP-stabilized complex with and without RNA, respectively. The bottom panel depicts a physical picture of how the 4.5S RNA exerts its effect on the SRP–SR interaction as described in the text

FRET efficiency similar to that in the absence of 4.5S RNA (Fig. 2.9b, red). Slightly higher FRET efficiencies are observed with moderate mutants UGAA, GUAA, and GAAA (blue), indicating partial formation of the GTP-independent early intermediate at the concentration used in this experiment. In contrast, the neutral mutant GUUG (green) formed the GTP-independent complex as efficiently as the wild type SRP. Due to the very weak affinity of the GTP-independent complex formed by the mutant RNAs (>50 microM), saturation could not be reached in equilibrium titration experiments to measure the stabilities of these complexes. Nevertheless, the results in Fig. 2.9b show that the GTP-independent complex is substantially destabilized by mutations in the tetraloop of the 4.5S RNA. Further, there is a strong correlation between the defects of RNA mutants in stabilizing the GTP-independent early intermediate and their defects in accelerating the assembly rate of the GTP-stabilized, final SRP–SR complex (cf. Fig. 2.9b vs Fig. 2.8d).

If stabilization of the early intermediate and efficient SRP–SR complex formation are essential for protein targeting, then the mutant RNAs would be predicted to also impair the protein targeting reaction. To test this notion, we measured the efficiency of protein targeting mediated by the mutant RNAs using a heterologous, co-translational protein targeting assay based on the model SRP substrate preprolactin (pPL) [6, 40]. As shown in Fig. 2.10, most of the mutant RNAs also exhibit translocation defects. The severe mutants (red), which impair complex formation by over 50-fold, completely block pPL translocation. The moderate mutants (blue), which reduce the SRP–SR interaction kinetics by about 15-fold, caused a more modest ($\sim 20\%$) reduction in translocation efficiency. The small translocation defect caused by the moderate mutants is presumably due to the limited sensitivity of this targeting assay, as it can detect translocation defect only when the SRP–SR interaction is reduced by more than 20-fold [6]. In contrast, the neutral mutant GUUG does not significantly affect protein translocation. Thus there is also a good correlation between the translocation defect and the degree to which complex formation is blocked by each mutant RNA (cf. Figs. 2.8d, 2.9b, and 2.10; see also Table 2.1).

2.3 Discussion

In this study, we developed a highly sensitive, real time FRET assay that allows us to detect a transient, GTP-independent early intermediate during assembly of a stable SRP–SR complex. This demonstrates that SRP–SR complex assembly is

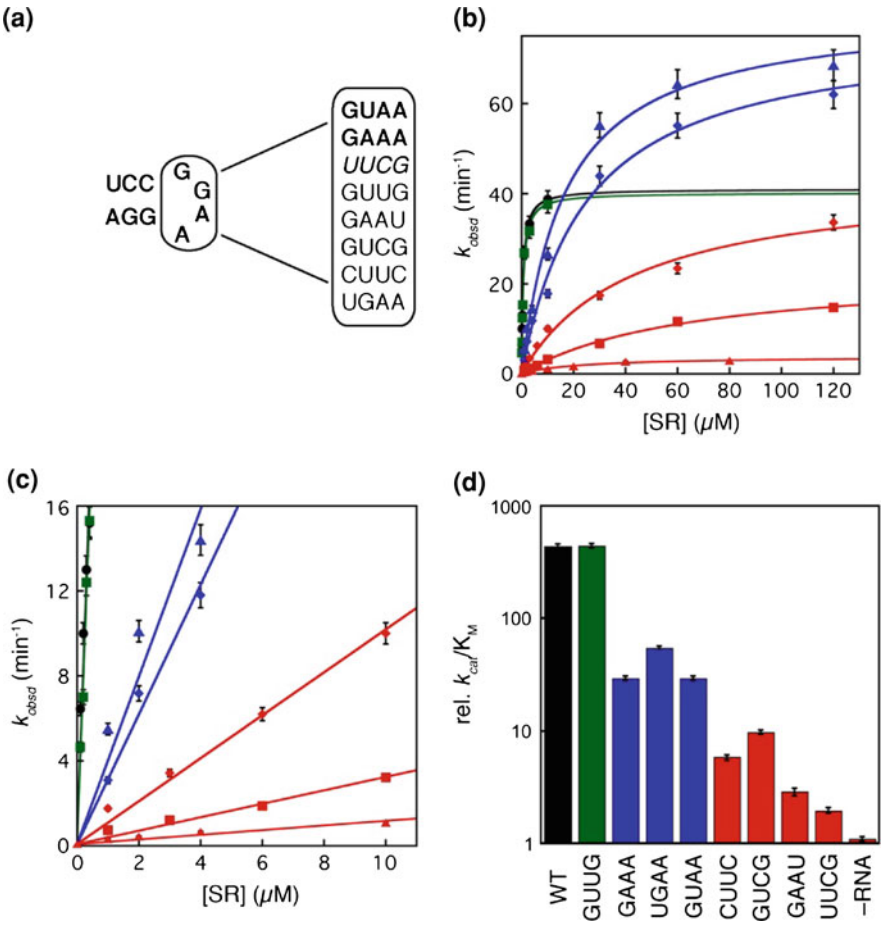

Fig. 2.8 Tetraloop mutants in 4.5S RNA slows down the assembly rate of an active SRP–SR complex. **a** List of tetraloop mutants studied in this work. GAAA and GUAA form GNRA type tetraloops (shown as *bold*); UUCG forms a UNRG type tetraloop (shown as *italics*); GUUG, GAAU, UCGA, CUUC and UGAA do not form a tetraloop (shown as *normal*). **b**, **c** Tetraloop mutants in the 4.5S RNA were classified into three classes based on the severity of defects in SRP-SR association (refer to the classification in Table 2.1). The GTPase reaction rate constants were measured and analyzed as described in Materials and Methods using 100 nM SRP and 100 microM GTP [wild-type (*closed black circles*), GUUG (*closed green squares*), UGAA (*closed blue triangles*), GAAA (*closed blue diamonds*), GUCG (*closed red diamonds*), UUCG (*closed red squares*), and no RNA (*closed red triangles*)]. The initial linear portion of **b** is expanded in **c** to show the difference in k_{cat}/K_M of the various RNA mutants. The values of k_{cat}/K_M and k_{cat} for each RNA are listed in Table 2.1. **d** Comparison of k_{cat}/K_M values for the various RNA mutants. Data were from **c**

a complex multi-step process. Intriguingly, this early intermediate is substantially stabilized by the 4.5S SRP RNA, and there is a strong correlation between the abilities of mutant RNAs to stabilize this early intermediate and their abilities to

Table 2.1 Summary of mutational effects of tetraloop mutants in the 4.5S RNA

Tetraloop mutant	k_{cat}/K_M, rel[a]	Translocation efficiency (%)	k_{cat} (min^{-1})	FRET
Wild type	439	55	40.9	0.40
GUUG	439	46	38.7	0.34
GAAA	29.2	37	76.4	0.12
UGAA	54.9	38	81.9	0.15
GUAA	29.2	38	80.6	0.11
CUUC	5.8	12	35.8	0.06
GUCG	9.8	14	44.3	0.07
GAAU	2.9	11	23.0	0.08
UUCG	1.9	8	33.8	0.05
No RNA	1	8	3.8	0.05

Three classes of mutants are classified based on the severity of the defect as defined in the text

[a] Relative value of k_{cat}/K_M compared to that of the no-RNA reaction

accelerate the assembly of the stable SRP–SR complex. This led us to propose a new model in which the SRP RNA exerts its catalytic effect on SRP–SR complex assembly through stabilizing a transient intermediate, thereby allowing it more dwell time to rearrange into the GTP-stabilized final complex. The presence of this additional conformational step provides another potential point for regulation in the protein targeting reaction.

Previous studies have established that GTP or non-hydrolyzable GTP analogues are required for formation of a stable SRP–SR complex, but no complexes have been observed in the absence of GTP [17, 25, 41–43]. In this study, FRET provides a highly sensitive assay that allows us to observe an unstable SRP–SR complex in solution that can be formed independently of GTP. Only Mandon et al. have reported a mammalian SRP–SR complex formed in GDP in surface-resonance measurements [38]. This complex was not observed in solution previously, presumably because previous studies have relied on gel filtration analysis [16] or the use of tryptophan fluorescence [17, 25, 44]. Gel filtration chromatography can only observe kinetically stable complexes but will not be able to detect a more transient complex. Tryptophan fluorescence relies on a late conformational change in FtsY that accompanies complex formation [17], but could miss earlier steps. In contrast, the FRET assay is able to detect transient complexes, because FRET signal relies only on the distance approximation and relative orientation of the donor and acceptor fluorophores on the two proteins. We also showed that the FRET value is different for the GTP-independent complex from the stable, GTP-dependent complex; thus these two complexes have different conformations. Finally, this assay allows us, for the first time, to quantitatively evaluate the contribution of the g-phosphate group to complex stability. The presence of the g-phosphate of GTP stabilizes the SRP–SR complex by over 250-fold; the actual interaction energy of the proteins with the g-phosphate group is presumably larger, as a significant amount of the interaction energy has to be used to induce conformational changes in the complex [5, 16].

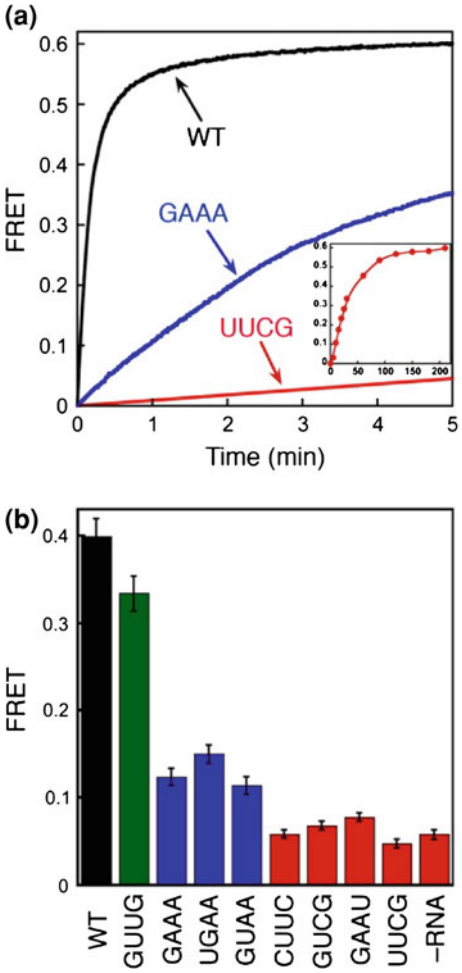

Fig. 2.9 FRET measurement shows the deficiency in SRP–SR complex formation caused by 4.5S RNA tetraloop mutants. **a** Time course for formation of the GTP-dependent complex in the presence of different RNA mutants. The *inset* shows the data over a longer time course with the UUCG mutant (time scale in minutes). 0.5 microM SRP (2 microM SRP for UUCG mutant) and 2 microM SR (10 microM SR for UUCG) were used in the experiment in the presence of 100 microM GppNHp. **b** FRET measurement of the extent of formation of the GTP-independent complex with various 4.5S RNA mutants. 4 microM SRP and 16 microM SR were incubated without GppNHp

For the SRP-subfamily of GTPases, the structural difference between the GppNHp-, GDP-, and apo-proteins is rather minimal [21, 23, 45–47]. It is therefore reasonable to suspect that the conformation of the GTP-independent complex can also be adopted by GTP-bound SRP and SR. Here we provide several lines of

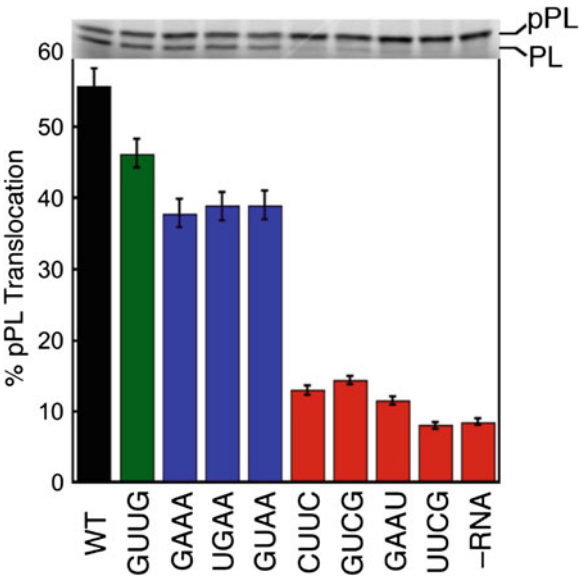

Fig. 2.10 Tetraloop mutants impair the co-translational translocation of pre-prolactin. The translocation efficiencies were determined and analyzed as described in Materials and Methods. Top panel shows the SDS–PAGE analysis of the translocation of ^{35}S-labeled prolactin. pPL and PL indicate the precursor and mature form of prolactin

evidence that strongly suggest that the GTP-independent complex represents an intermediate on the pathway to formation of the final, stable complex by GTP-bound SRP and SR. First, the time course for complex formation in the presence of GppNHp exhibits bi-phasic kinetics indicative of a two-step process, and the first kinetic phase agrees well with the kinetics for formation of GTP-independent complex. Second, the 4.5S RNA is shown to thermodynamically stabilize the GTP-independent complex and also accelerate formation of a GTP-stabilized complex. This observation is consistent with the classical criterion for an on-pathway intermediate: stabilization of an on-pathway intermediate should accelerate the reaction to form the final product. In contrast, if the GTP-independent complex were off-pathway, then stabilizing this complex would be expected to inhibit formation of the GTP-dependent complex. Together, these observations provide strong evidence that the GTP-independent complex is an early intermediate that precedes a GTP-dependent rearrangement to form the final, GTP-dependent complex. The omission of GTP provides a convenient means to isolate this intermediate by preventing the subsequent conformational rearrangements, thereby characterizing its kinetic, thermodynamic, and structural properties and its roles in the protein targeting reaction.

Previously, mutational analysis of the SRP–SR complex have isolated multiple classes of mutant GTPases that each block a different stage during the SRP–SR interaction: class I mutants are defective in complex formation; class II mutants primarily block reciprocal GTPase activation; class III mutants impair both steps; and class IV mutants specifically affect activation of one GTPase in the complex

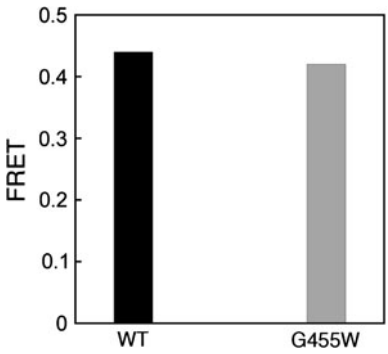

Fig. 2.11 Formation of the GTP-independent complex for wild type SR and a Class I mutant SR G455W [5]. FRET values were measured with 4 microM SRP and 16 microM wild type or mutant SR in the absence of nucleotides

[5]. The results with these mutants suggest that during the SRP–SR interaction, complex formation and activation of GTP hydrolysis in the individual GTPases are discrete and separable steps. Our results here further showed that assembly of a stable complex is also a multi-step process that involves an additional GTP-independent early intermediate. Together, these results emphasize the dynamic nature of the SRP–SR interaction. The fact that this early intermediate is much less stable than the previously characterized complexes, and that the class I mutant SR (G455W), which blocks formation of a stable complex, does not affect the formation of the early intermediate (Fig. 2.11), indicates that the early intermediate precedes formation of the closed complex.

The model in Fig. 2.7a describes the multiple steps during the SRP-SR binding and activation cycle. The free SRP and SR, predominantly in an inactive, *open* conformation, quickly associate with one another to form a transient, GTP-independent early intermediate (Fig. 2.7a, step 1). Interactions of both proteins with the GTP g-phosphate allow this complex to rearrange into a stable closed complex (step 2). Activation of GTP hydrolysis in the complex requires an additional local rearrangement of the conserved insertion box domain loops from both SRP and SR that precisely aligns the catalytic residues in the loop with respect to both GTP molecules (step 3). GTP hydrolysis then generates a GDP-complex (step 4), which quickly disassembles due to its low kinetic stability (step 5).

Notably, the early intermediate formed in the first step is significantly stabilized by the 4.5S SRP RNA. Unlike the purely kinetic effect of this RNA on formation of the stable SRP–SR complex (i.e., both complex formation and disassembly is accelerated by the same 200- to 400-fold without affecting the equilibrium stability of the complex) [17, 25], the RNA *thermodynamically* stabilizes the early intermediate. Further, mutations in the conserved tetraloop of the 4.5S RNA are defective in stabilizing the early intermediate, and this defect strongly correlates with the defect of these RNA mutants in accelerating formation of the final, stable SRP–SR complex. Judging from the FRET efficiency of the GTP-independent intermediate in the absence of the RNA, we estimate that the RNA exerts

a >60-fold stabilizing effect on this intermediate; this effect accounts for a large part of the ~200-fold acceleration of SRP–SR complex assembly by the RNA.

These data allow us to propose a new model for how the 4.5S RNA catalyzes both the association and dissociation between SRP and SR (Fig. 2.7b). We propose that the early intermediate, although forms quickly, does not have sufficient contacts between the two proteins and thus disassembles just as quickly. The 4.5S SRP RNA, by stabilizing the early intermediate, could provide this intermediate a longer lifetime during which each protein searches the conformational space and attempts to rearrange to the correct conformation for interacting with each other (Fig. 2.7b, lower panel). The subsequent rearrangement of the early intermediate to the closed complex is the rate-limiting step for formation of a stable SRP–SR complex (Fig. 2.7b, $DG^{\ddagger}$ and $DG^{\ddagger\prime}$ represents the free energy barrier for formation of the final complex with and without the RNA, respectively). Even if the RNA do not provide additional transition state stabilization for the early → closed rearrangement and the same barrier remains for this rearrangement with or without the RNA present, the overall energy barrier for formation of the stable complex is reduced, thus leading to an accelerated assembly rate (Fig. 2.7b). This model explains how the SRP RNA accelerates assembly of the Ffh–SR complex without affecting its equilibrium stability [17]. Several previous models have been proposed to account for the catalytic effect of the RNA by suggesting that the RNA preorganizes the conformation of Ffh to allow a better interaction with SR; however, such models predict that the stability of the Ffh–SR complex would also be increased by the SRP RNA and are not consistent with experimental data.

Although we provide here an energetic model to explain the catalytic role of the 4.5S RNA, the structural origin of this effect remains to be determined. Most likely, the SRP RNA provides a transient tether that holds the two GTPases together upon their initial encounter (Fig. 2.7b). This tether is broken after rearrangement to the final stable SRP–SR complex since the RNA does not stabilize this stable complex [17], and as such, it has been difficult to identify these transient interactions that the RNA makes with the GTPase domains. Since the thermodynamic stability of the early intermediate directly affects the overall energy barrier of the assembly reaction instead of characterizing the transition state, we can conveniently characterize the structural and energetic properties of the early intermediate to identify molecular interactions made by the 4.5S RNA to exert its catalytic role.

The presence of the early intermediate and an additional conformational rearrangement required to form the *closed* complex provides an additional potential point for regulation in the protein targeting reaction. In solution, the initial collisional encounter of the SRP and SR leads to a transient and unstable early intermediate that would not accumulate under cellular conditions. In the presence of spatial and temporal cues such as cargo binding and membrane localization, it is possible that the kinetic and thermodynamic stability of this early intermediate and its subsequent rearrangement can be altered and serves to coordinate the proper binding and release of cargo during the protein targeting reaction.

2.4 Materials and Methods

2.4.1 Material

Eschericia coli Ffh, FtsY and 4.5S RNA were expressed and purified using established procedures [25]. Mutant proteins and RNAs were constructed using QuickChange procedure (Stratagene, La Jolla, CA), and were expressed and purified by the same procedure as that for wild-type proteins and RNAs. Fluorescent dyes DACM and BODIPY-FL were purchased from Invitrogen (Carlsbad, CA).

2.4.2 Fluorescence Labeling

Single-cysteine mutants of Ffh and FtsY were labeled with maleimide derivatives of coumarin and BODIPY-FL, respectively. Protein was dialyzed in labeling buffer [50 mM KHEPES (7.0), 300 mM NaCl, 2 mM EDTA)] and treated with 2 mM TCEP to reduce the disulfide bonds. The labeling reaction was carried out using a fivefold excess of dye over protein for over 2 h at 4 °C, and stopped by adding 2 mM DTT. Excess dye was removed by gel filtration using Sephadex G-25 (Sigma, CA). Absorbance of DACM ($e_{363} = 27{,}000\ M^{-1}\ cm^{-1}$) and BODIPY-FL ($e_{504} = 79{,}000\ M^{-1}\ cm^{-1}$) was used to determine the concentration of labeled protein. The efficiency of labeling reaction was evaluated using

$$I = \frac{\text{moles of dye}}{\text{moles of proteins}}. \tag{2.1}$$

The efficiency of labeling reaction was typically ≥95% for both probes. The background, estimated from the labeling of cysteinless Ffh and FtsY using the same procedure, are less than 3%.

2.4.3 Fluorescence Measurement

FRET was determined by steady-state fluorescence measurement on a Fluorolog-3 spectrofluorometer (Jobin–Yvon, Edison, NJ). All measurements were carried out at 25 °C in assay buffer [50 mM KHEPES, pH 7.5, 150 mM KOAC, 2 mM $Mg(OAc)_2$, 2 mM DTT, 0.01% Nikkol] using an excitation wavelength of 380 nm. Fluorescence emission spectra were acquired from 420 to 600 nm. Equilibrium titration or kinetic measurements using FRET were determined by monitoring the fluorescence emission at 470 nm. FRET efficiency (E) is calculated by the relative fluorescence intensities of the donor in the presence and absence of acceptor (Eq. 2.2),

$$E = 1 - F_{DA}/F_D. \quad (2.2)$$

where F_{DA} and F_D are the fluorescence intensities of the donor measured in the presence and in the absence of acceptor, respectively. F_D was measured using donor-labeled Ffh and unlabeled FtsY. The Förster distance for the donor–acceptor pair coupled to the different positions was experimentally determined to be $R_0 \sim 47$ Å [48]. Fast reactions were measured on a Kintek stop-flow apparatus at 25 °C. The association rate constant for the SRP–SR complex was measured by mixing 2 microM SRP with 4, 8, 15, 25 microM SR in the presence or absence of GppNHp. The observed rate constant (k_{obsd}) is linearly dependent on SR concentration (Eq. 2.3) and the slope of the concentration dependence gives the association rate constant, k_{on} [17].

$$k_{obsd} = k_{on}[SR] + k_{off}. \quad (2.3)$$

The dissociation rate constant for the GTP-independent complex (k_{off}) was determined by a pulse-chase experiment [25]. 2 microM SRP and 8 microM SR were incubated in the absence of GppNHP for 5 min to form the SRP–SR complex, then the solution was mixed with equal volume of 400 microM unlabeled SR to drive irreversible dissociation of the complex. The time course of change in donor fluorescence was fit to exponential function (Eq. 2.4), where F_{obsd} is the observed fluorescence, $F_{t\to\infty}$ is the fluorescence when reaction reaches equilibrium, and ΔF is the amount of fluorescence change during the experiment.

$$F_{obsd} = F_{t\to\infty} + \Delta F \times e^{-k_{off}t}. \quad (2.4)$$

2.4.4 Translocation Assay

Mutant 4.5S RNAs were used to reconstitute SRP with Ffh, and protein targeting efficiency of the mutant SRPs were measured using a heterologous co-translational translocation assay as described [6, 40].

2.4.5 GTPase Assay

The GTPase assay to measure the stimulated GTP hydrolysis reaction between SRP and FtsY were carried out and analyzed as described [25].

Acknowledgments We thank members of the Shan Laboratory for comments on the manuscript. This work was supported by NIH grant GM078024 to S.S. S.S. was supported by the Burroughs Wellcome Fund career award, the Henry and Camille Dreyfus foundation, the Beckman Young Investigator award, and the Packard and Lucile award in science and engineering. X.Z. was supported by a fellowship from the Ulric B. and Evelyn L. Bray Endowment Fund.

References

1. Walter P, Johnson AE (1994) Annu Rev Cell Biol 10:87
2. Matlack KES, Mothes W, Rapoport TA (1998) Cell 92:381
3. Johnson AE, van Waes MA (1999) Annu Rev Cell Dev Biol 15:799
4. Shan SO, Walter P (2005) FEBS Lett 579:921
5. Shan SO, Stroud RM, Walter P (2004) PLoS Biol 2:1572
6. Shan SO, Chandrasekar S, Walter P (2007) J Cell Biol 178:611
7. Walter P, Ibrahimi I, Blobel G (1981) J Cell Biol 91:545
8. Walter P, Blobel G (1981) J Cell Biol 91:551
9. Walter P, Blobel G (1981) J Cell Biol 91:557
10. Batey RT, Rambo RP, Lucast L, Rha B, Doudna JA (2000) Science 287:1232
11. Keenan RJ, Freymann DM, Walter P, Stroud RM (1998) Cell 94:181
12. Krieg UC, Walter P, Johnson AE (1986) Proc Natl Acad Sci U S A 83:8604
13. Kurzchalia TV et al (1986) Nature 320:634
14. Zopf D, Bernstein HD, Johnson AE, Walter P (1990) EMBO J 9:4511
15. Connolly T, Rapiejko PJ, Gilmore R (1991) Science 252:1171
16. Egea PF et al (2004) Nature 427:215
17. Peluso P et al (2000) Science 288:1640
18. Powers T, Walter P (1995) Science 269:1422
19. Cleverley RM, Gierasch LM (2002) J Biol Chem 277:46763
20. Bourne HR, Sanders DA, Mccormick F (1991) Nature 349:117
21. Gawronski-Salerno J, Coon JSV, Focia PJ, Freymann DM (2007) Proteins 66:984
22. Focia PJ, Gawronski-Salerno J, Coon JS, Freymann DM (2006) J Mol Biol 360:631
23. Freymann DM, Keenan RJ, Stroud RM, Walter P (1999) Nat Struct Biol 6:793
24. Freymann DM, Keenan RJ, Stroud RM, Walter P (1997) Nature 385:361
25. Peluso P, Shan SO, Nock S, Herschlag D, Walter P (2001) Biochem 40:15224
26. Gu SQ et al (2005) RNA-Publ RNA Soc 11:1374
27. Siu FY, Spanggord RJ, Doudna JA (2007) RNA 13:240
28. Sagar MB, Lucast L, Doudna JA (2004) RNA 10:772
29. Brown S, Fournier MJ (1984) J Mol Biol 178:533
30. Jagath JR et al (2001) RNA-Publ RNA Soc 7:293
31. Zheng N, Gierasch LM (1997) Mol Cell 1:79
32. Poritz MA, Strub K, Walter P (1988) Cell 55:4
33. Poritz MA et al (1990) Science 250:1111
34. Batey RT, Sagar MB, Doudna JA (2001) J Mol Biol 307:229
35. Hainzl T, Huang S, Sauer-Eriksson AE (2007) Proc Natl Acad Sci U S A 104:14911
36. Stroud RM, Walter P (1999) Curr Opin Struct Biol 9:754
37. Spanggord RJ, Siu F, Ke AL, Doudna JA (2005) Nat Struct Mol Biol 12:1116
38. Mandon EC, Jiang Y, Gilmore R (2003) J Cell Biol 162:575
39. Buskiewicz I et al (2005) J Mol Biol 351:417
40. Powers T, Walter P (1997) EMBO J 16:4880
41. Connolly T, Gilmore R (1989) Cell 57:599
42. Rapiejko PJ, Gilmore R (1992) J Cell Biol 117:493
43. Zopf D, Bernstein HD, Walter P (1993) J Cell Biol 120:1113
44. Jagath JR, Rodnina MV, Wintermeyer W (2000) J Mol Biol 295:745
45. Padmanabhan S, Freymann DM (2001) Structure 9:859
46. Ramirez UD et al (2002) J Mol Biol 320:783
47. Focia PJ, Alam H, Lu T, Ramirez UD, Freymann DM (2004) Proteins 54:222
48. Lakowicz JR (1999) Principles of fluorescence spectroscopy. Kluwer Academic/Plenum Publishers, London

Chapter 3
Direct Visualization Reveals Dynamics of a Transient Intermediate During Protein Assembly

3.1 Introduction

Interactions between proteins are central to biology and underlie numerous molecular recognition, regulation, and signaling events [1–5]. A challenge in our understanding of protein interactions is to reconcile their fast association kinetics required for biological function (10^6–10^8 M^{-1} s^{-1}) with the fact that formation of stable protein assemblies often involves extensive short-range, stereospecific interactions that are difficult to accomplish during a single diffusional encounter [2, 3, 5, 6]. This problem becomes more pronounced in protein interactions that require extensive conformational changes in the interaction partners. Much theoretical work has suggested that assembly of a protein complex initiates with the formation of a transient intermediate held together by solvent cage and long-range electrostatic attractions, followed by relative rotatory diffusions of the binding partners to search for the optimal interaction interface with shape and electrostatic complementarity [4, 5, 7, 8]. Formation of transient intermediates reduces the dimension of translational and rotational search and could significantly accelerate protein association.

Nevertheless, direct experimental demonstration of this model is limited, and the structural and dynamic nature of transient intermediates during protein interactions remains elusive. Experimental studies of transient intermediates are still at the infant stage, because by definition, transient intermediates have short lifetimes and are rarely populated at equilibrium. Pioneering NMR studies have characterized rare conformational states in equilibrium with the predominant structure in the apoprotein or the final complex [9–16], and provided experimental support for the ability of proteins to explore different conformations during their interaction.

A version of this chapter has been published as Zhang X, Lam VQ, Mou Y, Kimura T, Chung J, Chandrasekar S, Winkler JR, Mayo SL, Shan S (2011) Direct visualization reveals dynamics of a transient intermediate during protein assembly. Proc Natl Acad Sci U S A 108:6450–6455

X. Zhang, *Multistate GTPase Control Co-translational Protein Targeting*,
Springer Theses, DOI: 10.1007/978-1-4419-7808-0_3,

Nevertheless, many of these studies have focused on protein interactions that are inherently weak and nonspecific; whether the same principle applies to the assembly of a stable and stereospecific protein complex remain unclear. Further, the transient species probed in this manner do not necessarily represent on-pathway intermediates that lead to the formation of final complexes. To understand the protein assembly pathway, it is crucial that on-pathway intermediates during protein assembly can be isolated. To this end, we chose the interaction between the signal recognition particle (SRP) and the SRP receptor (SR) as a model system.

3.2 Results and Discussion

Interaction between SRP and SR is mediated by contacts between the NG domains (comprised of a GTPase, G-domain and a helical N-domain) of both proteins (Fig. 3.1a). Rapid assembly of a stable SRP–SR complex is required to efficiently deliver cargo proteins to cellular membranes during co-translational protein targeting, and is essential for proper protein localization in all cells [17, 18]. However, free SRP and SR are not in the optimal conformation to bind one another, and extensive rearrangements must occur in both proteins to attain a stable complex [19]; this poses a challenge for achieving fast assembly kinetics. Previous kinetic studies showed that stable SRP–SR complex assembly begins with the formation of a transient "early" intermediate (Fig. 3.1a, step 1), which forms quickly ($k_{on} = 5.8 \times 10^6\ M^{-1}\ s^{-1}$) but is highly unstable ($K_d \sim 4$–$10\ \mu M$ and $k_{off} \sim 62\ s^{-1}$) [20]. This intermediate then slowly rearranges ($k_2 \sim 1.5\ s^{-1}$) to form the final stable complex, which is stabilized by a large, continuous interaction surface between the G- and N-domains (Fig. 3.1a, left panel and step 2) [20]. Importantly, complex assembly can be stalled at the early intermediate stage by leaving out guanosine 5′-triphosphate (GTP) (Fig. 3.1a) while maintaining the kinetic competence of this intermediate [20]. This allowed us to isolate this intermediate and characterize its structural, dynamic, and energetic features.

We first asked whether the early intermediate forms the same or distinct interaction interface compared to the stable complex. To this end, electron paramagnetic resonance (EPR) spectroscopy was used to probe the interaction surface [21]. Based on the co-crystal structure of the stable SRP–SR NG-domain complex, we selected residues in the vicinity of the interaction surface on SR for replacement by cysteine, which allowed site-directed spin labeling with the nitroxide probe (1-oxy-2,2,5,5-tetramethyl-3-pyrrolinyl-3-methyl) methanethiosulfonate (MTSSL). Only the sites where cysteine replacement and nitroxide labeling did not substantially affect the SRP-SR interaction were used for EPR measurements (Fig. 3.2). The residues on or near the dimer interface are likely to undergo significant changes in spin probe mobility upon complex formation, which are measured by the linewidth of the central resonance (Figs. 3.1b and 3.3, ΔH_0) and the overall breadth of the EPR spectra along the magnetic field axis [21]. To validate this approach, we first characterized the interaction surface of the stable complex formed with a non-

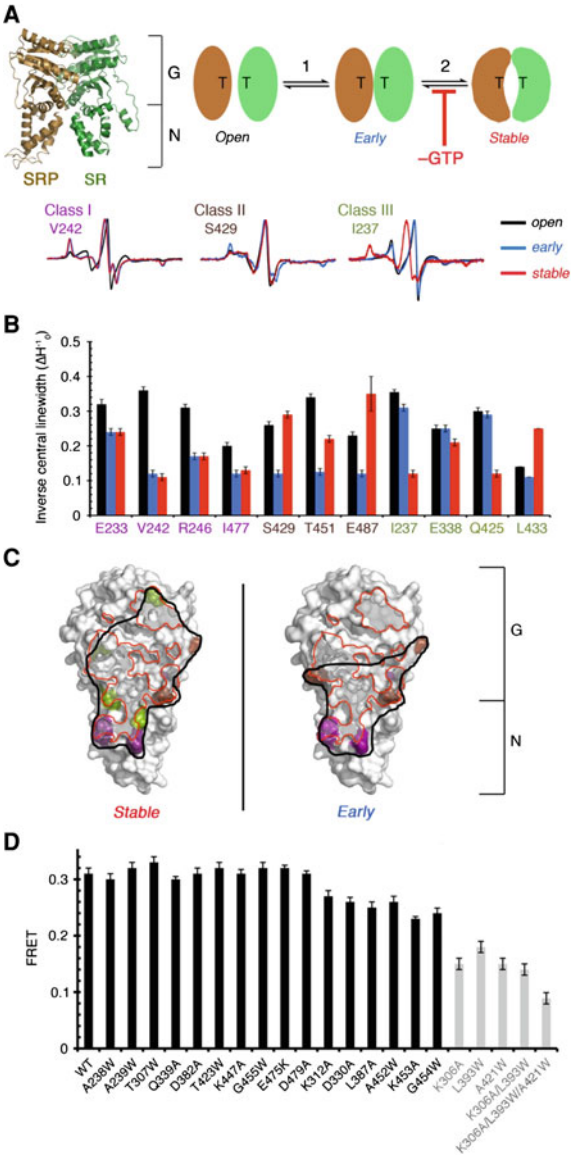

Fig. 3.1 The interface of the SRP-SR early intermediate overlaps with, but is distinct from that of the stable complex. **a** Left: crystal structure of the SRP–SR NG-domain complex (1JR9). Right: a multi-step mechanism for SRP–SR complex assembly involving formation of an early intermediate (step 1), and subsequent rearrangement to form the stable complex (step 2). Removal of GTP stalls the complex at the early intermediate stage. T denotes GTP. **b** Nitroxide spin probes labeled at specific SR residues change mobility upon formation of the early intermediate (*brown*), the stable complex (*green*), or both (*purple*). **c** Interaction surface of the early intermediate and stable complex mapped by EPR measurements. **d** Mutations that disrupt the stable complex did not significantly affect the stability of the early intermediate

hydrolyzable GTP analogue, 5′-guanylylimido-diphosphate (GMPPNP). Ten residues underwent significant EPR spectral changes upon complex formation (Figs. 3.1b and 3.3, red vs. black); collectively, they provided a view of the interaction surface in the stable complex (Fig. 3.1c left panel, dark outline) that is consistent with the co-crystal structure (Fig. 3.1c, red outline) [19]. This validated EPR as a powerful tool to identify the interaction surface of the complex.

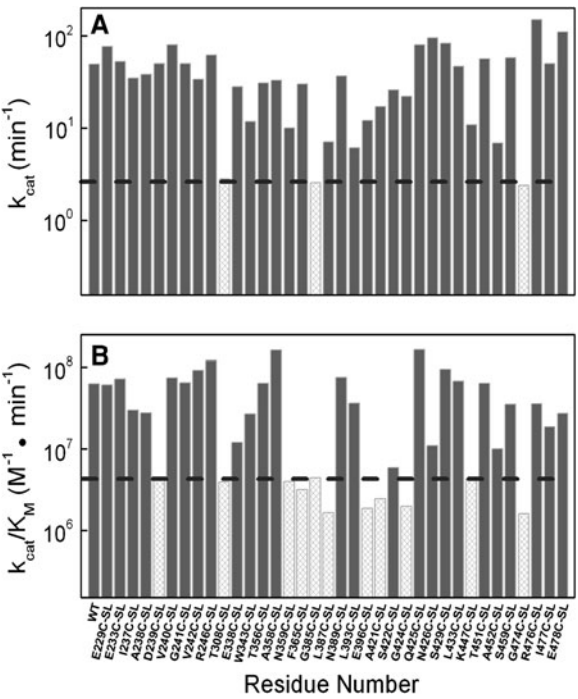

Fig. 3.2 Spin-labeled SR were screened using the GTPase assay. The activities of spin-labeled (SL) SR's in interaction with SRP were analyzed using the GTPase assay (see Materials and Methods). Two kinetic parameters were assessed: the GTPase rate constants of the SRP–SR complex (k_{cat} in **a**) and the association rate constants for stable SRP–SR complex assembly (as determined by k_{cat}/K_m in **b**; see Materials and Methods). Spin-labeled SR's that were defective in either property by a factor of 5 3 or more were not used for EPR studies (*open bars*). Spin-labeled SR's that were functional in interacting with SRP (grey bars) were used for EPR measurements

We next used this approach to map the interface of the early intermediate. Three classes of residues were identified that underwent distinct EPR spectral changes upon formation of the early or closed complex (Fig. 3.1b). Residues in class I, represented by V242 (Figs. 3.1b and 3.3, purple), underwent similar reductions in spin probe mobility upon formation of both the early and stable complexes, suggesting that they are involved in the interface of both complexes. Residues in class II, represented by S429 (Figs. 3.1b and 3.3, brown), underwent substantial immobilization of the spin probe in the early intermediate but these probes became more mobile in the stable complex, suggesting that they are more extensively involved in the formation of the early intermediate. Residues in class III, represented by I237 (Figs. 3.1b and 3.3, green), exhibited substantial changes in spin probe mobility only in the stable complex, suggesting that they are specifically involved in the formation of the stable complex. Collectively, seven residues (class I and II) underwent substantial spectral changes upon formation of the early intermediate (Fig. 3.1b, residues colored purple and brown), which provided a view of the interaction surface of this intermediate (Fig. 3.1c right panel, dark outline). In contrast to the stable complex, many residues engaged in the dimer interface of the early intermediate were in the N-domain. Thus this intermediate has a detectable interaction surface that overlaps with, but is distinct from that of the stable complex (Fig. 3.1c).

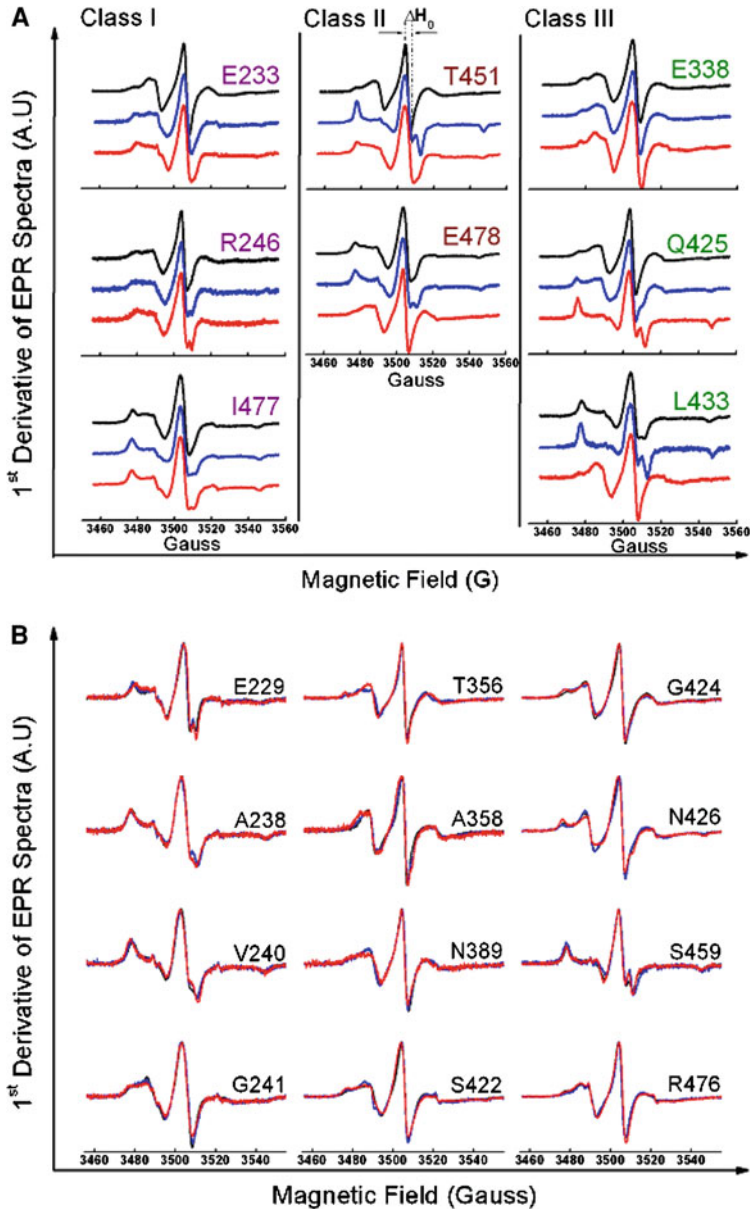

Fig. 3.3 The mobility of spin labels on SR changed upon formation of the early intermediate (class II), stable complex (class III), or both (class I). **a** EPR spectra of additional spin probes in SR that changed mobility upon complex formation. *Black*, *blue* and *red* denote the free protein, the early intermediate, and the stable complex, respectively. The mobility of spin label was analyzed from the central line width (ΔH_0) and the breadth of the spectra, and are summarized in **b**. **b** EPR spectra of spin probes in SR that exhibited no significant changes in mobility upon formation of either the early intermediate or the stable complex. Color-coding is the same as in **a**

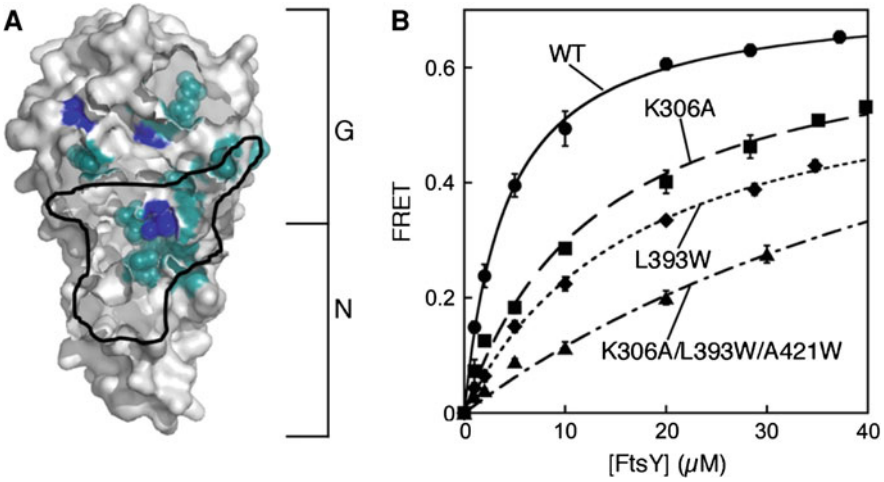

Fig. 3.4 Mutants that disrupt formation of the stable complex caused only moderate defects in the stability of the early intermediate. **a** Positions of the SR mutants (*cyan* and *blue*) studied in this work are shown on the surface representation of the SR. The three moderately defective mutants are highlighted in *blue*. The *black line* outlines the interaction surface of the early intermediate mapped by EPR spectroscopy. **b** The stabilities of the early intermediates formed by mutant SRs were determined by equilibrium titrations. Fits to Eq. 3.2 gave K_d values of 4.1 μM for wild-type SR, 13.2 μM for SR (K306A), 17.3 μM for SR (L393W), and 31.3 μM for SR (K306A:L393W:A421W)

To independently identify the interaction surface of the early intermediate, we introduced 24 mutations in SR (Fig. 3.1d), all of which map to the heterodimer interface in the stable complex (Fig. 3.4a) and disrupt formation of the stable complex by 5- to 200-fold [22]. Several of them were also on the interaction surface of the early intermediate identified by EPR (Fig. 3.4a). We tested whether these mutations disrupted the stability of the early intermediate using fluorescence resonance energy transfer (FRET) between coumarin (DACM) labeled SRP C235 and BODIPY-fluorescein (BODIPY-FL) labeled FtsY C487 [20]. To our surprise, most of these mutations did not disrupt the early intermediate (Fig. 3.1d, black bars). Only three mutations caused moderate reductions in the stability of the early intermediate by a factor of 2–4, and a combination of all three mutations destabilized the early intermediate by only a factor of 8 (Fig. 3.1d, gray bars and Fig. 3.4b).

These results presented a conundrum: while EPR studies suggested that the early intermediate has an overlapping interface with the stable complex, mutational analysis showed that this intermediate was insensitive to mutations on this interface. Two models to reconcile these results were tested and verified in the experiments described below. First, the major interactions that stabilize the early intermediate may lie outside the G-domain and its vicinity, where most of the mutations above are located. Second, the early intermediate may not have a defined structure but rather contains multiple conformations, each with a distinct interface.

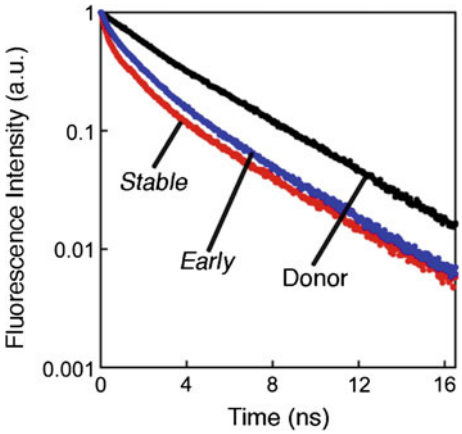

Fig. 3.5 Fluorescence decay of donor (DACM)-labeled at SRP (C76) under different experimental conditions. The *black*, *blue* and *red* curves represent the decay curves for donor-only, the early intermediate and the stable complex, respectively. The linear decay of the donor-only sample could be described by a single decay rate constant. In contrast, the decay curves in both the early intermediate and stable complex deviated from linearity and were described by multiple decay rate constants

Mutations that disrupted a specific interface did not affect alternative conformations, and hence did not significantly affect the overall stability of the intermediate. In contrast, the stable complex is likely to have a more defined structure, and hence is more susceptible to mutations that disrupt the dimer interface.

To test whether the early intermediate samples a broad distribution of conformations, time-resolved FRET (TR-FRET) was used to measure the distance distribution between donor (DACM) and acceptor (BODIPY-FL) dyes labeled at specific sites on SRP and SR in different SRP–SR complexes. These measurements provided nanosecond snapshots of fluorescence decay of the donor dye (Fig. 3.5), from which donor–acceptor distance distributions of the respective complex could be derived [23, 24]. Three pairs of residues were selected to measure distance distributions between the G domains (Fig. 3.6a, G-G), the NG domain interfaces (Fig. 3.6b, NG-NG), and the N domains (Fig. 3.6c, N–N) of both proteins. For all three pairs, the early intermediate exhibited broad distance distributions spanning 25–60 Å with no identifiable dominant population (Fig. 3.6, blue). In contrast, the distributions became significantly more restricted in the stable complex (Fig. 3.6, red), with the dominant distance in good agreement with that measured from the co-crystal structure [19]. These results provided direct evidence that the early intermediate contained a large ensemble of conformations that are similar in stability, whereas the stable complex has a more specific structure. Comparison of these distance distributions also provided clues to the complex assembly process. A significant population of molecules with distances as short as $\sim$25 Å was observed for the N–N pair in the early intermediate, but this population diminished in the stable complex (Fig. 3.6c). In contrast, a significant

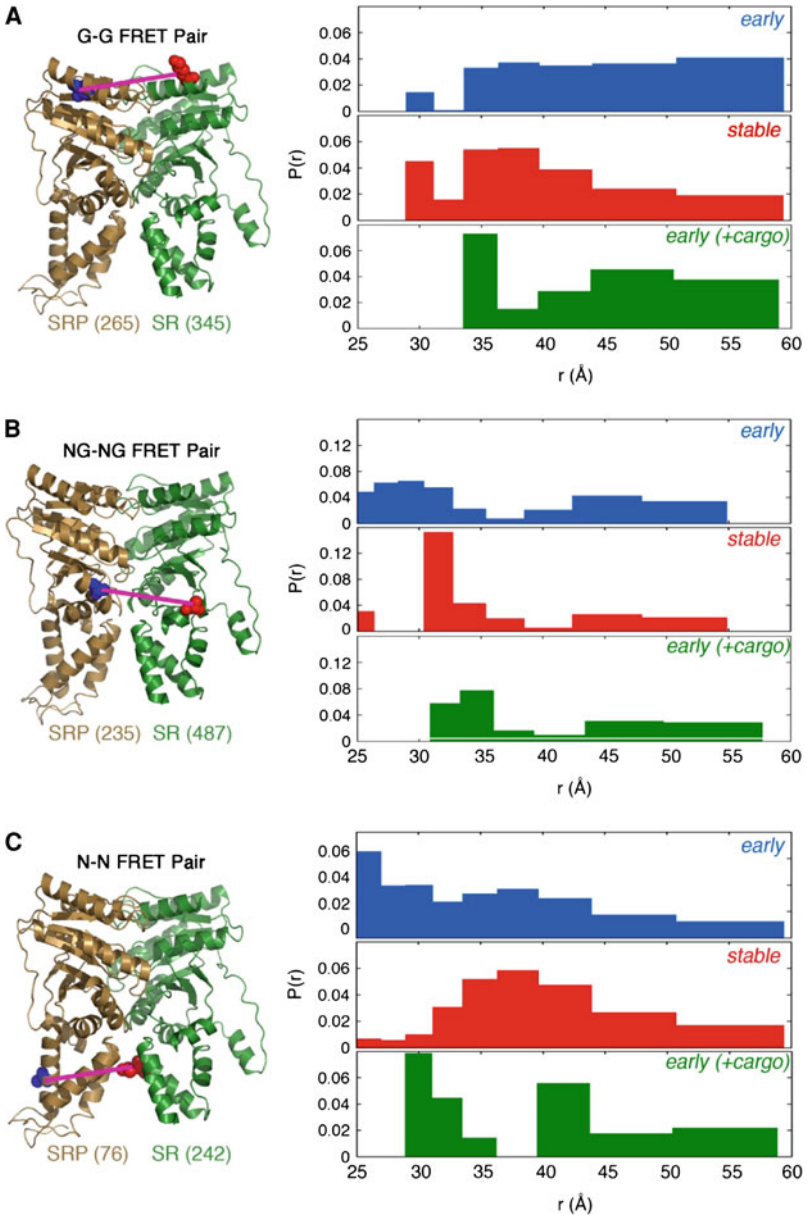

Fig. 3.6 Conformational distribution of the early intermediate is broad, and is restricted upon formation of the stable complex or by the cargo. Left, positions of the G-G (**a**), NG-NG (**b**), and N–N (**c**) FRET pairs in the SRP–SR NG-domain complex. Right, FRET distance distributions, P(r), for each FRET pair in the early intermediate (*blue*), stable complex (*red*), and the early intermediate bound with cargo (*green*), as derived from maximal entropy analyses of the TR-FRET data

population of molecules exhibited long distances (45–60 Å) for the G-G pair in the early intermediate (Fig. 3.6a), which also diminished in the stable complex. This suggests that complex assembly between SRP and SR initiates from close contacts between their N-domains in the early intermediate, whereas the G-domains are further apart.

We hypothesized that these initial close contacts could arise from electrostatic attractions, which have less stringent stereochemical requirements than van der Waals contacts and often facilitate diffusional encounters during macromolecular interactions [25]. Consistent with this hypothesis, adaptive Poisson–Boltzmann solver (APBS) calculation [26] revealed clusters of positively and negatively charged residues, respectively, on the surface of SRP and SR's N-domains (Fig. 3.7a). Interactions between these electrostatically complementary surfaces were supported by their evolutionary conservation (Fig. 3.8), and by molecular docking simulations using the ClusPro 2.0 program [27], which generated molecular models for the early intermediate. Two groups, each containing an ensemble of ~90 structures, scored significantly higher than all the alternative configurations (representative conformations in each group are shown in Fig. 3.7b). In the 'N' group, the N-domains of SRP and SR contact one another via the electrostatically complementary surfaces identified in the APBS calculation (Fig. 3.7a), whereas in the 'G' group, the G-domains of the proteins were adjacent to each other.

Both the 'N' and 'G' groups represent possible conformations within the ensemble of structures of the early intermediate, as residues that changed mobility in EPR measurements resided on the dimer interfaces of both groups (Fig. 3.9), and as both groups were needed to reproduce the experimentally observed broad distance distributions of FRET probes (cf. Fig. 3.10 and Fig. 3.6, blue). Nevertheless, the following strongly suggest that the 'N' group represents the major conformational ensemble. First, the interaction surface mapped by EPR spectroscopy resided largely in the N-domain (Fig. 3.1c, right panel), consistent with the interfaces of the conformers in the 'N' group. Second, most mutations in the G-domain that could affect the 'G' group did not abolish the stability of the early intermediate, suggesting that the conformers in the 'G' group are not significantly populated in this intermediate. Third, in Brownian Dynamics calculations [28], the association rate constant for the early intermediate estimated for the 'N' group was in excellent agreement with the experimental value, whereas that for the 'G' group was 30-fold slower (Fig. 3.7c).

What features in the 'N' group make it the primary conformation of the early intermediate? We reasoned that the presence of complementarily charged surfaces on the N-domains of SRP and SR could facilitate long-range electrostatic interactions that bring the two proteins into proximity (Fig. 3.7a). To test the contribution of these electrostatic interactions, we generated charge reversal mutants in which three basic residues (R35, R49 and K56) on the SRP N-domain were mutated to glutamates (RK3E), and the glutamate residues in the EELEE motif on the SR N-domain were mutated to arginines (EELRR and RRLRR). Mutants SRP (RK3E) and SR (EELRR and RRLRR) severely reduced the stability of the early intermediate (Figs. 3.7d and 3.11f), and caused 10- to 28-fold reductions in the

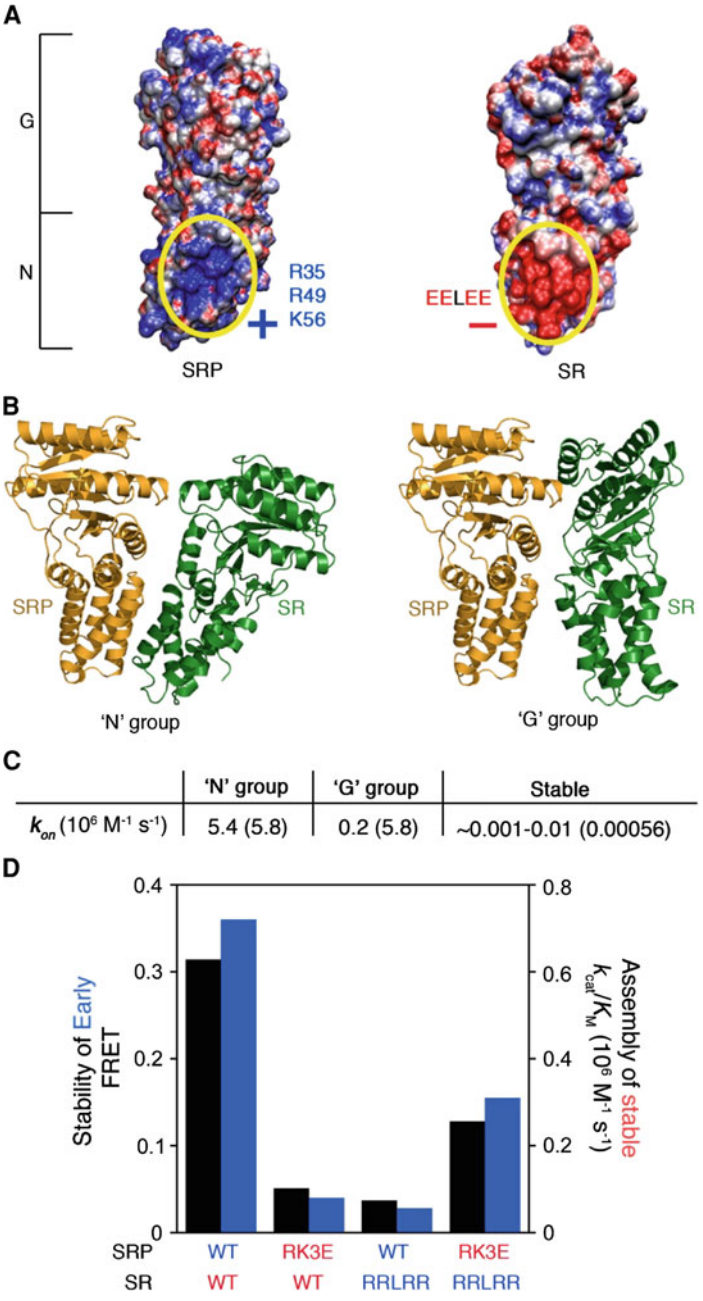

C

	'N' group	'G' group	Stable
k_{on} (10^6 M^{-1} s^{-1})	5.4 (5.8)	0.2 (5.8)	~0.001-0.01 (0.00056)

◀ **Fig. 3.7** Electrostatic interactions between the N-domains of the SRP and SR stabilize the early intermediate and accelerate stable complex assembly. **a** The SRP and SR N-domains contain complementarily charged surfaces. **b** Molecular docking simulation generated two groups of conformations (the 'N' and 'G' groups) for the early intermediate. *Gold* and *green* represent SRP and SR, respectively. **c** The association rate constants predicted from Brownian Dynamics calculations for formation of the early intermediate in the 'N' or 'G' group, and for the stable complex. The experimentally measured rate constants are in parentheses. **d** Charge complementarity between the N domains is critical to the stability of the early intermediate (*black bars*) and the kinetics of stable complex assembly (*blue bars*). The stabilities of the early intermediate and the kinetics for stable complex assembly were determined for the wildtype proteins (WT:WT), wildtype SRP and mutant SR (WT:RRLRR), mutant SRP and wildtype SR (RK3E:WT), and the charge reversal SRP and SR mutants (RK3E:RRLRR). The kinetic constants were derived from the data in Fig. 3.11g

association rate constant for stable SRP–SR complex assembly (Figs. 3.7d and 3.11c, d). In addition, the SR (EELRR) mutation increased the dissociation rate constant of the stable complex sevenfold, and reduced its equilibrium stability ~200-fold (Fig. 3.11e). Thus these electrostatic interactions play key roles in the stability and kinetics of the SRP–SR interaction.

We further asked whether the SRP–SR interaction can be rescued by combining the charge reversal mutants of SRP and SR, which partially restores the electrostatic interaction between their N-domains (Fig. 3.11a). Indeed, the combination of the SRP (RK3E) and SR (RRLRR) mutants restored the stability of the early intermediate to within threefold of that of the wildtype complex (Figs. 3.7d, black bars and Fig. 3.11b). The kinetics of stable complex assembly was similarly rescued (Fig. 3.7d, blue bars). The incomplete rescue could be accounted for by the fact that, although the SRP (RK3E) mutation made the N-domain of SRP highly negatively charged, the SR (RRLRR) mutation rendered the N-domain of SR only moderately positively charged (Fig. 3.11a). Together, these results strongly supported the notion that long-range electrostatic interactions provide an important driving force to form and stabilize the early intermediate, and to enhance the kinetics of stable complex assembly.

The SRP–SR interaction is profoundly influenced by the cargos of SRP, the ribosome nascent chain complexes (RNCs), which stabilize the early intermediate over 50-fold and accelerate stable complex assembly over 100-fold [17, 18]. We speculated that the cargo could actively regulate the conformational dynamics of the early intermediate. To test this hypothesis, we used TR-FRET to measure the conformational distribution of the early intermediate in the presence of RNC_{FtsQ}, which contains the first 74 amino acids of FtsQ, a known SRP substrate. Notably, the cargo substantially narrowed the distance distribution of all the FRET pairs in the early intermediate, changing their broad distance distributions to more bimodal patterns (Fig. 3.6, green). Thus the cargo restricts the dynamics of the early intermediate to a more limited conformational space, in which the successful selection of complementary structures might be enhanced. This could partly explain how the cargo enhances the kinetics of SRP-SR complex assembly and therefore effect efficient protein targeting.

Fig. 3.8 Sequence alignment of Ffh (**a**) and FtsY (**b**) homologues. The residue numbering is for *E. coli* Ffh and FtsY. Conserved positive and negative residues are denoted in *blue* and *red* colors, respectively

In summary, using the SRP–SR interaction as a model system, we have analyzed the structure, dynamics, and energetics of an on-pathway intermediate during protein complex assembly; the results revealed important features of this intermediate and shed light on the protein association process. First, the interaction surface used by the intermediate overlaps with but is distinct from that of the stable complex, with interactions between complementarily charged surfaces on their N-domains providing the primary stabilizing force. In contrast, more stereospecific interactions between the G-domains, which provide most of the stabilization for the stable complex, are rather weak at the intermediate stage. Thus, this protein interaction likely initiates at sites that are adjacent to but distinct from the final interaction surface, and is largely driven by long-range, relatively nonspecific electrostatic interactions. Second, the conformational distribution of the early intermediate is very broad but becomes much more restricted in the stable complex, suggesting that the intermediate samples a wide conformational space to seek the optimal structure conducive to formation of the stable complex (Fig. 3.12,

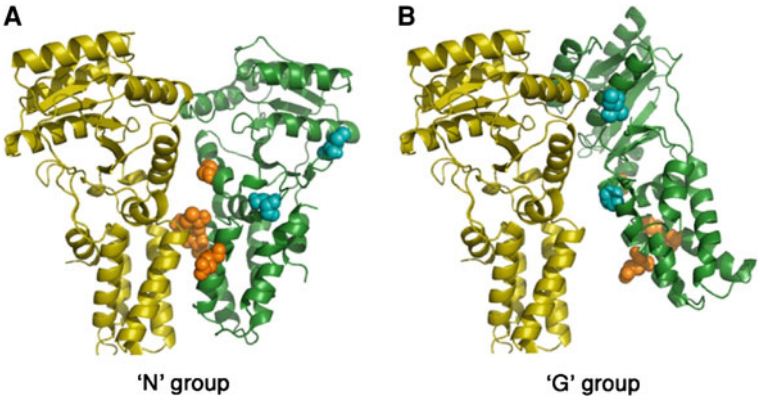

Fig. 3.9 Spin probes that changed mobility upon formation of the early intermediate are on residues close to the interaction surface of either the 'N' (*orange residues*) or the 'G' (*cyan residues*) group. The SRP NG-domain is in *gold*, and the SR NG-domain is in *green*

blue). Third, the stable complex still exhibits a distribution of FRET distances rather than a singular value, suggesting that residual, albeit more restricted, conformational sampling occurs after the stable complex is formed (Fig. 3.12, red). Finally, the conformational ensemble of the intermediate is actively regulated by the cargo, which could provide a mechanism to exert biological regulation (Fig. 3.12, green) [18]. These features of the early intermediate during protein assembly bear intriguing analogies to molten globules during protein folding [29], in that both are relatively resistant to many mutations and have a broad free energy landscape that allows the protein(s) to sample multiple configurations [29]. Also analogous to the protein folding process, the energy landscape of protein assembly is likely funnel-shaped and becomes narrower as the free proteins transition through the intermediate and progress towards the stereospecific complex (Fig. 3.12) [8]. These findings could represent general features of transient intermediates during protein assembly, and provide a framework to understand their roles in enhancing protein interactions and biological regulation.

3.3 Materials and Methods

3.3.1 Materials

The *E. coli* SRP and SR GTPases (Ffh and FtsY, respectively) and the 4.5S RNA were expressed and purified as described previously [20, 30]. Truncated FtsY (47–497) was used in all the fluorescence and EPR measurements (except for the charge reversal mutants FtsY (EELRR and RRLRR). The abilities of FtsY (47–497) to interact with SRP and respond to the cargo are similar to those of full

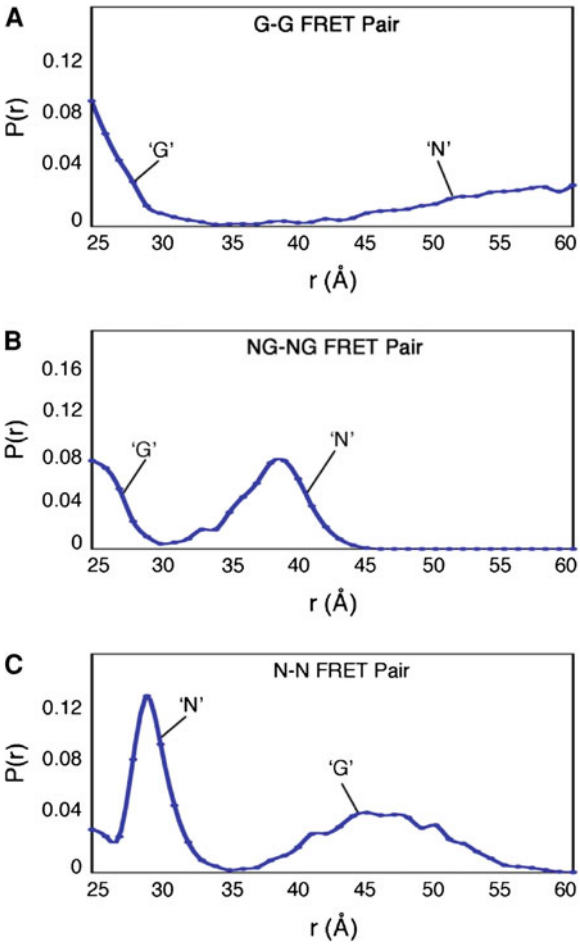

Fig. 3.10 Distance distributions between the three pairs of FRET probes predicted by a combination of the structures in the 'N' and 'G' groups

length FtsY [30]. Mutant Ffh and FtsY's were constructed using the QuickChange mutagenesis procedure (Stratagene). All the mutant proteins were expressed and purified using the same procedure as that for the wild-type proteins. Fluorescent dyes N-(7-dimethylamino-4-methylcoumarin-3-yl)maleimide (DACM) and BODIPY-FL-N-(2-aminoethyl)-maleimide were from Invitrogen.

3.3.2 RNC_{FtsQ} Purification

Homogeneous RNC_{FtsQ} were generated from in vitro translation using membrane free cell extract prepared from MRE600 cells, and were purified by affinity

chromatography and sucrose gradient centrifugation as described previously [17, 31]. Purified RNC_{FtsQ} serves as a functional cargo in protein targeting as it can bind SRP, trigger factor, and the secYEG translocon complex [31]. In quantitative assays, purified RNC_{FtsQ} exhibited the same affinity for SRP as those measured with RNCs that do not contain an affinity tag [32].

3.3.3 Fluorescence Labeling

For FRET measurements, DACM and BODIPY-FL were used to label single-cysteine mutants of Ffh and FtsY, respectively, as described previously [20]. Labeled protein was purified as described [20], and the efficiency of labeling was typically $\geq$95% with a background of <5%.

3.3.4 Spin Labeling

Single cysteine mutants of FtsY [in 20 mM HEPES (pH 8.0), 150 mM NaCl and 2 mM EDTA] were incubated with a tenfold molar excess of dithiothreitol (DTT) at room temperature for 1–2 h to reduce any disulfide bonds. DTT was removed by gel filtration chromatography. The reduced and degassed proteins ($\sim$100 μM) were labeled with a three- to fivefold molar excess of MTSSL (Toronto Research Chemicals, Toronto, Canada) at room temperature in the dark for 2–3 h. Excess MTSSL was removed by gel filtration chromatography. The labeling efficiency was determined by EPR using the TEMPO calibration curve (Bruker user manual), and was typically >80% with <5% background as assessed from the cysteine-less wild-type protein using the same procedure. All the spin-labeled proteins were tested for interaction with SRP using the GTPase assay; only the spin-labeled FtsY mutants that did not substantially disrupt activity were used for EPR measurements.

3.3.5 Electron Paramagnetic Resonance (EPR) Measurements

EPR measurements were carried out to determine the local mobility of twenty-three spin-labeled FtsY mutants in apo-FtsY, in the early intermediate, and in the stable complex. For apo-FtsY, 75–100 μM spin-labeled protein was used to obtain the EPR spectra. The early intermediate was formed by mixing 30 μM spin-labeled FtsY with 90 μM SRP in the presence of GDP. Based on the affinity of the early intermediate ($K_d \sim$ 4–10 μM) [20], >90% of labeled FtsY formed the early complex with SRP under these conditions. The stable complex was formed by mixing 30 μM spin-labeled-FtsY with 60 μM SRP in the presence of GMPPNP. Over 99% of labeled FtsY formed a stable complex with SRP under these conditions, according to the K_d values of the stable complex of $\sim$16–30 nM [20].

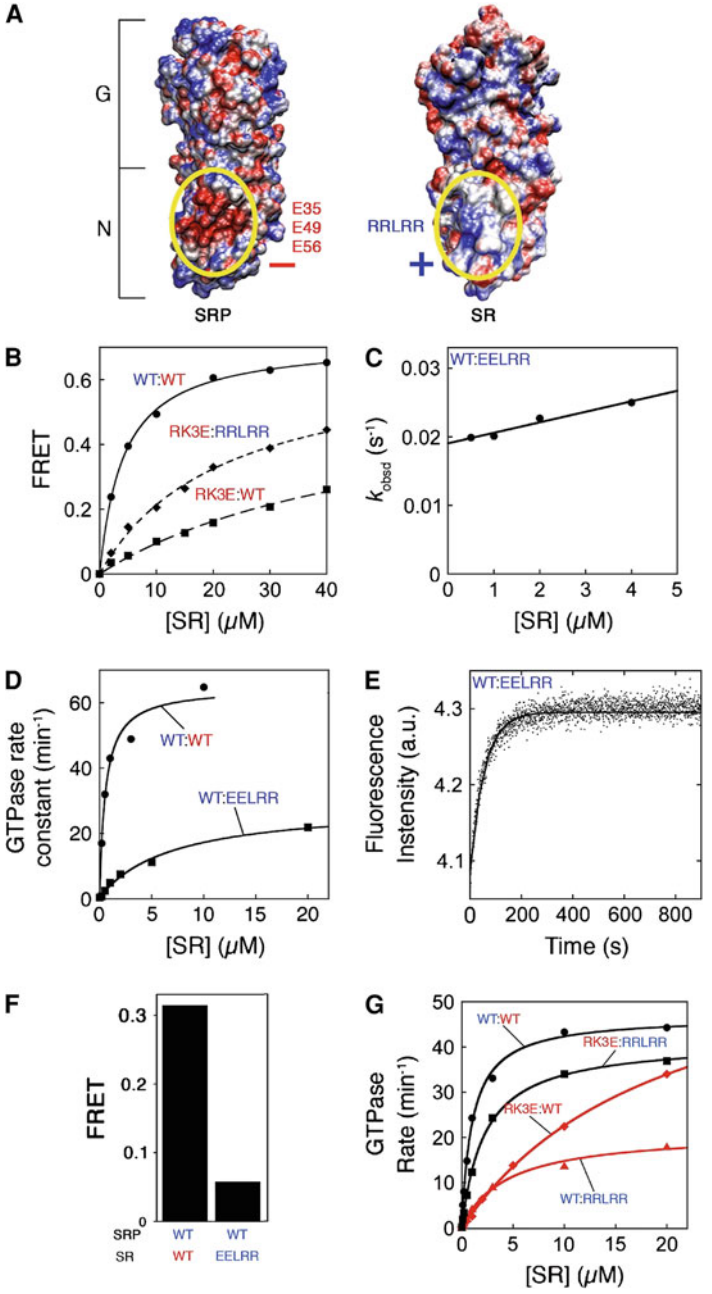
A
G
N
E35
E49
E56
SRP
RRLRR
SR
B
FRET
WT:WT
RK3E:RRLRR
RK3E:WT
[SR] (μM)
C
WT:EELRR
k_{obsd} (s^{-1})
[SR] (μM)
D
GTPase rate constant (min^{-1})
WT:WT
WT:EELRR
[SR] (μM)
E
WT:EELRR
Fluorescence Instensity (a.u.)
Time (s)
F
FRET
SRP WT WT
SR WT EELRR
G
GTPase Rate (min^{-1})
WT:WT
RK3E:RRLRR
RK3E:WT
WT:RRLRR
[SR] (μM)

◀ **Fig. 3.11** Mutations that disrupted charge complementarity between SRP and SR's N-domains reduced the stability of the early intermediate and the kinetics of stable complex assembly. **a** The R36E:R49E:K56E (R2E) mutation in SRP generated a negative electrostatic potential in the SRP N-domain (left), and the RRLRR mutation in SR generated a moderately positive electrostatic potential in the SR N-domain (right). **b** The stabilities of the early intermediates formed by mutant SRP and SR's were determined by equilibrium titrations. Nonlinear fits of data to Eq. 3.2 gave K_d values of 4.0 μM for WT:WT (wild-type SRP and SR), 50.1 μM for R2E:WT [mutant SRP (R2E) and wild-type SR], and 20.1 μM for R2E:RRLRR [mutants SRP (R2E) and SR (RRLRR)]. **c**, **d** Association rate constant for stable complex formation between wild-type SRP and mutant SR (EELRR) determined by the FRET (**c**) and the GTPase (**d**) assays. Linear fits of the data in **c** gave an association rate constant of 1.53×10^3 M^{-1} s^{-1}, 28-fold slower than that of the wild-type SR of 4.4×10^4 M^{-1} s^{-1} [17]. Fits of data in **d** to Eq. 3.1 gave k_{cat}/K_m values of 1.91×10^6 M^{-1} s^{-1} for wild-type SR and 6.82×10^4 M^{-1} s^{-1} for mutant SR (EELRR). The values of k_{cat}/K_m in the GTPase assay are equal to that of stable complex assembly (see Materials and Methods). **e** Dissociation rate constant of the stable complex between wild-type SRP and mutant SR (EELRR) was determined to be 0.0183 s^{-1} using the FRET assay, sevenfold faster than that of the wild-type SR of ~0.0026 s^{-1} [17]. Together, the dissociation and association rate constants gave a K_d value of 11.9 μM for stable complex assembly with mutant SR (EELRR), ~200-fold weaker than that of the wild-type complex. **f**, **g** Charge complementarity between the N domains is critical to the stability of the early intermediate (**f**) and the kinetics of stable complex assembly (**g**). Nonlinear fits of the data in **e** gave k_{cat}/K_m values of 0.72×10^6, 0.056×10^6, 0.080×10^6, and 0.31×10^6 M^{-1} s^{-1}, respectively, for the interaction between the wildtype proteins (WT:WT), wildtype SRP and mutant SR (WT:RRLRR), mutant SRP and wildtype SR (RK3E:WT), and the charge reversal SRP and SR mutants (RK3E:RRLRR)

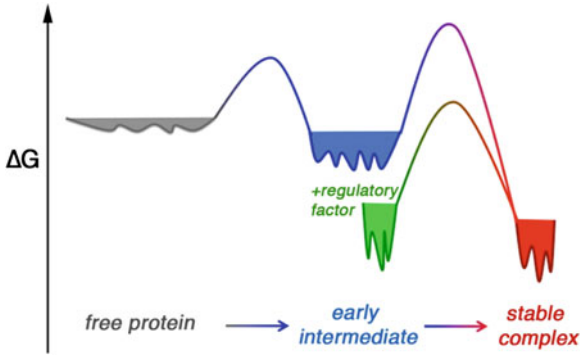

Fig. 3.12 Free energy landscapes for the protein–protein assembly process. The conformational space is broad for the free proteins (*grey*) and the early intermediate (*blue*), but becomes more restricted in the stereospecific stable complex (*red*) or in the presence of the cargo (*green*)

EPR spectra were acquired with a 9.4 GHz (X-band) Bruker EMX EPR spectrometer equipped with an ER 4119HS cavity at 20–23 °C. 40% glycerol was present in all samples to eliminate the global tumbling motion of proteins. Since the central linewidth (ΔH_0) of EPR spectra stayed the same at microwave powers of 0.2 mW, 2 mW, or 5 mW, all scans were carried out using a microwave power of 5 mW to improve the signal-to-noise ratio. The modulation amplitude was set at 2 gauss and magnetic field sweep width was set as 100 gauss. For each sample, an

averaged spectrum was obtained from approximately 32–64 scans and the background signal was subtracted.

3.3.6 GTPase Assay

The assay to measure the stimulated GTP hydrolysis reaction between SRP and SR were performed and analyzed as described [30]. Briefly, reactions were carried out in SRP buffer [50 mM KHEPES, pH 7.5, 150 mM KOAc, 2 mM $Mg(OAc)_2$, 2 mM DTT, 0.01% Nikkol] in the presence of a small, fixed amount of SRP (100–200 nM), varying amounts of SR, and saturating GTP (100–200 μM). The observed rate constants (k_{obsd}) were plotted against SR concentration and fit to Eq. 3.1,

$$k_{obsd} = k_{cat} \times \frac{[\mathrm{SR}]}{K_m + [\mathrm{SR}]} \tag{3.1}$$

in which k_{cat} is the maximal rate constant at saturating SR concentrations, and K_m is the concentration required to reach half saturation. Because k_{cat} is at least 100-fold faster than the rate of SRP–SR complex disassembly, the rate constant k_{cat}/K_m in this assay is rate-limited by and therefore equal to the rate of stable SRP–SR complex formation [30]. No DTT was present in the reactions involving spin-labeled proteins.

3.3.7 Steady-state Fluorescence Measurements

All measurements were carried out at 25 °C in SRP buffer on a Fluorolog-3-22 spectrofluorometer (Jobin–Yvon, Edison, NJ). FRET measurements were carried out using an excitation wavelength of 380 nm and an emission wavelength of 470 nm. FRET efficiency was calculated as described.

To compare the relative equilibrium stabilities of the early intermediates formed with different SR mutants, 4 μM BODIPY-FL labeled SR mutants were incubated with 1 μM DACM-labeled SRP in the absence of GTP. As formation of the early intermediate is rapid but has a high K_d (4–10 μM), the changes in FRET value at the subsaturating SR concentration provided a sensitive measure of the changes in the stability of the early intermediate caused by the mutations in SR. For representative mutants, equilibrium titrations were further carried out in the presence of a small, fixed amount of donor-labeled SRP and increasing amounts of acceptor-labeled SR in the absence of GTP or GTP analogues. FRET efficiency was plotted as a function of SR concentration ([SR]) and fit to Eq. 3.2,

$$E = E_1 \times \frac{[\mathrm{SR}]}{K_d + [\mathrm{SR}]} \tag{3.2}$$

in which E_1 is the FRET value (end point) when all the SRP are bound to SR, and K_d is the equilibrium dissociation constant of the early intermediate.

3.3.8 TR-FRET Measurements

TR-FRET experiments were carried out to measure the distance distribution between the donor (DACM) on SRP and acceptor (BODIPY-FL) on SR. SRP (C265)-SR (C345), SRP (C235)-SR (C487), and SRP (C76)-SR (C242) were used as G-G, NG-NG, and N–N FRET pairs, respectively (Fig. 3.6). Donor-only measurements were carried out in the presence of 5 or 1 μM DACM-labeled SRP for the early and stable complexes, respectively. For the early intermediate, 5 μM DACM-labeled SRP and 50 μM BODIPY-FL-labeled SR were mixed together in the presence of GDP. For the stable complex, 1 μM DACM-labeled SRP and 8 μM BODIPY-FL-labeled SR were mixed in the presence of GMPPNP. Formation of both complexes was complete after a 20-min incubation at room temperature in dark.

Time-resolved DACM fluorescence decay measurements were carried out with a picosecond streak camera (C5680; Hamamatsu Photonics) in the photon-counting mode [33, 34]. The excitation wavelength was set at 355 nm from a third harmonic of a regeneratively amplified mode-locked Nd-YAG laser (pulsewidth is $\sim$15 ps) (Vanguard, Spectra-Physics). A band-pass filter of 450 $\pm$ 5 nm was used as the emission filter, which minimizes the fluorescence from the acceptor (BODIPY-FL). There was no observable fluorescence from buffer or unlabeled protein. DACM fluorescence decay kinetics was measured in both short (5 ns) and long (20 ns) time scale, with time resolutions of $\sim$10 and $\sim$40 ps, respectively.

3.3.9 Data Fitting and Analysis for TR-FRET Measurements

The measured short and long time-scale data were spliced together, and the combined traces were compressed logarithmically before the fitting process (70 points per decade). The splicing and compression did not introduce artifacts to the interpretation of data [23]. Analyses of the TR-FRET data can be described as a numerical inversion of a Laplace transform $\left[I(t) = \sum_k P(k)\exp^{-kt}\right]$, in which $I(t)$ is fluorescence intensity, k is the fluorescence decay rate constant, and $P(k)$ is the probability of a specific k[35, 36]. In this work, two algorithms were used to invert the kinetics data with regularization methods that also impose a non-negativity constraint, $P(k) \geq 0\,(\forall k)$. The first method is based on the Least-Squares (LSQ) fitting algorithm. The LSQ fitting used a MATLAB algorithm (LSQNONNEG) (Mathworks, Natck, MA) that minimizes the sum of the squared deviations (χ^2) between observed and calculated values of $I(t)$, subject to the non-negativity constraint. This algorithm produces the narrowest $P(k)$ distributions and smallest values of χ^2 with relatively few nonzero

components. The second method is based on the Maximum Entropy (ME) theory. The information theory proposes that the least biased solution to the inversion problem is to minimize χ^2 and maximize the breadth of $P(k)$ [37]. This regularization condition can be met by maximizing the Shannon–Jaynes entropy of the rate-constant distribution $\left\{S = -\sum_k P(k)\ln[P(k)]\right\}$ while satisfying the non-negativity constraint. ME fitting generated stable and reproducible numerical inversions of the kinetics data. The balance between χ^2 minimization and entropy maximization is evaluated by the L-curve analysis, which yielded upper limits for the widths of $P(k)$ consistent with experimental data. The $P(k)$ distributions from ME fitting were broader than those obtained with LSQ fitting, but exhibited maxima at similar locations.

Both methods were used to generate the decay rate distribution $P(k)$. A coordinate transformation using the Förster relation (Eq. 3.3) was then used to convert the probability distribution of the decay rates k to the donor–acceptor distances r, thus generating the donor–acceptor distance distribution $P(r)$.

$$r = R_0\left(\frac{k}{k_0} - 1\right)^{1/6} \tag{3.3}$$

The Förster radius, R_0, for the DACM/BODIPY-FL pair is $\sim$47 Å. The value of k_0 was obtained from donor-only measurements, which gave a nearly single-exponential (>90%) fluorescence decay kinetics for all three positions in this study. At distances larger than 1.5 R_0, energy transfer does not take place efficiently, whereas at distances $< \sim$ 13 Å, the Förster model does not reliably describe FRET kinetics. Therefore, our TR-FRET measurements can provide information about donor–acceptor distances only in the range of 13–70 Å.

3.3.10 Docking

The ClusPro 2.0 docking server was used to generate docking models for the early intermediate. This program was chosen because it emphasizes the number of energy-preferred structures in the docking cluster, and is therefore particularly suitable to generate an ensemble of conformations for the early intermediate. During the docking, *E. coli* Ffh was set as a static receptor while *E. coli* FtsY was set as a ligand that searched for the best docking position with the receptor. The initial docking positions were generated by the Fast Fourier Transform method and docking positions were clustered according to their root mean squares deviations. Clusters were sorted via a filter which was set to an energy function that favors electrostatic interactions. The ranking of the clusters was determined by the number of structures that each cluster contained. The top five clusters had 89, 88, 65, 59 and 46 structures, respectively. The top two clusters, named ‘G’ and ‘N’, were chosen for further analyses.

3.3.11 Brownian Dynamics

BrownDye was used for Brownian Dynamics calculations [28]. APBS was used to calculate the electrostatic potentials [26]. Partial atomic charges and atomic radii were assigned from the PARSE parameter set. The dielectric constants were assigned to be 4 in the protein interior and 78 in the exterior. Grids were assigned with dimensions of 193 × 193 × 193 points. Temperature was set to 298 K and ionic strength was set to 100 mM. Brownian dynamics trajectories were started at a minimum intermolecular separation that still gave spherically symmetric forces. The number of trajectories to estimate the association rate constants varied from 40,000 to 100,000 depending on how fast the rates were. The reaction criterion was specified by the atom-contact pairs defined by the structure of the complex. All the intermolecular nitrogen–oxygen pairs within 0.55 nm were considered as within the reaction criterion. A series of simulations with different levels of reaction criteria were generated by systematically tuning the required atom-contact number from 3 to 7. Three structures were used for this analysis to obtain the association rate constants: the central structure of the 'G' cluster, the central structure of the 'N' cluster, and the crystal structure of the stable complex.

Acknowledgment Electron paramagnetic (EPR) measurements were carried out by Dr. Vinh Q. Lam; molecular docking and Brownian Dynamics simulations were carried out by Yun Mou and Dr. Steven L. Mayo; time-resolved FRET (TR-FRET) measurements were assisted by Dr. Tetsunari Kimura and Dr. Jay R. Winkler; sequence alignment was performed by Sowmya Chandrasekar. We thank H. B. Gray and P. E. Wright for insightful discussions, and D. C. Rees, T. F. Miller III, and members of the Shan laboratory for comments on the manuscript. This work was supported by NIH grants GM078024 to S.S. and GM068041 to J.R.W., DARPA Protein Design Processes to S.L.M., and career awards from the Burroughs Welcome Foundation, the Henry and Camille Dreyfus foundation, the Arnold and Mabel Beckman foundation, and the David and Lucile Packard foundation to S.S.

References

1. Alberts B (1998) Cell 92:291
2. Blundell TL, Fernandez-Recio J (2006) Nature 444:279
3. Boehr DD, Wright PE (2008) Science 320:1429
4. Schreiber G, Haran G, Zhou HX (2009) Chem Rev 109:839
5. Ubbink M (2009) FEBS Lett 583:1060
6. Janin J (1997) Proteins 28:153
7. Koshland DE (1958) Proc Natl Acad Sci U S A 44:98
8. Ma B, Kumar S, Tsai CJ, Nussinov R (1999) Protein Eng 12:713
9. Iwahara J, Clore GM (2006) Nature 440:1227
10. Tang C, Iwahara J, Clore GM (2006) Nature 444:383
11. Volkov AN, Worrall JA, Holtzmann E, Ubbink M (2006) Proc Natl Acad Sci U S A 103:18945
12. Tang C, Schwieters CD, Clore GM (2007) Nature 449:1078
13. Lange OF et al (2008) Science 320:1471
14. Tang C, Louis JM, Aniana A, Suh JY, Clore GM (2008) Nature 455:693

15. Fawzi NL, Doucleff M, Suh JY, Clore GM (2010) Proc Natl Acad Sci U S A 107:1379
16. Crowley PB, Ubbink M (2003) Acc Chem Res 36:723
17. Zhang X, Schaffitzel C, Ban N, Shan SO (2009) Proc Natl Acad Sci U S A 106:1754
18. Zhang X, Rashid R, Wang K, Shan SO (2010) Science 328:757
19. Egea PF et al (2004) Nature 427:215
20. Zhang X, Kung S, Shan SO (2008) J Mol Biol 381:581
21. Crane JM, Lilly AA, Randall LL (2010) Methods Mol Biol 619:173
22. Shan SO, Stroud RM, Walter P (2004) PLoS Biol 2:1572
23. Kimura T, Lee JC, Gray HB, Winkler JR (2009) Proc Natl Acad Sci U S A 106:7834
24. Kimura T, Lee JC, Gray HB, Winkler JR (2007) Proc Natl Acad Sci U S A 104:117
25. Schreiber G, Fersht AR (1996) Nat Struct Biol 3:427
26. Baker NA, Sept D, Joseph S, Holst MJ, McCammon JA (2001) Proc Natl Acad Sci U S A 98:10037
27. Comeau SR et al (2007) Proteins 69:781
28. Ermak DL, Mccammon JA (1978) J Chem Phys 69:1352
29. Pande VS, Rokhsar DS (1998) Proc Natl Acad Sci U S A 95:1490
30. Peluso P, Shan SO, Nock S, Herschlag D, Walter P (2001) Biochem 40:15224
31. Schaffitzel C, Ban N (2007) J Struct Biol 158:463
32. Bornemann T, Jockel J, Rodnina MV, Wintermeyer W (2008) Nat Struct Mol Biol 15:494
33. Lee JC, Engman KC, Tezcan FA, Gray HB, Winkler JR (2002) Proc Natl Acad Sci U S A 99:14778
34. Lee JC, Langen R, Hummel PA, Gray HB, Winkler JR (2004) Proc Natl Acad Sci U S A 101:16466
35. Beals JM, Haas E, Krausz S, Scheraga HA (1991) Biochem 30:7680
36. Beechem JM, Haas E (1989) Biophys J 55:1225
37. Istratov AA, Vyvenko OF (1999) Rev Sci Instrum 70:1233

Chapter 4
Multiple Conformational Switches Control Co-translational Protein Targeting

4.1 Introduction

SRP-mediated co-translational protein targeting delivers roughly a third of proteins to their correct subcellular destinations, including the eukaryotic endoplasmic reticulum and the bacterial plasma membrane. This pathway involves a sequential series of molecular steps [1–3], including (1) recognition and loading of cargo (ribosomes translating nascent polypeptides with signal sequences) on the SRP; (2) delivery of cargo to the target membrane via complex formation between SRP and SR; (3) unloading and transfer of cargo from the SRP to the protein conducting channel (PCC); and (4) disassembly of the SRP–SR complex and recycling of free SRP and SR for subsequent rounds of protein targeting. Like many cellular processes, this complex series of molecular interactions are spatially and temporally regulated by members of the GTPase superfamily, in this case, two highly homologous and directly interacting GTPases in both the SRP and SR.

SRP and SR provide a notable exception to the 'GTPase switch' paradigm established for classical signaling GTPases [4]. These GTPases do not exhibit substantial conformational changes depending on whether GTP or GDP is bound [5–7], and further, their intrinsic nucleotide exchange rates are 10^2–10^4-fold faster than those of classical GTPases [8, 9]. Thus no external GEFs are required to switch these GTPases from the GDP- to the GTP-bound state, and the facilitation of nucleotide exchange by an external GEF cannot be the mechanism to turn these GTPases to the 'on' state. Moreover, SRP and SR reciprocally stimulate each other's GTP hydrolysis activity when they form a complex with one another [8, 10]. Thus no external GAPs are required either to switch these GTPases from the GTP- to the GDP-bound state, and the stimulation of GTP hydrolysis by an external GAP cannot be the mechanism to turn these GTPases to the 'off' state.

A version of this chapter has been published as Zhang et al (2009) Proc Natl Acad Sci U S A 106:1754–1759.

X. Zhang, *Multistate GTPase Control Co-translational Protein Targeting*,
Springer Theses, DOI: 10.1007/978-1-4419-7808-0_4,

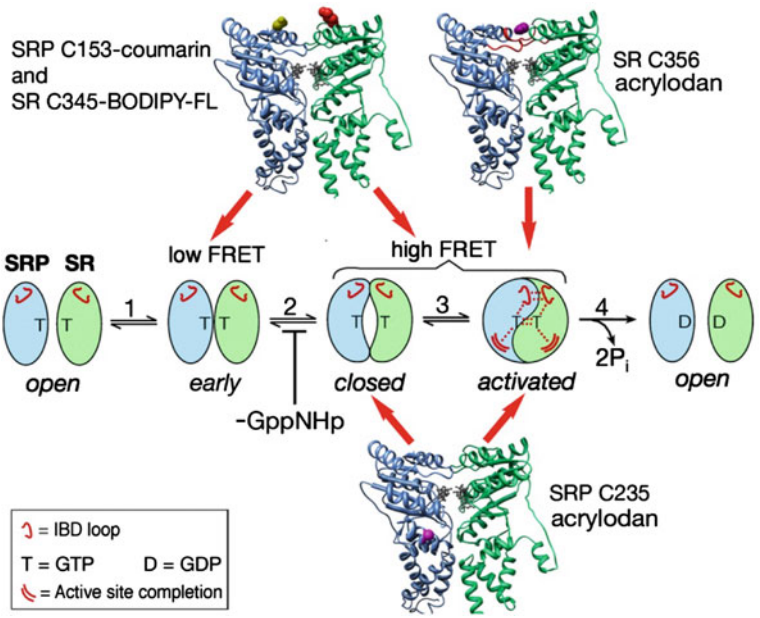

Fig. 4.1 Multiple conformational changes during SRP–SR complex formation and activation [11, 16], as described in the text, and the positions of fluorescence probes that detect the different conformational stages, as described in the text. Adapted from [16], with permission from Elsevier

In contrast, these GTPases undergo a series of discrete conformational changes driven by heterodimeric interactions between the two GTPases (Fig. 4.1) [10–13]. Both proteins, starting in an inactive, '*open*' conformation, quickly bind one another to form a transient '*early*' intermediate independently of GTP (Fig. 4.1, step 1). The presence of GTP bound at both GTPase active sites induces a conformational rearrangement in both proteins to form a stable '*closed*' complex (Fig. 4.1, step 2) [11, 13, 14]. A subsequent rearrangement involving the activation loops in both proteins activates GTP hydrolysis (Fig. 4.1, step 3) [11, 12], which drives disassembly of the complex (Fig. 4.1, step 4) [15].

If these conformational rearrangements during SRP–SR binding and activation are integral to the regulatory role of these GTPases in protein targeting, then they should be responsive to the biological events they are monitoring. To test this hypothesis, we examined the effects of cargo loading on the kinetic and thermodynamic features of the SRP and SR's GTPase cycle. Our results demonstrate that the SRP and SR GTPases can use each of the conformational changes during their binding and activation cycle to sense temporal cues such as cargo loading and in response, substantially change the free energy landscape of the different conformational states in the SRP–SR GTPase complex. These cargo-induced responses allow these GTPases to drive the efficient delivery and unloading of cargo to the target membrane, and to potentially improve the fidelity of protein targeting via kinetic proofreading mechanisms.

4.2 Results

4.2.1 General Experimental Approach

To monitor the different conformational stages of the SRP–SR complex, we used fluorescence resonance energy transfer (FRET) between donor and acceptor probes incorporated on the SRP and SR. FRET provides a highly sensitive assay that allows us to detect the transient *early* intermediate (Fig. 4.1) [16]. Further, this intermediate can be distinguished from the subsequent conformations because it has a lower FRET value than the *closed* and *activated* complexes (Fig. 4.1) [16]. In addition, an environmentally sensitive probe, acrylodan labeled at residue 235 of SRP, detects formation of the *closed* and *activated* complexes but not the *early* intermediate (Figs. 4.1 and 4.2), thereby simplifying kinetic and thermodynamic analyses of these later conformations. Finally, acrylodan labeled at residue 356 of SR near its catalytic loop specifically detects the *activated* complex (Figs. 4.1 and 4.3). In addition to these fluorescent probes, mutant GTPases and GTP analogues were used to block specific rearrangements and thus isolate each conformational intermediate [10, 11]. We can block the *early* → *closed* rearrangement by leaving out GTP (Fig. 4.1) [16]; this allows us to isolate the *early* intermediate and characterize its kinetics and stability. Mutations in the catalytic loop, SRP A144W or SR A335W, allow a stable *closed* complex to form but block its rearrangement to the *activated* complex [11, 17]. The non-hydrolyzable GTP

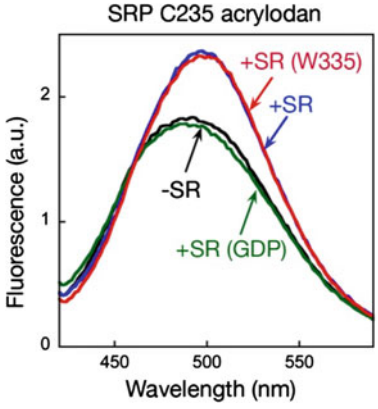

Fig. 4.2 Acrylodan labeled SRP C235 monitors formation of the *closed/activated* conformation. Fluorescence emission spectra are acquired in the presence of GppNHp for acrylodan-labeled SRP C235 alone (0.1 microM; *black*), labeled SRP C235 incubated with 1 microM wild type SR (*blue*), or labeled SRP C235 incubated with 1 microM SR A335W (*red*), which is blocked in the *closed/activated* rearrangement and thus isolates the *closed* complex [11], or in the presence of GDP with 10 microM SR (*green*), which isolates the *early* complex [16]

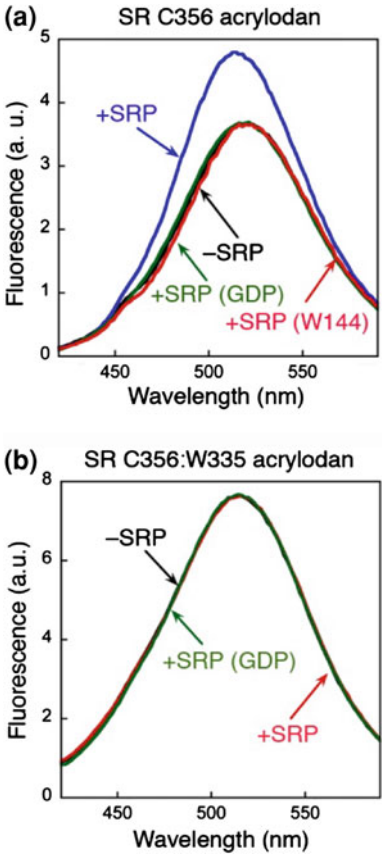

Fig. 4.3 Acrylodan labeled SR C356 specifically monitors formation of the *activated* SRP–SR complex. **a** Fluorescence emission spectra was obtained for acrylodan labeled SR C356 alone (0.1 microM; *black*), acrylodan labeled SR C356 incubated with wild type SRP (*blue*) or SRP A144W (*red*) in the presence of GppNHp, or with 10 microM SRP in the presence of GDP (*green*). SRP A144W allows a stable *closed* complex to form but specifically blocks formation of the *activated* complex [17]. The absence of fluorescence change with SRP A144W shows that acrylodan labeled SR C356 specifically monitors formation of the *activated* complex. **b** Acrylodan labeled C356 does not change fluorescence if mutant SR A355W [11] was used to block the formation of the *activated* complex. Spectra was obtained for 0.1 microM acrylodan labeled SR A335W:C356 alone (*black*) and when this labeled SR mutant was incubated with 1 microM SRP in the presence of GppNHp (*red*) or with 5 microM SRP in the presence of GDP (*green*). The absence of a fluorescence change shows that the probe on SR T356 does not detect the *early* or the *closed* complex. Adapted from [16], with permission from Elsevier

analogue 5′-guanylylimido-diphosphate (GppNHp) allows most of the rearrangements to occur but inhibits GTP hydrolysis [10, 11]. Using these tools, we determined how the SRP and SR GTPases use their conformational changes to respond to cargo loading.

4.2.2 Cargo Accelerates Assembly of a Stable SRP–SR Complex Over 100-Fold

As cargo, we purified stalled ribosome–nascent chain complexes (RNCs) bearing the N-terminal 74 amino acids of the model SRP substrate FtsQ [18–20]. SRP–SR complex assembly was monitored using FRET in the presence of GppNHp. Comparison of the time courses for complex assembly shows three differences between free and cargo-loaded SRP (Fig. 4.4a): (1) the initial rates are much faster with cargo-loaded SRP; (2) the kinetics of complex formation with cargo-loaded SRP is bi-phasic with a burst phase, suggesting the accumulation of an intermediate; (3) at completion of the reaction, FRET plateaus at a lower value for cargo-loaded SRP, suggesting a change in the equilibrium stability of the final SRP–SR complex. These effects are further characterized in the following.

An observed rate constant for complex formation (k_{obsd}) at any protein concentration is the sum of the complex assembly and disassembly rate constants [22].

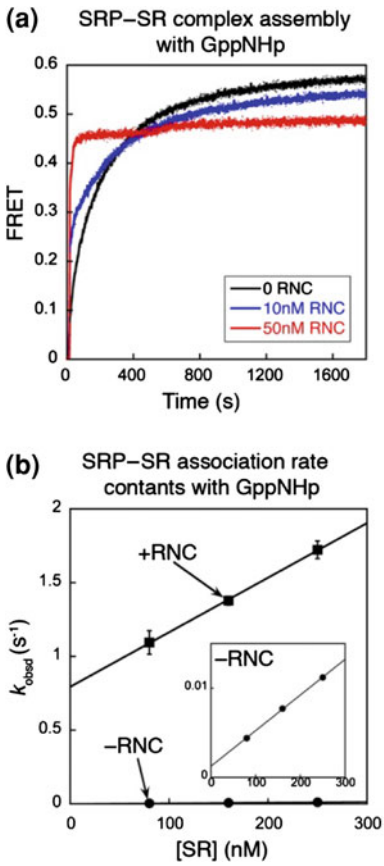

Fig. 4.4 Cargo changes the kinetics of SRP–SR interaction. **a** Time courses for SRP–SR complex assembly with GppNHp in the absence (*black*) or presence of 10 nM (*blue*) and 50 nM (*red*) RNC, using 10 nM SRP and 100 nM SR to mimic physiological protein concentrations [21]. **b** Cargo accelerates SRP–SR complex assembly with GppNHp by 100-fold. The data are fit to the equation: $k_{obsd} = k_{on}[SR] + k_{off}$, and gave association rate constants (k_{on}) of $3.7 \pm 0.4 \times 10^6$ M^{-1} s^{-1} and $4.0 \pm 0.3 \times 10^4$ M^{-1} s^{-1} with (*closed squares*) and without (*closed circles*) 60 nM RNC, respectively

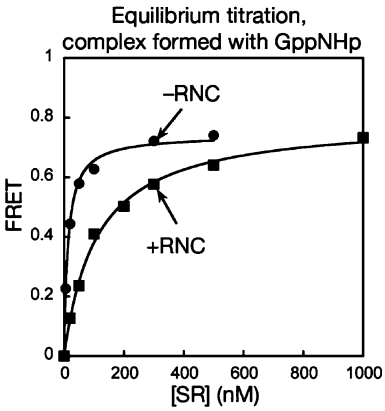

Fig. 4.5 Equilibrium titration of the SRP–SR complex assembled in GppNHp with (*closed squares*) and without (*closed circles*) RNC using the FRET assay. Nonlinear least squares fits of data gave K_d values of 14 ± 3 nM (without RNC) and 60 ± 7 nM (with RNC). For cargo-loaded SRP, an accurate determination of the stability of the *closed/activated* states by FRET is complicated by the fact that the stabilities of the SRP–SR complexes assembled with and without GppNHp are very similar (60 vs. 80 nM, respectively), thus a significant fraction of the SRP–SR complex is in the *early* conformation even in the presence of GppNHp. The observed affinity of the cargo–SRP–SR complex of 60 nM is consistent with the weighted average of the stabilities of the *early* intermediate (80 nM, Fig. 4.7c) and the *closed* complex (40 nM, Fig. 4.7c) that are equally populated in the presence of GppNHp and cargo

$$k_{obsd} = k_{on} \times [SR] + k_{off}. \tag{4.1}$$

To isolate the effect of cargo on complex assembly, we measured the observed rate constants as a function of SR concentration; the slope of this concentration dependence gives the association rate constant, k_{on} [Eq. (4.1); Fig. 4.4b]. The value of k_{on} is 4.4×10^4 M^{-1} s^{-1} in the absence of cargo, consistent with previous measurements [10]. In the presence of cargo, the complex formation rate constant is 100- to 400-fold faster (Figs. 4.4b and 4.5). Thus cargo-loaded SRP has a substantial kinetic advantage over free SRP to form a complex with the SR, ensuring efficient delivery of cargo to the target membrane.

4.2.3 Cargo Stabilizes the Early Intermediate by Two Orders of Magnitude

The biphasic kinetics with a burst phase during complex formation with cargo-loaded SRP suggests the accumulation of an intermediate (Figs. 4.4a and 4.6a, blue). A likely candidate to account for this burst is the *early* intermediate, which forms quickly and has a lower FRET value than the subsequent complexes (Fig. 4.1) [16]. To test this notion, we blocked the *early* → *closed* rearrangement

and isolated the *early* complex by performing complex assembly in the absence of nucleotide (Fig. 4.1, step 2; Fig. 4.6a, green). Both the rate and the magnitude of FRET changes for assembly of the *early* intermediate agree well with those of the burst phase during complex assembly with GppNHp (Fig. 4.6a). This provides strong evidence that in the presence of cargo, the *early* intermediate accumulates substantially during complex assembly.

The *early* intermediate, which lacks stabilizing interactions from the γ-phosphate of GTP, is very unstable without cargo [5, 16], hence it cannot accumulate under the nanomolar concentrations of SRP and SR used here (Fig. 4.4a, black). Therefore it was surprising to detect its accumulation with cargo-loaded SRP. This observation suggests that the cargo strongly stabilizes this intermediate. To test this hypothesis, we determined the equilibrium and kinetic stability of the *early* complex with and without cargo. Indeed, the cargo stabilizes the *early* complex over 50-fold, lowering its equilibrium dissociation constant (K_d) from 4 to 10 microM [16] to 80 ± 4 nM (Fig. 4.6b, squares) and decreasing its dissociation rate constant (k_{off}, derived from the y-intercept in Fig. 4.6c) from 62 ± 2 s^{-1} to 1.6 ± 0.1 s^{-1}.

Stabilization of the *early* intermediate explains the faster rate of SRP–SR complex assembly with GppNHp for cargo-loaded SRP (Fig. 4.4b). Without cargo, formation of the highly labile *early* intermediate is not sufficient to give a stable SRP–SR complex; to obtain a stable complex, the *early* intermediate needs to rearrange to the *closed* complex. However the *early* intermediate dissociates quickly and less than 2% of the population rearranges to form the *closed* complex (k_{off} = 62 ± 2 s^{-1} vs $k_{rearrange}$ = 1.03 ± 0.02 s^{-1}) [16]. This gives rise to the slow rate constant for formation of a stable *closed* complex between free SRP and SR. In contrast, for cargo-loaded SRP the *early* intermediate is stabilized over 50-fold. Thus forming the *early* complex (Fig. 4.1, step 1) is sufficient to give a relatively stable SRP–SR complex under physiological SRP and SR concentrations (200–400 nM) [21]. Furthermore, the cargo–SRP–SR *early* complex dissociates with much slower kinetics (Fig. 4.6c, k_{off} = 1.6 ± 0.1 s^{-1}), giving this intermediate a much longer lifetime to undergo subsequent rearrangements. Both of these effects contribute to the faster rate of assembling a stable GTPase complex with cargo-loaded SRP in the presence of GppNHp.

4.2.4 Cargo Stalls the SRP–SR Complex at Earlier Conformational Stages

The different FRET end points in Fig. 4.4a suggest that the stability of the final SRP–SR complex is also altered by the cargo. To test this hypothesis, we compared the equilibrium stability of the SRP–SR complex assembled in GppNHp with and without cargo using SRP C235 labeled with acrylodan (Figs. 4.1 and 4.2). Equilibrium titrations using this probe showed that the cargo destabilizes the

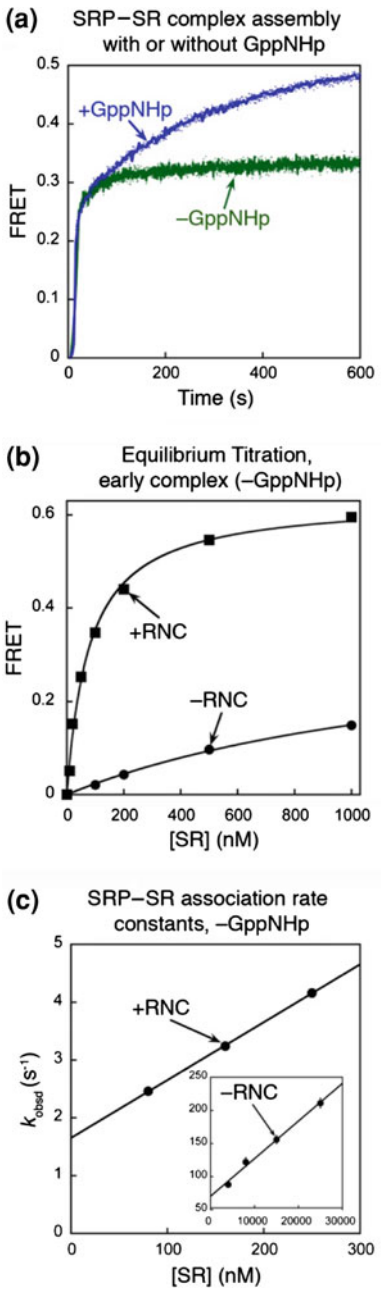

Fig. 4.6 Cargo stabilizes the early intermediate. **a** Comparison of the time courses for SRP–SR complex formation for cargo-loaded SRP in the absence (*green*) and presence of 100 microM GppNHp (*blue*). Data were obtained using 20 nM SRP, 100 nM SR and 20 nM RNC. **b** Cargo stabilizes the *early* intermediate 50-fold. Equilibrium titration of the *early* complex assembled in

◀ **Fig. 4.6** (continued)
the absence of GppNHp with (*closed squares*) and without (*closed circles*) 50 nM RNC. Nonlinear fits of data gave K_d values of 80 ± 4 nM in the presence of RNC. **c** Cargo increases the kinetic stability of the *early* intermediate 40-fold. The data are analyzed as in **b** and give $k_{on} = 1.0 \pm 0.1 \times 10^7\ M^{-1}\ s^{-1}$ with cargo-loaded SRP, which is within twofold of the value in the absence of RNC ($k_{on} = 5.6 \pm 0.3 \times 10^6\ M^{-1}\ s^{-1}$) [16], and $k_{off} = 1.62 \pm 0.1\ s^{-1}$, which is 40-fold slower than that in the absence of RNC ($k_{off} = 60 \pm 2\ s^{-1}$) [16]. The *inset* shows the data in the absence of RNC (adapted from Ref. [16]). Note the difference in scales between the two plots

closed/activated complexes fourfold, increasing its K_d from 10 ± 2 nM to 40 ± 4 nM (Fig. 4.7a). A similar destabilizing effect was observed using the FRET probes, with the K_d of the *closed/activated* increasing from 14 ± 3 nM without cargo to 60 ± 7 nM with cargo-loaded SRP (Fig. 4.8). An additional probe that specifically monitors the *activated* complex, acrylodan-labeled SR C356 (Figs. 4.1 and 4.3), also confirmed that the cargo destabilizes the *activated* complex (Fig. 4.7b). In summary, the results from all three fluorescence probes showed that, in contrast to the large stabilizing effect of the cargo on the *early* intermediate, the subsequent conformations during the SRP–SR interaction are destabilized by the cargo.

Thus the cargo significantly alters the conformational rearrangements in the SRP–SR complex (Fig. 4.7c). Without cargo, the *closed* and *activated* states are >400-fold more stable than the *early* intermediate, therefore the equilibrium for the *early* → *closed* rearrangement is extremely favorable (Fig. 4.7c, $K^{rel} = 400$). In contrast, in the cargo–SRP–SR complex this rearrangement is 200-fold less favorable (Fig. 4.7c, $K^{rel} = 1.3–2$). Thus in the cargo–SRP–SR complex, a substantial fraction of the GTPase complex is still in the *early* conformation (30–40%) even in the presence of GppNHp. This conformational heterogeneity of the GTPase complex in the presence of cargo is consistent with previous EM analysis that showed that, while the SRP is well-resolved in the RNC–SRP complex, upon addition of SR and GppNHp the electron density for both the SRP and SR's GTPase domains are no longer visible [23]. Thus both the biochemical and structural analyses highlight the dynamic nature of the GTPase complex when it is bound to the cargo.

The SRP–SR complex can use the *early* → *closed* rearrangement to drive cargo unloading during protein targeting (Fig. 4.7d). Initially, cargo loading stabilizes the *early* intermediate 50-fold (Fig. 4.7d, K_d and K_d'). Correspondingly, the interaction of cargo with SRP should be stabilized to the same extent in the *early* intermediate (Fig. 4.7d, $K_d^{RNC'}/K_d^{RNC} = K_d'/K_d = 50$). Using the value of $K_d^{RNC} \sim 1$ nM [24, 25], the stability of cargo bound to the *early* intermediate would be in the range of $K_d^{RNC'} \sim 20$ pM. Although this effect could enhance the initial recognition and delivery of cargo to the membrane, such strong binding will block the subsequent unloading of cargo from the SRP. This problem is circumvented by the 200-fold destabilizing effect of cargo on the *early* → *closed*

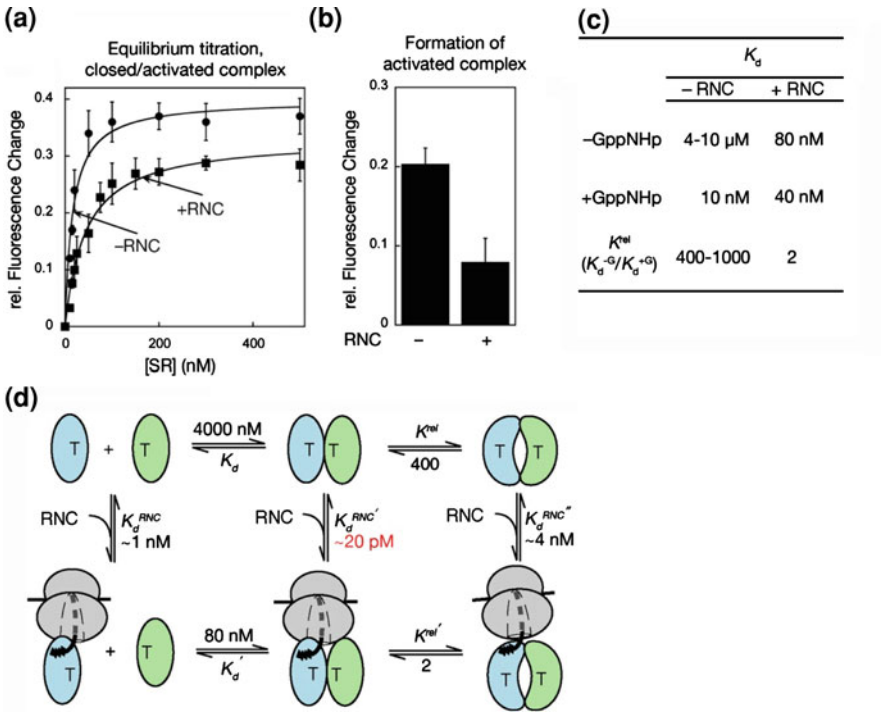

Fig. 4.7 Cargo destabilizes the *closed* and *activated* states during SRP–SR interaction. **a** Equilibrium titration of the SRP–SR complex assembled in GppNHp with (*closed squares*) and without (*closed circles*) RNC using acrylodan-labeled SRP C235. Nonlinear fits of data gave K_d values of 10 ± 2 nM (without RNC) and 40 ± 4 nM (with RNC). **b** Relative fluorescence changes of acrylodan-labeled SR C356 in the presence and absence of cargo, obtained using 50 nM SRP and 15 nM labeled SR with 100 microM GppNHp. An accurate K_d value could not be determined with this probe because of the large amount of cargo-loaded SRP that would be required to saturate labeled SR C356. **c** Equilibrium constants of the GTP-independent (K_d^{-G}) and GTP-dependent (K_d^{+G}) SRP–SR complexes with or without RNC. The equilibrium for rearrangement (K^{rel}) were calculated from $K^{rel} = K_d^{-G}/K_d^{+G}$. **d** Thermodynamic analysis of the interaction of cargo with SRP at different conformational stages during the SRP–SR interaction

rearrangement (Fig. 4.7c, d, K^{rel} and $K^{rel'}$). Correspondingly, the interaction of cargo with SRP would also be weakened 200-fold by this rearrangement (Fig. 4.7c, $K_d^{RNC''}/K_d^{RNC} = K^{rel'}/K^{rel}$), thus priming the cargo for subsequent unloading. This model is supported by mutational analyses that showed that mutant GTPases defective in the *early* → *closed* rearrangement severely block protein translocation [17]. The observation that mutants defective in the *closed* → *activated* rearrangement inhibit protein translocation further suggest that this last rearrangement is also essential for cargo unloading [17]. Therefore both rearrangements within the GTPase complex provide essential driving forces

to help unload the cargo from the SRP to the PCC, thus initiating protein translocation.

Since cargo disfavors the rearrangements to form the *activated* complex, one would predict that stimulated GTP hydrolysis, which occurs from the *activated* complex, would also be impaired. To test this notion, we compared the GTPase reaction rate from the SRP–SR complex in the presence and absence of cargo. In the absence of cargo, the GTPase rate of free SRP is significantly stimulated by the addition of SR (Fig. 4.9, closed circles). The reaction rate reaches a plateau of 0.79 s^{-1} at saturating SR concentrations, representing the GTPase rate constant from the SRP–SR complex (Fig. 4.9, closed circles). In the presence of cargo, significantly less GTPase stimulation was observed (Fig. 4.9, closed squares). Intriguingly, two plateaus were observed for the GTPase reaction in the presence of cargo (Fig. 4.9, closed squares), suggesting the presence of two populations of cargo–SRP–SR complexes: one population, which forms at low SR concentrations (below 50 nM), hydrolyzes GTP at a rate constant of 0.064 s^{-1}; the second population, which forms at higher SR concentrations (above 1 microM), hydrolyzes GTP at a rate constant of 0.11 s^{-1} (Fig. 4.9, closed squares). Although the nature of this heterogeneity is unclear at present, in both of these populations the GTPase activity is repressed by the RNC (12- and 8-fold for the first and second population, respectively). The effect of cargo in reducing the GTP hydrolysis rate is specific to the SRP–SR complex, as the cargo does not affect the basal GTP hydrolysis rate of free SRP. Thus the cargo also delays GTPase activation in the SRP–SR complex. This effect, which we term 'stalling', would provide an important time window that allows the SRP to unload the cargo before GTP hydrolysis drives irreversible complex disassembly, as discussed below.

4.3 Discussion

We showed here that cargo loading substantially alters the free energy landscape of the SRP–SR interaction cycle (Fig. 4.10a). Without cargo (black), assembly of a stable SRP–SR complex is slow because it requires rearrangement from an unstable *early* intermediate (Fig. 4.10a, $\Delta G^{\ddagger}_{complex} = \Delta G_{early} + \Delta G^{\ddagger}$) [16]. Further, the stable SRP–SR complex has a short lifetime because as soon as it is formed, rapid activation of GTP hydrolysis drives its irreversible disassembly [8]. The cargo uses a remarkably simple solution to these problems, by stabilizing the *early* intermediate (Fig. 4.10a, $\Delta\Delta G = -2.4$ kcal/mol) and disfavoring the *closed* and *activated* states (Fig. 4.10a, $\Delta\Delta G \geq +0.8$ kcal/mol). This accelerates complex assembly (Fig. 4.10a, $\Delta\Delta G^{\ddagger} = -2.8$ kcal/mol), and prolongs the lifetime of the SRP–SR complex due to delayed GTP hydrolysis (Fig. 4.10a, $\Delta\Delta G^{\ddagger} = +1.3$–1.5 kcal/mol). The rate-limiting step of the SRP–SR interaction cycle shifts from the *early* → *closed* rearrangement with free SRP to GTP hydrolysis with cargo-loaded SRP.

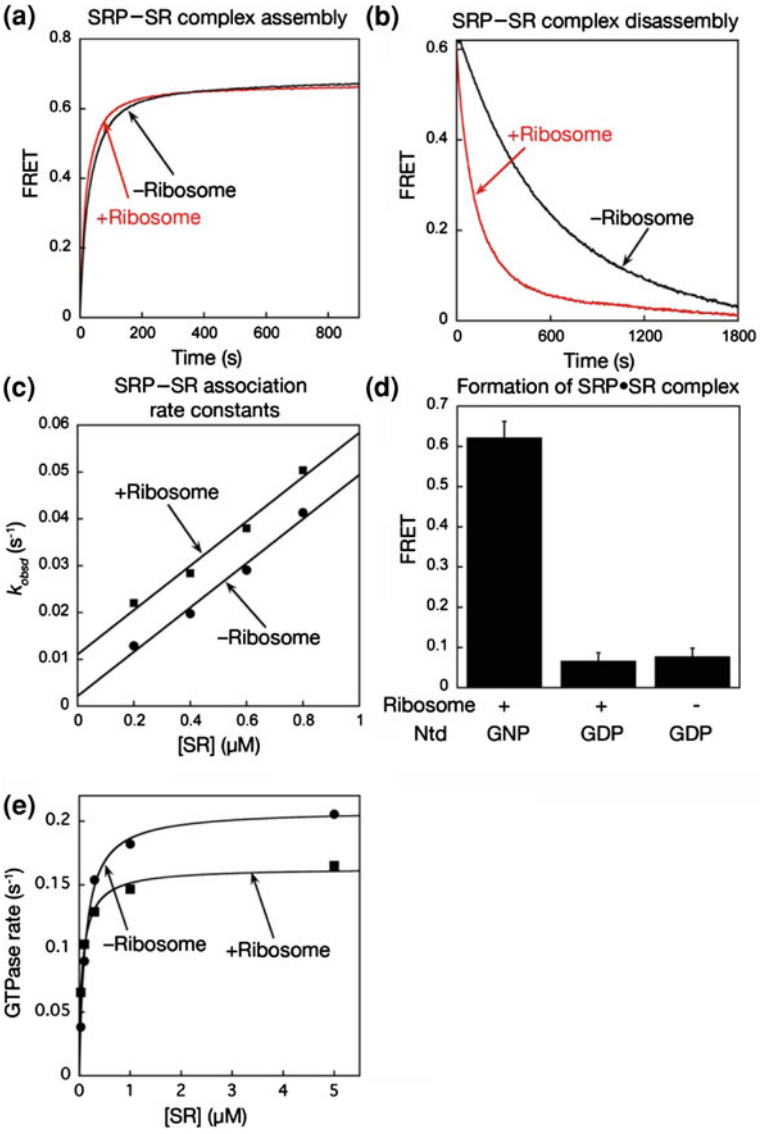

Fig. 4.8 Empty ribosomes do not substantially alter the interaction between SRP and SR. **a** The time course for SRP–SR complex formation, monitored by FRET, in the absence (*black*) and presence (*red*) of 0.8 microM ribosomes. Data were obtained with 0.1 microM SRP, 1.0 microM SR, and 100 microM GppNHp. **b** The ribosome accelerates disassembly of the SRP–SR complex of approximately threefold. The rate constants for complex disassembly were determined in the absence (*black*) and presence (*red*) of 1.0 microM ribosomes. Fits of the data to single exponential decay give dissociation rate constants of 0.010 ± 0.003 s^{-1} and 0.0027 ± 0.004 s^{-1} in the presence and absence of ribosome, respectively. **c** The ribosome does not affect the rate of SRP–SR complex assembly. Association kinetics of the SRP–SR complex was measured as in Fig. 4.4 with (*closed squares*) or without (*closed circles*) 1.0 microM ribosome. Linear fits of the

◀ **Fig. 2.8** (continued)
data gave k_{on} values of 4.7 ± 0.7 × 10^4 M^{-1} s^{-1} with ribosome and 4.7 ± 0.4 × 10^4 M^{-1} s^{-1} without ribosome, and k_{off} values of 0.011 ± 0.004 s^{-1} with ribosome and 0.0022 ± 0.003 s^{-1} without ribosome. **d** Ribosome does not stabilize the *early* intermediate. FRET values are compared for SRP–SR *early* complex assembled with GDP in the presence and absence of ribosome. Data are obtained with 0.1 microM SRP, ribosome, and 1.0 microM SR. **e** Ribosome does not substantially affect the stimulated GTP hydrolysis on the SRP–SR complex. GTPase rate constants were measured and analyzed as described in Methods using 15 nM SRP and 50 microM GTP in the absence (*closed circles*) and presence (*closed squares*) of 1.0 microM ribosome

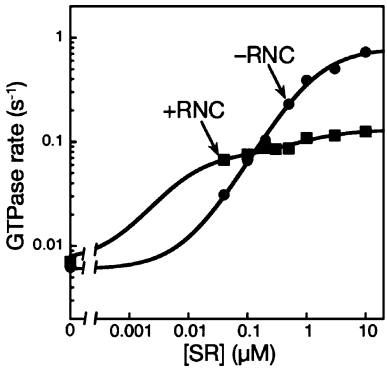

Fig. 4.9 Cargo delays activation of GTP hydrolysis in the SRP–SR complex. GTPase rate constants were measured using 40 nM SRP and 100 microM GTP in the absence (*closed circles*) and presence (*closed squares*) of 100 nM RNC. The data in the absence of cargo were fit to a single binding curve and gave a rate constant of 0.79 s^{-1} for GTP hydrolysis from the SRP–SR complex. The data in the presence of cargo is not consistent with a single binding curve and was fit to a model based on two populations of SRP–SR complexes that reacts at rate constants of 0.064 and 0.11 s^{-1}

These cargo-induced effects allow the SRP and SR to use each of their conformational rearrangements to regulate a distinct step during protein targeting (Fig. 4.10b). At the beginning of each targeting cycle, cargo loading (Fig. 4.10b, step 1) allows the SRP to assemble a stable complex with SR > 100-fold faster (Fig. 4.10b, step 2). This ensures rapid delivery of cargo to the membrane [26, 27], and avoids futile interactions between free SRP and SR. In the *early* intermediate, the cargo is locked in the SRP–SR complex with very high affinity (Fig. 4.7d, $K_d^{RNC'} \sim 20$ pM), allowing the SRP to effectively compete with cellular chaperones for binding the cargo. Subsequent GTPase rearrangements to the *closed* and *activated* conformations weaken the interaction of cargo with the SRP (Fig. 4.10b, steps 3–4; and Fig. 4.7d) and thus help the SRP to switch from a cargo-binding mode to a cargo-release mode, to unload the cargo to the PCC (Fig. 4.10b, step 4). Once in the *activated* conformation, and especially after cargo release, rapid GTP hydrolysis drives the disassembly and recycling of SRP and SR (Fig. 4.10b, step 5).

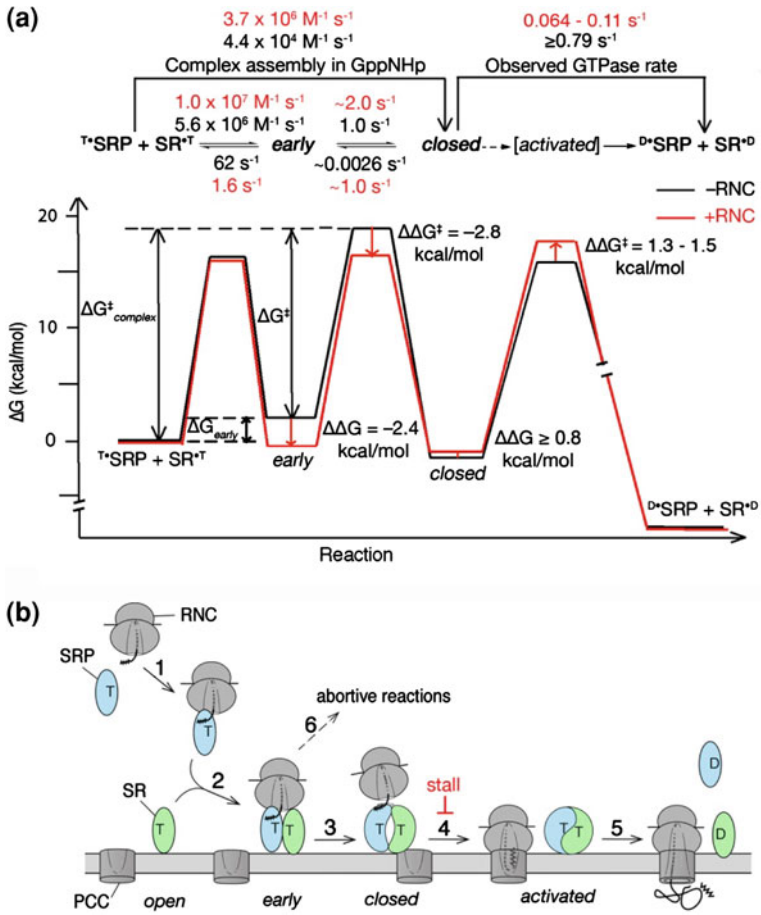

Fig. 4.10 Conformational changes during the SRP–SR interaction respond to cargo loading and regulate protein targeting. **a** Rate constants and free energy profile for the SRP–SR interaction in the absence (*black*) and presence (*red*) of cargo. A standard state of 200 nM SRP is used to approximate cellular protein concentrations. Activation energies were calculated from the observed association and dissociation rate constants using $\Delta G^{\ddagger} = -RT\ \ln(kh/k_BT)$, where R = 1.987 cal K^{-1} mol^{-1}, $h = 1.58 \times 10^{-37}$ kcal s^{-1}, $k_B = 3.3 \times 10^{-27}$ kcal K^{-1}, and T = 298 K. The relative energies of the different complexes were calculated from the observed equilibrium stabilities using $\Delta G = -RT\ \ln K$, where K is the equilibrium constant. ΔG_{early} is the free energy cost to form the *early* complex, $\Delta G^{\ddagger}$ is the activation energy for the *early* → *closed* rearrangement. The sum of these two gives the overall energy barrier to form the *closed* complex ($\Delta G^{\ddagger}_{complex}$), which is lowered 2.8 kcal mol^{-1} by the cargo because the cargo stabilizes the *early* complex by 2.4 kcal mol^{-1}. In contrast, the RNC increases the activation energy for GTP hydrolysis by 1.9 kcal mol^{-1}. **b** Proposed model for how the conformational changes during the SRP–SR interaction regulate protein targeting and translocation as described in text

The mechanism proposed here (Fig. 4.10b) focuses on GTP-bound SRP and SR because the high cellular concentration of GTP compared to GDP (∼900 and 100 microM in bacteria, respectively) predicts that over 90% of both GTPases are

bound with GTP. Minor pathways are also possible in which empty-site or GDP-bound forms of SRP and SR first form the *early* intermediate to deliver cargo to the membrane surface, followed by rapid binding or exchange of GTP to drive the subsequent steps [26, 27]; these pathways are not depicted in Fig. 4.10b for clarity.

The most intriguing effect of cargo is 'stalling', i.e., the delay of GTPase activation by $\sim$8- to 12-fold (Fig. 4.10b, step 4). A similar effect was suggested from studies of the mammalian system where prior to the addition of the PCC, a stable cargo–SRP–SR complex persists in the presence of GTP, suggesting that the cargo may also delay GTP hydrolysis in the mammalian SRP–SR complex [28]. We suggest that stalling creates an important time window during which SRP ensures the efficiency and fidelity of protein targeting, via either or both of the following mechanisms. First, stalling could provide a spatial checkpoint for the target membrane and/or the PCC. Before the SR associates with the PCC, stalling prevents premature GTP hydrolysis that would irreversibly disassemble the SRP–SR complex, and thus help avoid abortive targeting reactions (Fig. 4.10b, step 6). Interaction of SR with the PCC may trigger the rearrangement to the *closed* and *activated* states and initiate cargo unloading [28]. The PCC also competes with SRP for interacting with the RNC [19, 20, 23, 29], which could further drive the transfer of cargo from SRP to the PCC [28, 30]. Alternatively, stalling could provide a fidelity checkpoint. Many of the effects of the cargo described here are observed only with RNCs but not with empty ribosomes (Fig. 4.8) nor with RNCs bearing weak signal sequences, establishing the importance of the signal sequence. It could be envisioned that cargos with weaker signal sequences could not effectively stall the SRP–SR complex, and thus are more likely to be rejected via premature GTP hydrolysis (Fig. 4.10b, step 6). In this way, GTP hydrolysis could be used to improve the fidelity of protein targeting akin to kinetic proofreading mechanisms used by elongation factor [31].

4.4 Materials and Methods

4.4.1 Materials

The *Eschericia coli* SRP and SR GTPases (Ffh and FtsY, respectively) and 4.5S RNA were expressed and purified using established procedures [8, 17]. Most of the fluorescence experiments used the FtsY(47–497) construct. This truncated FtsY construct behaves similarly to full length FtsY in its ability to interact with the SRP and to respond to the cargo. The GTPase reactions with and without cargo was determined with full length FtsY. Mutant proteins were constructed using the QuickChange procedure (Stratagene, La Jolla, CA), and were expressed and purified by the same procedure as that for the wild-type protein. Fluorescent dyes DACM, BODIPY-FL and acrylodan were from Invitrogen (Carlsbad, CA). 70S ribosomes and RNCs were purified as described previously [18, 32, 33].

4.4.2 Fluorescence Labeling

For FRET measurements, maleimide derivatives of coumarin and BODIPY-FL were used to label single-cysteine mutants of SRP and SR, respectively, as described [16]. Labeling of SRP and SR with acrylodan followed the same procedure except that the labeling reaction was carried out using a 30-fold excess of dye over protein for over 12 h at 4 °C. Absorbance of acrylodan (e_{391} = 20,000 M^{-1} cm^{-1}) was used to determine the concentration of labeled protein. The efficiency of labeling reaction was typically ≥90% for both proteins. The background, estimated from the labeling of cysteinless SRP and SR using the same procedure, is less than 3%.

4.4.3 Fluorescence Measurement

All measurements were carried out at 25 °C in assay buffer [50 mM KHEPES, pH 7.5, 150 mM KOAC, 10 mM $Mg(OAc)_2$, 2 mM DTT, 0.01% Nikkol] on a Fluorolog-3 spectrofluorometer (Jobin–Yvon, Edison, NJ) as described [8, 16]. FRET measurements were carried out using an excitation wavelength of 380 nm and an emission wavelength of 470 nm. FRET efficiency was calculated as described [16]. Fluorescence emission spectrum of SRP (or SR) labeled with acrylodan was measured using an excitation wavelength of 370 nm. Fluorescence emission at 500 nm was monitored for equilibrium titrations using acrylodan-labeled protein.

Pulse chase experiments were carried out using unlabeled protein to trap any dissociated protein SRP or SR [10]. Fast reactions were measured on a Kintek stop-flow apparatus [10]. The incubation time during equilibrium measurements was calculated based on the SRP–SR complex assembly rate [10, 16], and varies from 5 min for fast reactions (*early* complex assembly and complex assembly in the presence of cargo) to several hours (complex assembly with GppNHp in the absence of cargo).

4.4.4 GTPase Assay

The GTPase assay to measure the stimulated GTP hydrolysis reaction between SRP and SR were carried out and analyzed as described [8]. Multiple turnover reactions were carried out at 25 °C with a small, fixed amount of free or cargo-loaded SRP and increasing concentrations of SR, 100 microM GTP (doped with trace γ-^{32}P-GTP) was present in the reaction to saturate both GTPase sites. Previous studies have established that the GTPase reaction rate is rate-limited by SRP–SR complex formation at subsaturating SR concentrations, whereas at saturating SR concentrations, the reaction is rate-limited by GTP hydrolysis or a

slow conformational change preceding GTP hydrolysis [8]. The release of products, including dissociation of GDP, P_i, and disassembly of the ^{GDP}SRP–SR^{GDP} complex, are not rate-limiting for the GTPase assay [8].

4.4.5 Preparation of 70S Ribosomes and RNCs

70S empty ribosomes were purified from *E. coli* MRE600 following a modified protocol described by Moazed and Noller [33]. Cell pellet from a 1 L culture was resuspended in 30 mL buffer A [20 mM Tris–HCl (pH 7.0 at 21 °C), 10.5 mM $MgCl_2$, 100 mM NH_4Cl, 0.5 mM EDTA, 6 mM 2-mercapto ethanol (βME)]. The cell resuspension was passed through the French Press twice to lyse the cells. The lysate was clarified by two rounds of centrifugation at 20,000 × *g* for 15 min at 4 °C. The supernatant was layered on a 1.1 M sucrose cushion in buffer B [20 mM Tris–HCl (pH 7.0 at 21 °C), 10.5 mM $MgCl_2$, 500 mM NH_4Cl, 0.5 mM EDTA, 6 mM βME, 1.1 M sucrose] and ultracentrifuged at 100,000 × *g* for 21 h at 4 °C. The ribosome pellet was collected and dissolved in buffer A containing 500 mM NH_4Cl. The dissolved ribosomes were ultracentrifuged at 4 °C for 3 h at 100,000×*g*. The pellet was dissolved in buffer C [20 mM Tris–HCl (pH 7.0 at 21 °C), 6 mM $MgCl_2$, 100 mM NH_4Cl, 6 mM βME], layered on top of 32-mL sucrose gradients (10–40% w/v sucrose in buffer C), and ultracentrifuged at 50,000×*g* for 14 h at 4 °C. Fractions containing 70S ribosomes were collected and ultracentrifuged at 100,000×*g* for 17 h at 4 °C. Ribosome pellets were collected and dissolved in storage buffer [20 mM Tris–HCl (pH 7.0 at 21 °C), 10 mM $MgCl_2$, 100 mM NH_4Cl, 6 mM βME]. Ribosomes were stored at −80 °C.

The RNC was generated from in vitro translation in a membrane-free cell extract prepared from *E. coli* MRE600 as described [18]. In vitro translation was performed at 37 °C for 25 min. The translation mix was layered onto a 40-mL sucrose gradient in buffer S1 (10–50% w/v sucrose in 50 mM HEPES–KOH (pH 7.5 at 4 °C), 100 mM $Mg(OAc)_2$, 100 mM NH_4Cl) and ultracentrifuged at 4 °C for 15 h at 23,500 rpm using a SW-32 rotor (Beckman). Fractions containing monoribosome were collected and loaded onto a 1-mL Strep-Tactin Sepharose column (IBA, Göttingen Germany) equilibrated with buffer S1 at 4 °C. Buffer S1 containing 2.5 mM desthiobiotin (Sigma) was used to elute RNCs from affinity column. RNC-containing fractions were centrifuged at 55,000 rpm for 3 h at 4 °C using a TLA-55 rotor (Beckman). Pellets were collected and dissolved in buffer S1 with 25 mM $Mg(OAc)_2$.

Acknowledgments We thank Sandra Schmid, Douglas C. Rees, Raymond Deshaies, Nathan Pierce, and members of the Shan Laboratory for comments on the manuscript. This work was supported by NIH grant GM078024 to S.S., and by the Swiss National Science Foundation (SNSF) and the NCCR Structural Biology program of the SNSF to N.B. S.S. was supported by a career award from the Burroughs Welcome Foundation, the Henry and Camille Dreyfus foundation, the Beckman Young Investigator award, and the Packard and Lucile award in science and engineering. X.Z. was supported by a fellowship from the Ulric B. and Evelyn L. Bray Endowment Fund.

References

1. Walter P, Johnson AE (1994) Annu Rev Cell Biol 10:87
2. Matlack KES, Mothes W, Rapoport TA (1998) Cell 92:381
3. Johnson AE, van Waes MA (1999) Annu Rev Cell Dev Biol 15:799
4. Bourne HR (1986) Nature 321:814
5. Focia PJ, Gawronski-Salerno J, Coon JS, Freymann DM (2006) J Mol Biol 360:631
6. Freymann DM, Keenan RJ, Stroud RM, Walter P (1999) Nat Struct Biol 6:793
7. Freymann DM, Keenan RJ, Stroud RM, Walter P (1997) Nature 385:361
8. Peluso P, Shan SO, Nock S, Herschlag D, Walter P (2001) Biochem 40:15224
9. Jagath JR, Rodnina MV, Lentzen G, Wintermeyer W (1998) Biochem 37:15408
10. Peluso P et al (2000) Science 288:1640
11. Shan SO, Stroud RM, Walter P (2004) PLoS Biol 2:1572
12. Egea PF et al (2004) Nature 427:215
13. Shan SO, Walter P (2003) Proc Natl Acad Sci U S A 100:4480
14. Lu Y et al (2001) EMBO J 20:6724
15. Miller JD, Wilhelm H, Gierasch L, Gilmore R, Walter P (1993) Nature 366:351
16. Zhang X, Kung S, Shan SO (2008) J Mol Biol 381:581
17. Shan SO, Chandrasekar S, Walter P (2007) J Cell Biol 178:611
18. Schaffitzel C, Ban N (2007) J Struct Biol 158:463
19. Mitra K et al (2005) Nature 438:318
20. Schaffitzel C et al (2006) Nature 444:503
21. Jensen CG, Pedersen S (1994) J Bacteriol 176:7148
22. Fersht A (1999) Structure and mechanism in protein science: a guide to enzyme catalysis and protein folding. WH Freeman, New York pp. xxi, 631 p
23. Halic M et al (2006) Science 312:745
24. Bornemann T, Jockel J, Rodnina MV, Wintermeyer W (2008) Nat Struct Mol Biol 15:494
25. Flanagan JJ et al (2003) J Biol Chem 278:18628
26. Rapiejko PJ, Gilmore R (1997) Cell 89:703
27. Bacher G, Lutcke H, Jungnickel B, Rapoport TA, Dobberstein B (1996) Nature 381:248
28. Song WQ, Raden D, Mandon EC, Gilmore R (2000) Cell 100:333
29. Halic M et al (2006) Nature 444:507
30. Pool MR, Stumm J, Fulga TA, Sinning I, Dobberstein B (2002) Science 297:1345
31. Rodnina MV, Wintermeyer W (2001) Annu Rev Biochem 70:415
32. Schaffitzel C, Ban N (2007) J Struct Biol 159:302
33. Moazed D, Noller HF (1989) Cell 57:585

Chapter 5
Sequential Checkpoints Govern Substrate Selection During Co-translational Protein Targeting

5.1 Introduction

Co-translational protein targeting by the SRP is an essential and evolutionarily conserved pathway for delivering proteins to cellular membranes [1, 2]. SRP recognizes ribosomes translating nascent polypeptide chains (RNCs) as its cargo (Fig. 5.1a, step 1) [1–6]. Cargo loading enables efficient assembly of an SRP–SR complex through interactions between their GTPase domains, and the cargo stabilizes the GTPase complex in an *early* conformational state (step 2) [7, 8]. The interactions of SR with the target membrane and the protein conducting channel (PCC) is proposed to induce dynamic rearrangements in the SRP–SR complex [4, 6, 8], first to form a GTP-dependent *closed* complex (step 3) and then to activate GTP hydrolysis in the complex (step 4). These rearrangements facilitate the unloading of cargo from SRP to the PCC (steps 3–4) [4, 6, 8]. In a productive targeting cycle, GTP is hydrolyzed after cargo unloading to drive the disassembly and recycling of SRP and SR (step 5) [9].

Despite significant progress in our dissection of the SRP pathway as a paradigm for understanding the molecular basis of protein localization, how the SRP ensures faithful delivery of correct cargos remains poorly understood. Like other topogenic sequences that mediate protein localization, signal sequences that engage the SRP lack a consensus motif and are highly divergent [10–12], with a hydrophobic core as their primary distinguishing feature [11, 13]. Thus the SRP needs to be highly adaptable; indeed it was proposed that the methionine-rich M-domain of SRP provides a flexible pocket to accommodate diverse signal sequences [14, 15]. Nevertheless, the difference in signal sequences of substrates that engage SRP vs. SRP-independent pathways are relatively minor [16]. Thus despite its flexibility, the SRP has evolved a strategy to remain highly specific to its substrates. Here we

A separate version of this chapter has been published as a Report in Science on May 7th, 2010 (Zhang X, Rashid R, Wang K, Shan SO (2010) Science 328:757–760).

X. Zhang, *Multistate GTPase Control Co-translational Protein Targeting*,
Springer Theses, DOI: 10.1007/978-1-4419-7808-0_5,

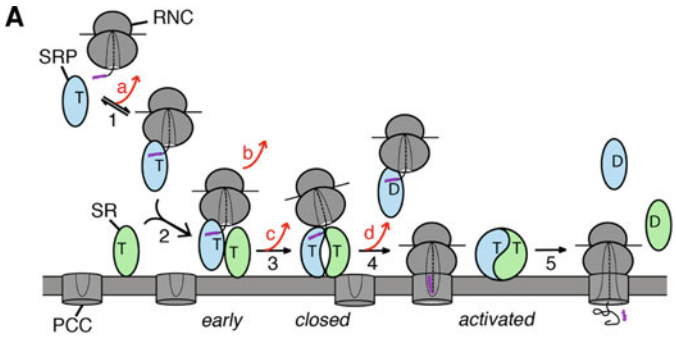

B

phoA-1A9L	MKQST**LALLLLLLLL**TPVTKA
phoA-2A8L	MKQST**LALLLLLALL**TPVTKA
phoA-3A7L	MKQST**LALLLLLALA**TPVTKA
phoA-WT	MKQST**IALALLPLLF**TPVTKA
phoA-5A5L	MKQST**LALALALALA**TPVTKA
phoA-8A2L	MKQST**LAAAAAAALA**TPVTKA
EspP	MNKIYSLKYSHITGGLIAVSELSGRVSSRATG KKKHKR**ILALCFLGLL**QSSYSFA
luciferase	MEDAKNIKKGPAPFYPLEDGT

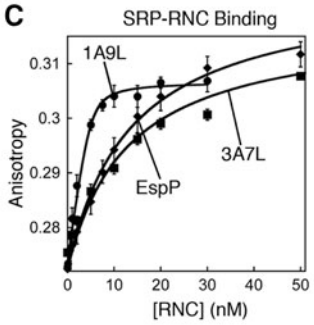

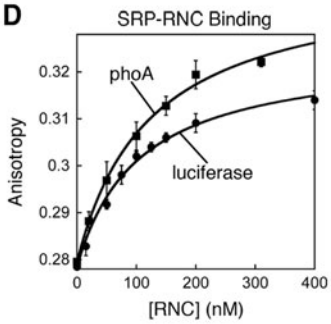

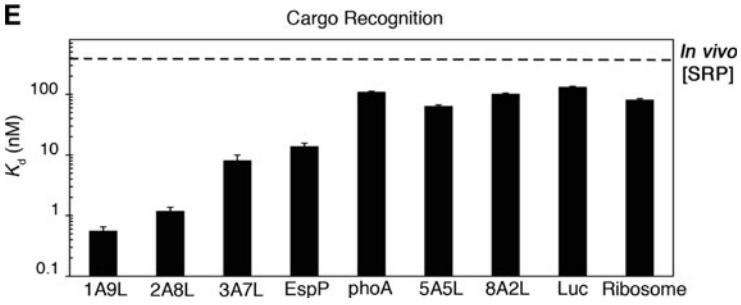

◀ **Fig. 5.1** Potential fidelity checkpoints in the SRP pathway. **a** Model for potential checkpoints during co-translational protein targeting. A cargo bearing a signal sequence (*magenta*) enters this pathway upon binding the SRP, and is either retained (*black arrows*) or rejected (*red arrows*) at each checkpoint. T and D denote for GTP and GDP, respectively. **b** Signal sequence variants used in this study. *Bold* highlights the hydrophobic core. *Blue* denotes the unique N-terminal signal peptide extension in EspP. **c**, **d** Equilibrium titrations of SRP–RNC binding. Nonlinear fits of data gave K_d values of 0.55, 8.4, 13.6, 108 and 130 nM for RNC_{1A9L} (**c**, *filled circle*), RNC_{3A7L} (**c**, *filled square*), RNC_{EspP} (**c**, *filled diamond*), RNC_{phoA} (**d**, *filled square*) and $RNC_{luciferase}$ (**d**, *filled circle*), respectively. **e** Summary of the binding affinities of SRP for different cargos. The *dashed line* represents the cellular SRP concentration of ~400 nM

demonstrate that the SRP pathway achieves high fidelity through a combination of binding, induced fit and kinetic proofreading mechanisms.

5.2 Results

It was generally thought that 'incorrect' cargos without strong signal sequences are rejected because they bind weakly to the SRP (Fig. 5.1a, arrow a). To test this hypothesis, we systematically varied the signal sequence based on alkaline phosphatase (phoA), a 'borderline' substrate targeted by either the SRP or SecB pathway [16, 17]. We replaced the hydrophobic core of the phoA signal sequence (Fig. 5.1b, bold) with a combination of leucine and alanine, and varied the Leu/Ala ratio to generate signal sequences with different hydrophobicity [17, 18]. As another means to vary the signal sequence and generate an incorrect cargo, the *E. coli* autotransporter EspP was used. Although the EspP signal peptide has a hydrophobicity comparable to that of phoA-3A7L, EspP enters the PCC via an SRP-independent pathway due to the presence of an N-terminal signal peptide extension (Fig. 5.1b, blue) [19]. Firefly luciferase, a cytosolic protein without any identifiable signal sequences, was used as a negative control (Fig. 5.1b) [17]. For all the following experiments, homogeneous stalled RNCs were purified and used as cargos [8, 20].

We first tested the binding affinities of SRP for different cargos. A single cysteine was engineered into the SRP M-domain (C421) and labeled with 5-maleimide-fluorescein (F5M); RNC binding was detected as an increase in the fluorescence anisotropy of SRP(C421)-F5M. SRP binds tightly to the two cargos with the strongest signal sequences (RNC_{1A9L} and RNC_{2A8L}), with equilibrium dissociation constants (K_d) of ~1 nM or less (Fig. 5.1c and 5.2). These values are similar to that for an SRP model substrate, RNC bearing the FtsQ signal sequence (Fig. 5.2a); thus the behavior of authentic SRP substrates can be recapitulated by the engineered signal sequences. The next strongest cargo, RNC_{3A7L}, also exhibits strong albeit attenuated binding to SRP, with K_d ~10 nM (Fig. 5.1c). Cargos with even weaker signal sequences bind the SRP another tenfold weaker (Figs. 5.1d, e, and 5.2). Nevertheless, the affinity of incorrect cargos or the empty ribosome for SRP is still substantial, with K_d's of 80–100 nM. In comparison, signal peptides

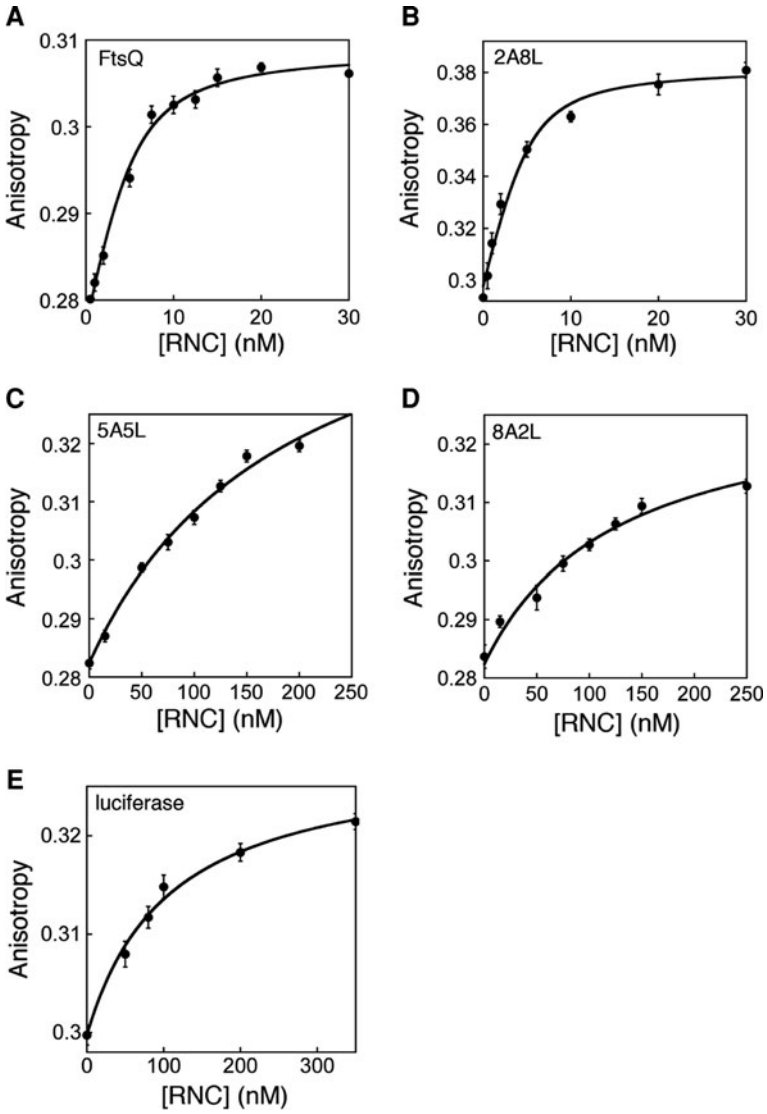

Fig. 5.2 The binding affinities of SRP for different cargos. Equilibrium titrations to measure cargo–SRP binding were carried out as described in Sect. 5.4. K_d values of each cargo (Table 5.1) were derived from quadratic fits of data according to Eq. 5.3. Error bars are SDs from three independent experiments

bind SRP with K_d's in the micromolar range [21, 22]. Thus interactions with the ribosome are important for recruiting the SRP to the cargo [3–5, 23]. As the cellular SRP concentration is $\sim$400 nM [24], at least fourfold higher than the K_d values of SRP for even the weakest cargos (Fig. 5.1e, dashed line), a substantial

amount of incorrect cargos could be bound at this SRP concentration. To our surprise, although EspP is not an SRP substrate, RNC_{EspP} binds SRP as tightly as RNC_{3A7L} (Fig. 5.1c). Thus the differences in cargo binding affinity may not provide sufficient discrimination against incorrect cargos, and additional factors in the bacterial cytosol do not increase the specificity of SRP–cargo binding (Fig. 5.3) [25].

Besides SRP, the PCC also discriminates against incorrect cargos [26, 27]. Nevertheless, the PCC mediates translocation of proteins from both the SRP- and SecB-pathways, including EspP [28], and hence is unlikely to be solely responsible for the stringent substrate selection by the SRP. We postulated that incorrect cargos could be less efficient during subsequent steps of targeting; these steps thereby provide additional checkpoints to help reject incorrect cargos [29]. We tested several potential checkpoints: (i) Formation of the *early* SRP–SR complex (Fig. 5.1a, step 2), an obligatory intermediate preceding the formation of subsequent complexes [7, 8]. This intermediate is highly unstable with free SRP, and >98% of it dissociates before rearranging into the subsequent complex. A strong cargo stabilizes the *early* intermediate and prevents its premature disassembly [8]. If incorrect cargos could not provide such a stabilization, then their *early* targeting complexes would be more likely to disassemble and exit the SRP pathway prematurely (Fig. 5.1a, arrow b). (ii) Rearrangement of the *early* intermediate to the *closed* complex (Fig. 5.1a, step 3), which is essential for switching the SRP from a cargo-binding to a cargo-releasing mode and primes the cargo for unloading [8]. If incorrect cargos were less efficient in this rearrangement, then their late stages of targeting would be delayed (Fig. 5.1a, arrow c). (iii) GTP hydrolysis from the SRP–SR complex, which occurs rapidly in the absence of cargo [30]. A strong cargo could delay GTP hydrolysis, providing the cargo–SRP–SR complex an important time window to search for the target membrane and the PCC before GTP hydrolysis drives the irreversible disassembly of the targeting complex (Fig. 5.1a, steps 4 vs. 5) [8]. If incorrect cargos could not delay GTP hydrolysis as effectively, they would be more likely to be rejected through premature GTP hydrolysis (Fig. 5.1a, arrow d). This would further improve the fidelity of targeting via kinetic proofreading.

To test whether the *early* SRP–SR complex is stabilized more strongly by the correct than the incorrect cargo, we assembled cargo–SRP–SR *early* complexes in the absence of nucleotides; this blocks the rearrangement of the GTPase complex to subsequent conformations and allows us to isolate this intermediate [7, 8]. The equilibrium stabilities of the *early* complexes were measured using fluorescence resonance energy transfer (FRET) between donor- and acceptor-labeled SRP and SR [7]. In this and all the following experiments, saturating RNCs were used to ensure that 80–99% of the SRPs are loaded with cargo, such that differences in cargo binding affinities are bypassed. The *early* complex is significantly stabilized by RNC_{1A9L} and RNC_{2A8L}, with K_d ~80 nM (Fig. 5.4a), and this stability is severely compromised for the weaker cargos (Figs. 5.4b, c, and 5.5). Further, with incorrect cargos such as RNC_{EspP} and $RNC_{luciferase}$, the FRET efficiency plateaus at a lower value, ~0.3–0.4 (Figs. 5.4b, d, and 5.5), compared to ~0.66 with the

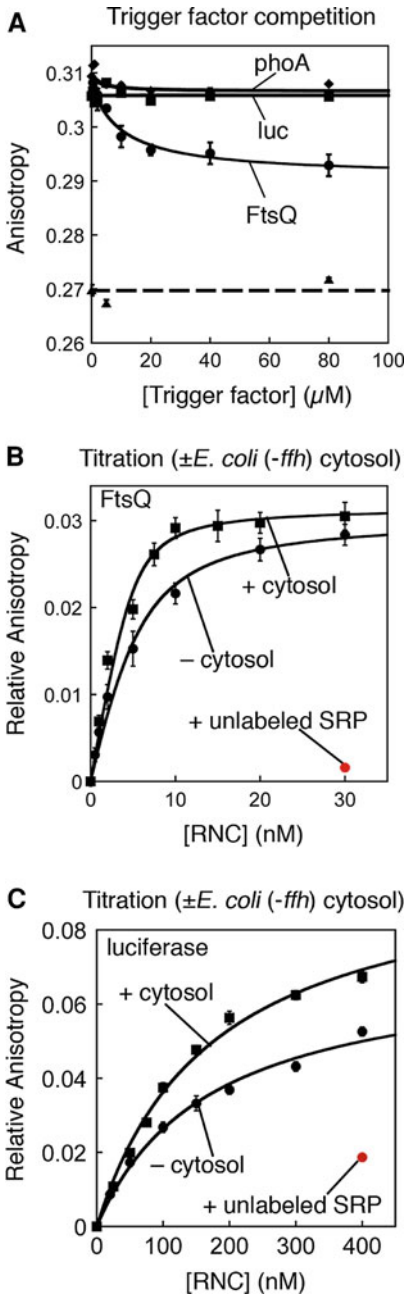

Fig. 5.3 Trigger factor and SRP-free *E. coli* (*-ffh*) total cytosol do not displace the SRP from the RNCs. **a** Fluorescence anisotropy of cargo-loaded SRP in the presence of increasing amounts of trigger factor. RNC_{FtsQ} (*filled circle*), RNC_{phoA} (u) and $RNC_{luciferase}$ (*filled square*) are used as representatives of correct, weak and wrong cargos, respectively. The *dashed line* represents the anisotropy value of free SRP (*filled triangle*). At each concentration, TF has been incubated with the RNC–SRP complex for sufficient time (15–30 min) to ensure that equilibrium has been reached. **b**, **c** Equilibrium titrations to measure the binding affinities of SRP for RNC_{FtsQ} (**b**) and $RNC_{luciferase}$ (**c**) in the presence (*filled square*) and absence (*filled circle*) of SRP- and ribosome-free *E. coli* (*-ffh*) total cytosolic extract. Nonlinear fits of data to Eq. 5.3 gave K_d values of 0.10 ± 0.02 and 0.67 ± 0.11 nM for RNC_{FtsQ} with and without cytosol (**b**), respectively, and 174 ± 14 and 170 ± 10 nM for $RNC_{luciferase}$ with and without *E. coli* cytosol (**c**), respectively. In all titration experiments, fluorescence anisotropy changes can be competed away by unlabeled SRP (*filled circle*). Error bars are SDs from three independent experiments

correct cargos (Fig. 5.4a, d). This and the slower rate at which these *early* complexes rearrange to the *closed* state (see below) suggest that the SRP and SR are likely mispositioned in the *early* targeting complexes formed by the incorrect

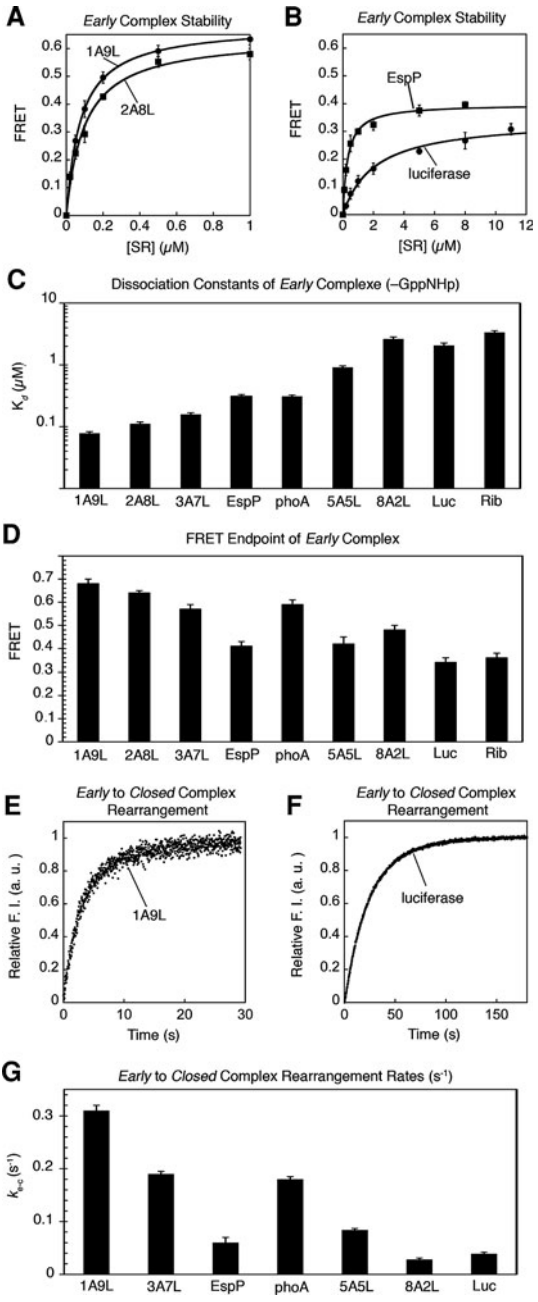

Fig. 5.4 Correct cargos stabilize the *early* intermediate and mediate faster rearrangement to the *closed* complex. **a**, **b** Equilibrium titrations of the *early* intermediate. Nonlinear fits of data gave K_d values of 78, 110, 311 and 2,060 nM and FRET endpoints of 0.68, 0.64, 0.41, and 0.34 for RNC_{1A9L} (**a**, *filled circle*), RNC_{2A8L} (**a**, *filled square*), RNC_{EspP} (**b**, *filled square*), and $RNC_{luciferase}$ (**b**, *filled circle*), respectively. **c**, **d** Summary of the K_d values (**c**) and FRET end points (**d**) of the *early* intermediates formed by different cargos. **e**, **f** Measurements of the *early* → *closed* rearrangement. Nonlinear fits of data gave rate constants of 0.31 s^{-1} with RNC_{1A9L} (**e**) and 0.039 s^{-1} with $RNC_{luciferase}$ (**f**). **g** Summary of the rate constants for the *early* → *closed* rearrangement with different cargos

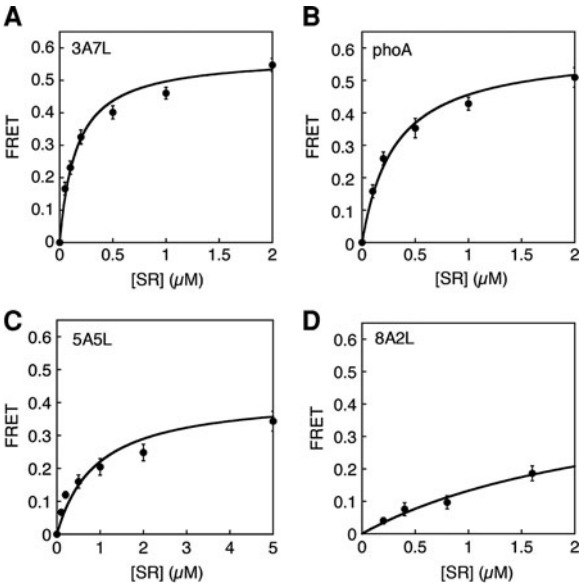

Fig. 5.5 Stabilities of the SRP–SR *early* intermediates formed with different cargos. Equilibrium titrations of the *early* intermediate were carried out as described in Sect. 5.4. Nonlinear fits of data to Eq. 5.4 gave K_d values of the *early* intermediate in the presence of each cargo (Table 5.1). Error bars are SDs from three independent experiments

cargos. Thus weak or incorrect cargos do not induce the formation of a stable and productive *early* complex, and are more likely to exit the pathway prematurely (Fig. 5.1a, arrow b).

To test whether the rearrangement to the *closed* complex is more efficient with the correct than the incorrect cargos (Fig. 5.1a, step 3), we used acrylodan-labeled SRP(C235), which specifically detects formation of the *closed* complex [8]. We preformed the *early* targeting complex in the absence of nucleotides and in the presence of saturating cargo and SR, and monitored its rearrangement into the *closed* complex upon addition of the GTP analogue 5′-guanylylimido-diphosphate (GMPPNP). With RNC_{1A9L}, this rearrangement is fast, occurring at 0.3 s^{-1} (Fig. 5.4e). RNC_{3A7L} and RNC_{phoA} mediated this rearrangement 40% slower (Figs. 5.4g and 5.6). Notably, RNC_{EspP} and cargos weaker than RNC_{5A5L} mediate this rearrangement five to tenfold slower than RNC_{1A9L} (Figs. 5.4f, g, and 5.6). The slower rate of the *early* → *closed* rearrangement observed with these cargos correlated with their lower FRET value in the *early* intermediate (Fig. 5.4d), suggesting that efficient rearrangement to the *closed* complex requires formation of an *early* intermediate in a productive conformation.

The more favorable pre-equilibrium to form the *early* intermediate combined with the faster *early* → *closed* rearrangement would allow the correct cargos to mediate GTP-dependent SRP–SR complex assembly at much faster rates (Fig. 5.1a, steps 2–3). We characterized this cumulative effect using both FRET (Figs. 5.7a–c, and 5.8f, g) and acrylodan-labeled SRP(C235) (Fig. 5.8). Both probes demonstrated that the correct cargos mediate rapid SRP–SR complex assembly with GMPPNP (Figs. 5.7a and 5.8a), and this rate decreases significantly

Table 5.1 Kinetic and thermodynamic parameters for individual reaction step during SRP-dependent protein targeting in the presence of various cargos

	K_d (nM) RNC binding	K_d (nM) early complex	FRET end point early complex	$k_{e\rightarrow c}$ (s^{-1}) early → closed rearrangement	k_{on} (M^{-1} s^{-1}) closed complex	GTPase rate (s^{-1})
1A9L	0.55 ± 0.20	78 ± 5	0.68 ± 0.02	0.31 ± 0.02	$9.9 \pm 1.3 \times 10^6$	0.11 ± 0.01
2A8L	1.2 ± 0.20	110 ± 8	0.64 ± 0.02	ND	$8.8 \pm 1.6 \times 10^6$	0.12 ± 0.02
3A7L	8.4 ± 2.0	158 ± 10	0.57 ± 0.02	0.19 ± 0.01	$2.0 \pm 0.2 \times 10^5$	0.18 ± 0.01
EspP	13.6 ± 3.0	311 ± 21	0.41 ± 0.03	0.060 ± 0.02	$9.2 \pm 0.2 \times 10^3$	0.51 ± 0.08
phoA	108 ± 11	310 ± 20	0.59 ± 0.03	0.18 ± 0.02	$6.3 \pm 0.4 \times 10^4$	0.45 ± 0.02
5A5L	63 ± 4	910 ± 50	0.42 ± 0.02	0.084 ± 0.003	$1.1 \pm 0.2 \times 10^4$	0.38 ± 0.02
8A2L	100 ± 5	≥2630	≥0.48	0.028 ± 0.003	$5.6 \pm 0.3 \times 10^3$	ND
Luciferase	130 ± 12	2060 ± 201	0.34 ± 0.02	0.039 ± 0.003	$1.8 \pm 0.3 \times 10^3$	0.65 ± 0.22

ND not determined; error bars are SDs from three independent experiments

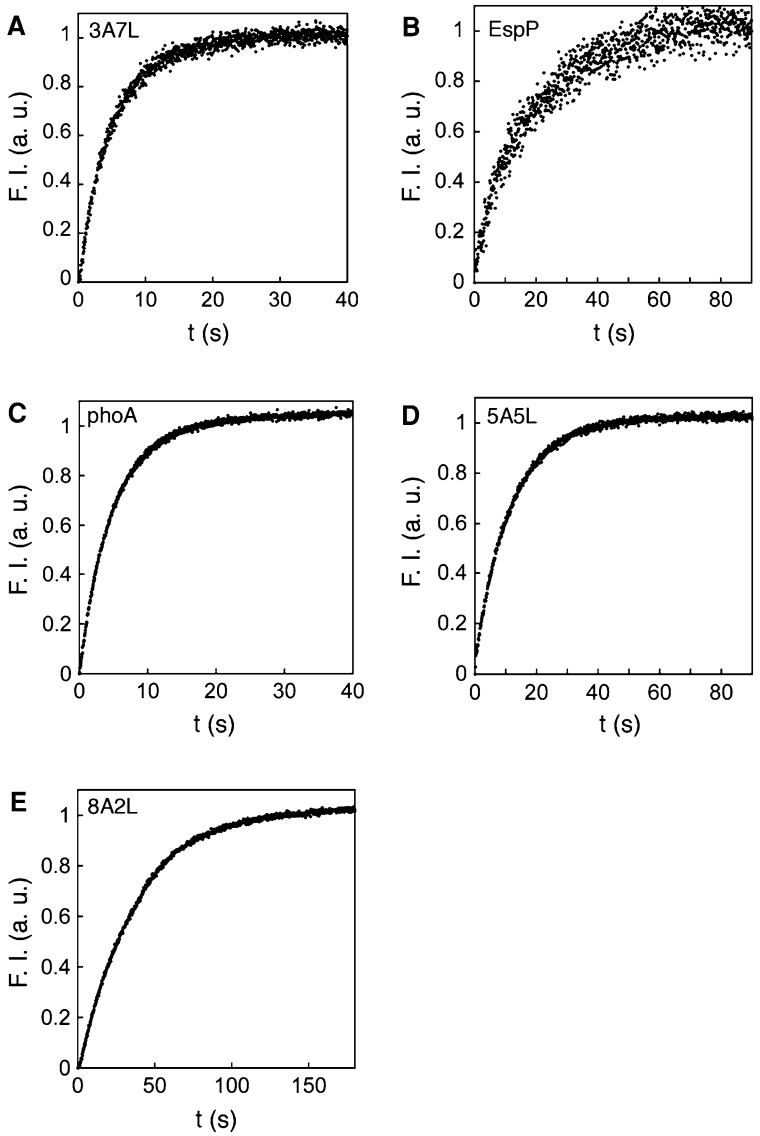

Fig. 5.6 The *early* → *closed* rearrangement is slower with weaker cargos. Rate constants of the GTPase rearrangements were measured using acrylodan-labeled SRP(C235) as described in Sect. 5.4. Rate constants with each cargo (Table 5.1) were derived from nonlinear fits of the data to Eq. 5.5. Reactions were carried out with 100–250 nM SRP, 200 nM RNC_{3A7L} and RNC_{EspP} or 500 nM RNC's with other signal sequences, and 50–75 μM SR

as the signal sequence becomes weaker (Figs. 5.7b, c and 5.8). Both assays revealed a $\sim 10^3$-fold discrimination between the strongest (e.g., RNC_{1A9L}) and weakest (e.g., RNC_{EspP} and RNC_{8A2L}) cargos in the kinetics of GTP-dependent

complex assembly (Figs. 5.7c and 5.8e). This is consistent with the cumulative effect of the over 50-fold more stable *early* intermediate (Fig. 5.4c) and the ~10-fold faster rate at which this intermediate rearranges to the *closed* complex (Fig. 5.4g) with the correct than the incorrect cargos.

To test whether the correct cargos delay GTP hydrolysis more effectively than the incorrect cargos, we determined the rate of the GTPase reaction from the cargo–SRP–SR complexes. RNC_{1A9L} and RNC_{2A8L} reproducibly delay GTP hydrolysis six to eightfold (Figs. 5.7d and 5.9). The next strongest cargo, RNC_{3A7L}, has a smaller but still substantial inhibitory effect on the GTPase reaction (Fig. 5.9). In contrast, incorrect cargos such as RNC_{EspP} inhibit GTP hydrolysis by less than twofold, and $RNC_{luciferase}$ does not significantly affect the GTPase rate (Figs. 5.7e, f, and 5.9). These results are consistent with the hypothesis that the fidelity of protein targeting can be further improved through kinetic proofreading mechanisms by using the energy of GTP hydrolysis (Fig. 5.1a, arrow d).

These results demonstrate that the SRP pathway discriminates against incorrect cargos not only through binding affinity, but also through differences in the kinetics of SRP–SR complex assembly and GTP hydrolysis. Another important determinant of co-translational protein targeting is the length of the nascent polypeptide, as the SRP loses its ability to target substrates when the nascent chain exceeds ~110 residues [31, 32]. Since the bacterial SRP does not arrest translation [1], this gives a ~3 s time window for the SRP to complete protein targeting [29], assuming that SRP begins to recognize cargos when the nascent chain is ~35 amino acids long and a translation elongation rate of ~20–30 amino acids/s in bacteria [33]. Based on this time constraint and the rate and equilibrium constants determined here, we calculated the amount of substrates retained in the SRP pathway after each checkpoint (Fig. 5.10a). The cargo binding step is not sufficient to discriminate against incorrect cargos, allowing over 75% of them to enter the SRP pathway (Fig. 5.10a, light grey). During cargo delivery through GTP-dependent SRP–SR complex assembly, a large portion of substrates weaker than phoA are rejected (Fig. 5.10a, dark grey). Finally, kinetic competition between GTP hydrolysis and cargo unloading allows most of the incorrect substrates to be rejected, whereas the majority of substrates stronger than phoA-3A7L are retained (Fig. 5.10a, black).

To test the validity of this analysis, we determined the targeting efficiency of proteins with various signal sequences using a well-established assay that tests the ability of *E. coli* SRP and SR to mediate the co-translational targeting of preproteins to microsomal membranes [34, 35]. Cleavage of preprolactin (pPL) signal sequence provides readout for successful targeting and translocation (Fig. 5.10b). Bacterial SRP and SR mediate pPL targeting as efficiently as their mammalian homologues despite the heterologous nature of this assay [35]; this highlights the remarkable conservation of the SRP pathway and allows us to test insights from biophysical studies of bacterial SRP and SR in the context of a complete and functional targeting reaction. Importantly, as both reaction substrates and products are quantitated, this assay provides the most accurate measure of targeting

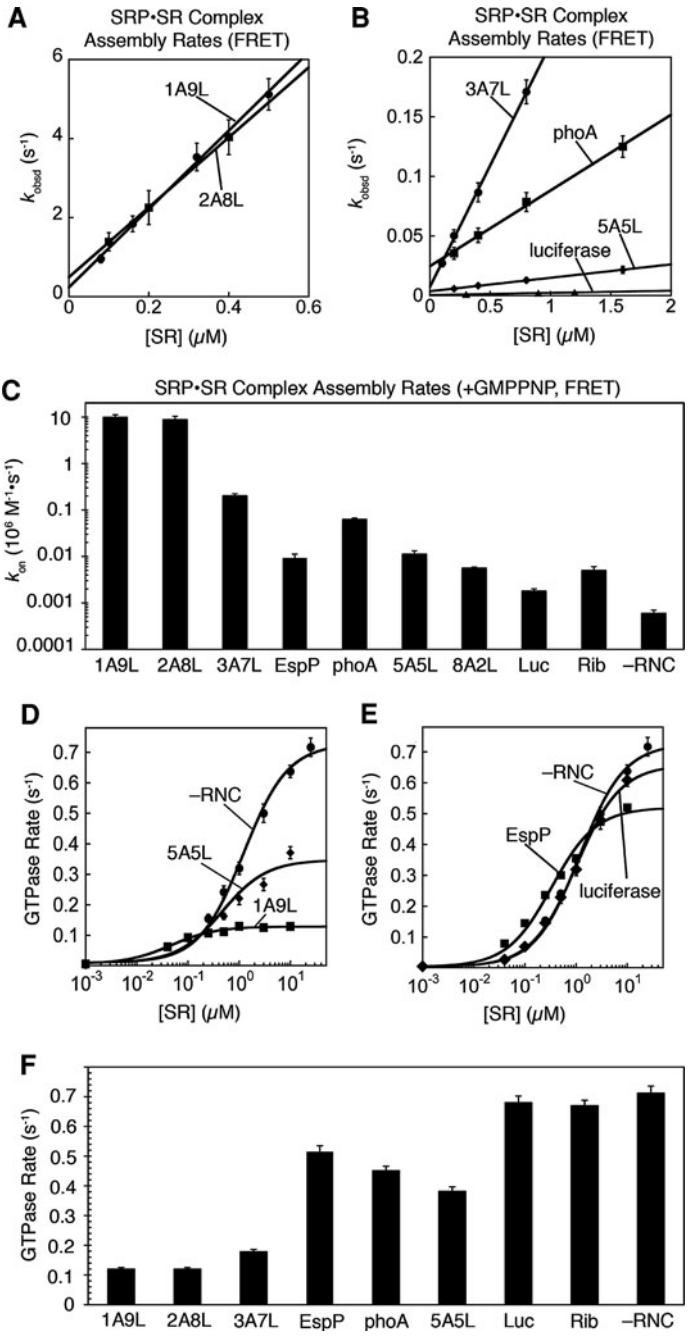
A
SRP•SR Complex Assembly Rates (FRET)
1A9L
2A8L
k_{obsd} (s^{-1})
[SR] (μM)
B
SRP•SR Complex Assembly Rates (FRET)
3A7L
phoA
5A5L
luciferase
k_{obsd} (s^{-1})
[SR] (μM)
C
SRP•SR Complex Assembly Rates (+GMPPNP, FRET)
k_{on} (10^6 M^{-1}•s^{-1})
1A9L 2A8L 3A7L EspP phoA 5A5L 8A2L Luc Rib –RNC
D
–RNC
5A5L
1A9L
GTPase Rate (s^{-1})
[SR] (μM)
E
–RNC
EspP
luciferase
GTPase Rate (s^{-1})
[SR] (μM)
F
GTPase Rate (s^{-1})
1A9L 2A8L 3A7L EspP phoA 5A5L Luc Rib –RNC

◀ **Fig. 5.7** Correct cargos accelerate GTP-dependent complex formation but delay GTP hydrolysis. **a**, **b** Rate constants of SRP–SR complex assembly in GMPPNP measured by FRET. k_{on} values of 9.9×10^6, 8.8×10^6, 2.0×10^5, 2.2×10^4, 1.1×10^4 and 1.8×10^3 M^{-1} s^{-1} for RNC_{1A9L} (**a**, *filled circle*), RNC_{2A8L} (**a**, *filled square*), RNC_{3A7L} (**b**, *filled circle*), RNC_{phoA} (**b**, *filled square*), RNC_{5A5L} (**b**, *filled diamond*) and $RNC_{luciferase}$ (**b**, *filled triangle*), respectively. **c** Summary of GTP-dependent complex assembly rate constants with different cargos. **d**, **e** Effects of cargo on GTP hydrolysis from the SRP–SR complex. k_{cat} are 0.72 s^{-1} without cargo (*filled circle*), and 0.11, 0.34, 0.51, and 0.65 s^{-1} with RNC_{1A9L} (**d**, *filled square*), RNC_{5A5L} (**d**, *filled diamond*), RNC_{EspP} (**e**, *filled square*) and $RNC_{luciferase}$ (**e**, *filled diamond*), respectively. **f** Summary of GTPase rate constants in the presence of different cargos

efficiency. Substrates with signal sequences stronger than 3A7L are efficiently targeted and translocated (Fig. 5.10b and 5.11). In contrast, substrates with the EspP signal sequence or signal sequences weaker than phoA show severe defects in translocation, and almost no translocation was detected for the phoA-8A2L substrate (Fig. 5.10b). Remarkably, the experimentally determined protein targeting efficiencies agree well with predictions based on the kinetic and thermodynamic measurements (Fig. 5.10c), suggesting that our model (Fig. 5.1a) faithfully represents the way SRP handles its substrates.

5.3 Discussion

Our work supports a novel model in which fidelity is achieved during co-translational protein targeting through the cumulative effect of multiple checkpoints, by using a combination of binding, induced fit, and kinetic proofreading mechanisms. With correct substrates, loading of cargo is coupled to its rapid delivery (through accelerated complex assembly) and productive unloading (through delayed GTP hydrolysis); whereas with incorrect cargos stable SRP–SR complex assembly is extremely slow, but once the stable complex is formed rapid GTP hydrolysis immediately drives its disassembly. These differences in downstream steps strongly suggest that incorrect cargos bind the SRP in a less productive mode than the correct cargos [6]. The lack of productive interactions with the signal sequence did not lead to complete rejection of incorrect cargos during the initial binding step, but were detected during subsequent steps and discriminated repeatedly. This conclusion is most strongly supported by the case of EspP, which binds SRP strongly but is rejected primarily by kinetic discrimination in the complex assembly and GTP hydrolysis steps. Our analyses here focused on how the SRP handles each substrate in a single round of targeting. In vivo, a higher fidelity could be achieved during multiple rounds of targeting and with competition between correct and incorrect cargos. In addition, the PCC provides another important checkpoint to discriminate against incorrect cargos such as phoA-8A2L [26, 27]; we could not detect this additional discrimination as the targeting efficiency of this substrate before arrival at PCC is already $\leq 1\%$.

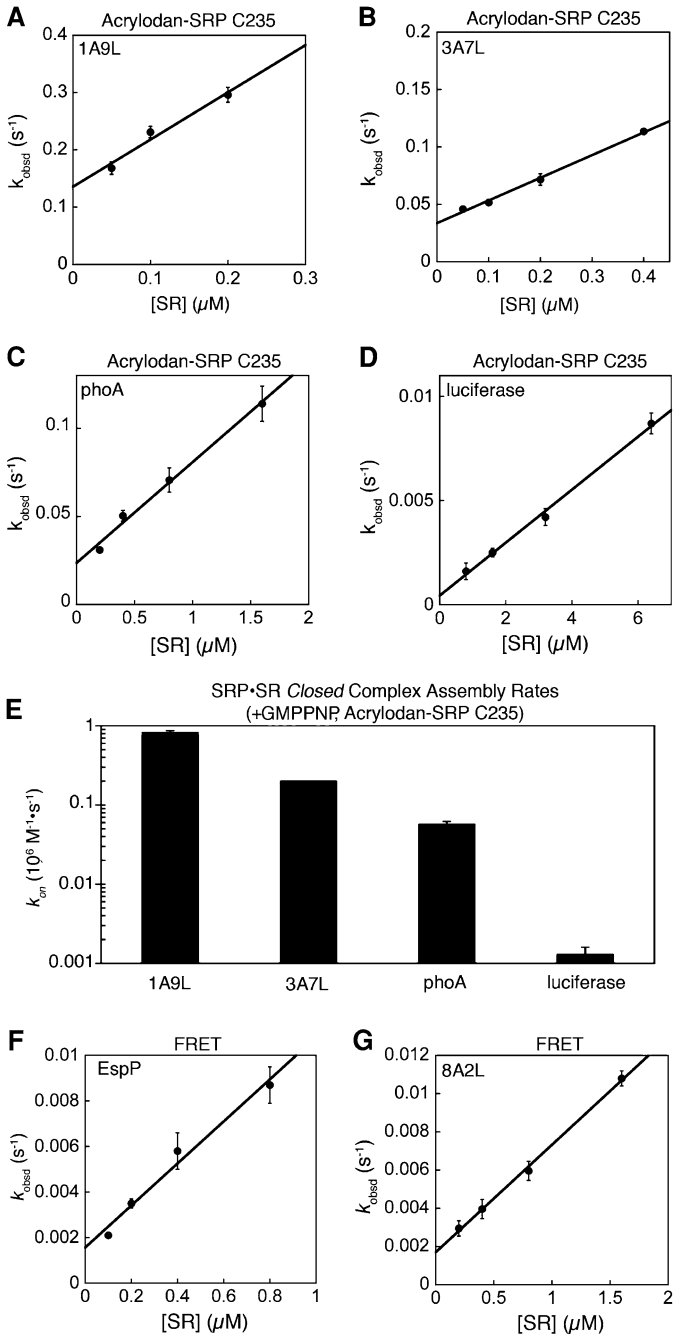
A
Acrylodan-SRP C235
1A9L
k_{obsd} (s^{-1})
[SR] (μM)
B
Acrylodan-SRP C235
3A7L
k_{obsd} (s^{-1})
[SR] (μM)
C
Acrylodan-SRP C235
phoA
k_{obsd} (s^{-1})
[SR] (μM)
D
Acrylodan-SRP C235
luciferase
k_{obsd} (s^{-1})
[SR] (μM)
E
SRP•SR *Closed* Complex Assembly Rates
(+GMPPNP, Acrylodan-SRP C235)
k_{on} (10^6 M^{-1}•s^{-1})
1A9L
3A7L
phoA
luciferase
F
FRET
EspP
k_{obsd} (s^{-1})
[SR] (μM)
G
FRET
8A2L
k_{obsd} (s^{-1})
[SR] (μM)

◀ **Fig. 5.8** Rate constants for assembly of the SRP–SR *closed* complex. **a–d** Complex assembly rate constants were determined using acrylodan-labeled SRP(C235) as described in Sect. 5.4. Linear fits of data to Eq. 5.6 gave second order constants of complex assembly (k_{on}) of 0.82 ± 0.05, 0.20 ± 0.04, 0.057 ± 0.005, and 0.0013 ± 0.0003×10^6 M^{-1} s^{-1} with RNC_{1A9L} (**a**), RNC_{3A7L} (**b**), RNC_{phoA} (**c**), and $RNC_{luciferase}$ (**d**) respectively. **e** Summary of *closed* complex assembly rates with different cargos measured by acrylodan-labeled SRP(C235). **f**, **g** Complex assembly rate constants for RNC_{EspP} and RNC_{8A2L} measured using FRET. Second order constants of complex assembly (k_{on}) were obtained from linear fits of the data to Eq. 5.6 (Table 5.1). Error bars are SDs from three independent experiments

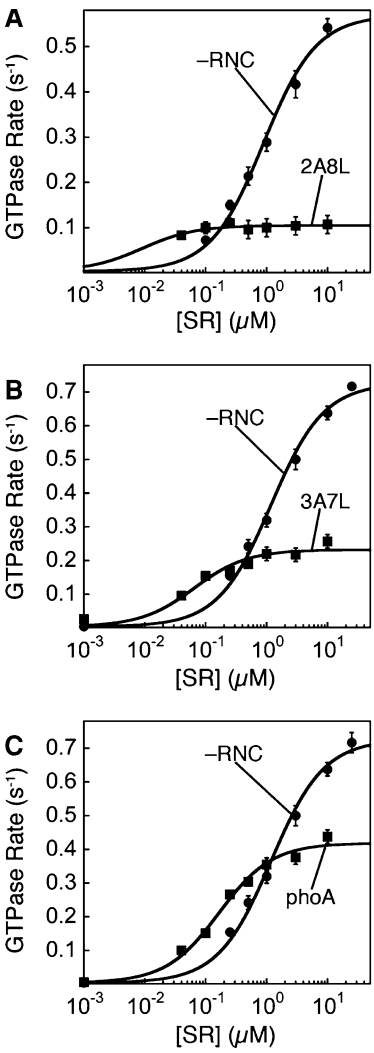

Fig. 5.9 Effects of different cargos on GTPase activation in the SRP–SR complex. GTPase reactions were carried out and analyzed as described in Sect. 5.4. GTPase rate constants (k_{cat}) from the cargo–SRP–SR complexes were obtained from nonlinear fits of data to Eq. 5.7 (Table 5.1). Error bars are SDs from three independent experiments

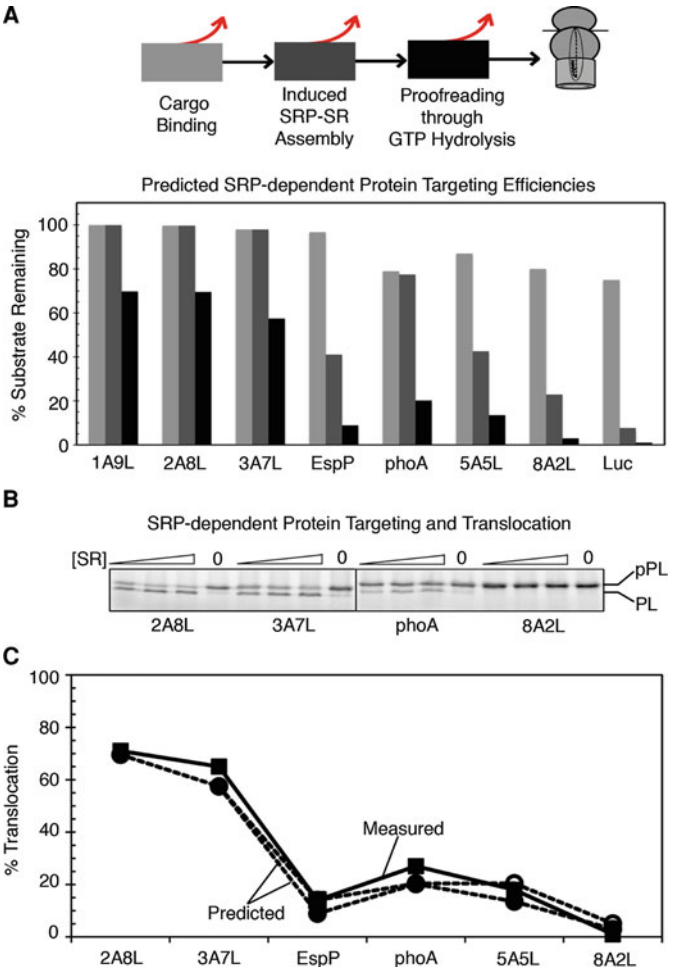

Fig. 5.10 Stepwise rejection of weak or wrong cargos from the SRP pathway. **a** The fraction of cargos remaining in the SRP pathway after each step, calculated as described in Sect. 5.4. As depicted in the top panel, cargos are either retained (*black arrow*) or rejected (*red arrow*) from the pathway during cargo binding (*light grey*), induced SRP–SR assembly (*dark grey*), and proofreading through GTP hydrolysis (*black*). **b** SRP-dependent protein targeting and translocation of substrates with different signal sequences analyzed by SDS-PAGE. pPL and PL denote the precursor and signal sequence-cleaved forms of the substrate, respectively. **c** Predicted protein targeting efficiencies (*filled circle* and *open circle*) agree well with the experimentally determined values (*filled square*), quantitated from the data in **b**. Translation elongation rates of 20 (*filled circle*) and 10 amino acids/s (*open circle*) were used for the *E. coli* and eukaryotic ribosomes, respectively, to calculate the targeting efficiencies. The small discrepancies between the measured and calculated targeting efficiencies based on *E. coli* ribosomes could be rationalized by a slower translation rate of eukaryotic ribosome used in the assay than that of *E. coli* ribosome used in the calculations [111], which gives the SRP and SR a longer time window for complex assembly. This discrepancy became smaller when the calculation was performed using the translation rate of eukaryotic ribosomes (*open circle*)

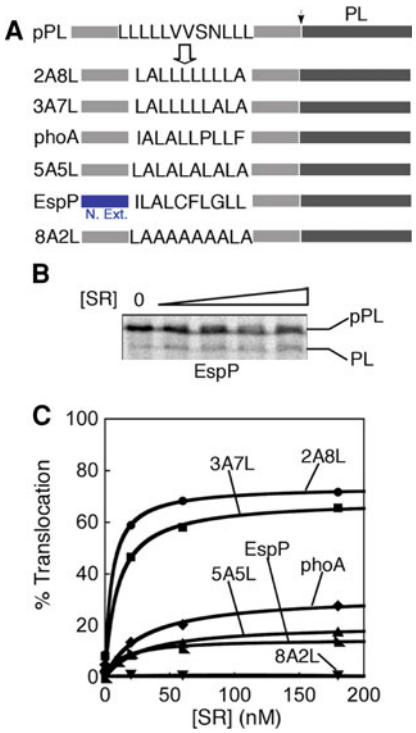

Fig. 5.11 Experimental determination of protein targeting efficiency of substrates bearing the different signal sequences. **a** Schematic diagram depicting the chimericpPL constructs used for the co-translational protein targeting assay (see Sect. 5.4). The arrow between signal sequence (*light grey*) and mature protein (*dark grey*) shows the signal peptidase cleavage site from pPL. *Blue* denotes the N-terminal signal peptide extension of EspP construct. **b** SRP-dependent protein targeting and translocation efficiency of substrates with EspP signal sequences analyzed by SDS-PAGE. pPL and PL denote the precursor and signal sequence-cleaved forms of the substrate protein, respectively. **c** Quantification of the protein targeting and translocation efficiencies of each substrate tested

Our findings are analogous to those observed in tRNA selection during translation, in which a mismatch between the mRNA and tRNA anticodon at the ribosome active site leads not only to weaker binding affinities for the noncognate and near-cognate tRNAs, but also to slower rates of subsequent steps and higher frequency of rejection of the non- and near-cognate tRNAs [36, 37]. Similar strategies of using multiple checkpoints to ensure fidelity have been demonstrated by pioneering work on tRNA synthetases [38] and DNA and RNA polymerases [39, 40], and likely represents a general principle for complex cellular pathways, especially those that need to recognize degenerate signals or to discriminate between substrates based on minor differences.

5.4 Materials and Methods

5.4.1 Materials

The *E. coli* SRP and SR GTPases (Ffh and FtsY, respectively), trigger factor, and 4.5S RNA were expressed and purified as described previously [30, 41]. FtsY(47-497) was used in all the fluorescence measurements, and full length FtsY was used in GTPase rate measurements. The abilities of FtsY(47-497) to interact with SRP and respond to the cargo are similar to those of full length FtsY [8]. Single cysteine mutants of Ffh and FtsY were constructed using the QuickChange mutagenesis procedure (Stratagene), and were expressed and purified using the same procedure as that for the wild-type proteins. Fluorescent dyes *N*-(7-dimethylamino-4-methyl-coumarin-3-yl)maleimide (DACM), fluorescein-5-maleimide (F5M), and BODIPY-FL-*N*-(2-aminoethyl)-maleimide were from Invitrogen.

5.4.2 Signal Sequence Mutants

Plasmids encoding signal sequence variants were constructed based on pUC19StrepFtsQSecM [20], composed of a strep3 tag in the N-terminus, the first 74 amino acids of FtsQ, and a translation stall sequence from SecM (residues 136–166). For this work, FtsQ ([1, 7–9, 14, 21, 30, 34, 35, 42–106] was replaced with the first 50 residues of phoA or firefly luciferase, and mutations were introduced into the hydrophobic core of phoA (Fig. 5.1b in main text) using the QuickChange mutagenesis procedure (Stratagene).

5.4.3 RNC and Ribosome Purification

70S ribosomes were purified from *E. coli* MRE600 cells following established protocols [8, 107]. Homogeneous RNCs were generated from in vitro translation reactions using membrane free cell extract prepared from MRE600 cells, and purified through affinity chromatography and sucrose gradient centrifugation as described previously [8, 107]. RNCs purified using this method can bind SRP, TF, and the secYEG complex [20] and in quantitative assays, exhibit the same affinity for SRP as those measured with RNCs that do not contain an affinity tag [108].

5.4.4 SRP- and Ribosome-Free E. coli (-ffh) Total Cytoplasmic Extract

The bacterial strain HDB51 MC4100 *ara* + *secB* + *zic-4901*::Tn*10* *ffh*::*kan-1* *λ*(Para-*ffh* Apr), in which the expression of Ffh is under the control of arabinose

promoter, was a generous gift from Harris D. Bernstein at NIDDK, NIH [109]. Bacterial culture was grown at 37 °C in the absence of arabinose for 4–5 generations so that more than 90% of endogenous Ffh was depleted [109]. Cells were harvested at $OD_{600} = 0.70$. The cell pellet was washed with 0.1 M Tris–HCl buffer (pH 8.0), and resuspended in lysis buffer [0.1 M Tris–HCl, 20% sucrose, 1 mM phenylmethylsulphonyl fluoride (PMSF), and 50 μg/mL lysozyme] for 90 min at room temperature. $MgCl_2$ was then added to stabilize the spheroplasts at a final concentration of 20 mM. The mix was spun at 8,000 rpm for 10 min to separate spheroplasts from the periplasmic fraction. The spheroplasts were washed twice in buffer containing 0.1 M Tris–HCl (pH 8.0), 20% sucrose, and 20 mM $MgCl_2$, resuspended in PBS containing 1 mM PMSF, and passed through French Press three times at 10,000 psi. The lysate was clarified by centrifugation at 8,000 rpm for 10 min, and ultracentrifuged twice at 320,000 g for 3 h at 4 °C to remove membranes and ribosomes. The supernatant was collected as the cytosolic extract.

5.4.5 Fluorescence Labeling

For FRET measurements, DACM and BODIPY-FL were used to label single-cysteine mutants of Ffh and FtsY, respectively, as described previously [7]. For measurements using environmental sensitive probes, acrylodan was used to label Ffh(C235) as described [8]. For fluorescence anisotropy measurements, F5M was used to label Ffh(C421). Fluorescence labeling with F5M followed the same procedure as those for DACM and BODIPY-FL. Labeled protein was purified as described [7], and the concentration of labeled protein was determined using an absorption extinction coefficient of $\varepsilon_{504} = 83{,}000\ M^{-1}\ cm^{-1}$ for F5M. The efficiency of labeling was typically ≥95% with a background of <5%.

5.4.6 Fluorescence Anisotropy Measurements

Anisotropy measurements used an excitation wavelength of 450 nm and emission wavelength of 518 nm. Fluorescence anisotropy was calculated according to Eq. 5.1:

$$R = \frac{(I_{VV} - G \times I_{VH})}{(I_{VV} + 2G \times I_{VH})} \tag{5.1}$$

in which I_{VV} and I_{VH} are the vertically and horizontally polarized emission intensities when the sample is vertically excited, G is the grating factor that corrects for the wavelength response to polarization of the emission optics and detectors, defined as $G = I_{HV}/I_{HH}$, where I_{HV} and I_{HH} are the vertically and horizontally polarized emission intensities when the sample is horizontally excited.

5.4.7 Fluorescence Measurements

All measurements were carried out at 25 °C in assay buffer [50 mM KHEPES, pH 7.5, 150 mM KOAc, 10 mM $Mg(OAc)_2$, 2 mM DTT] on a Fluorolog-3-22 spectrofluorometer (Jobin–Yvon, Edison, NJ). The detergent Nikkol, which was used in previous work, was not used for studies of complex assembly in this work. The stimulatory effects of strong SRP cargos can be observed without removing Nikkol [7], and the same SRP–SR complex assembly rate constants and stability of the *early* complex was observed with the strong cargos (RNC_{1A9L}, RNC_{2A8L}, and RNC_{3A7L}) with or without Nikkol present. On the other hand, Nikkol obscures the small stimulatory effects from weak cargos or the empty ribosome, as the complex assembly rate constant between free SRP and SR is ~100-fold faster in the presence of Nikkol [22].

FRET measurements were carried out using an excitation wavelength of 380 nm and an emission wavelength of 470 nm. FRET efficiency was calculated as described [7]. For measurements using acrylodan-labeled SRP(C235), an excitation wavelength of 380 nm was used and fluorescence emission at 500 nm was monitored [8].

5.4.8 Strategy to Isolate Individual Reaction Steps During Protein Targeting

This section describes how the individual reaction rate or equilibrium constants were isolated using the principles of rate laws, rate-limiting steps, the rules of thermodynamics and mass action, and the information acquired for a previous reaction step. In general, each time a subsequent reaction step was measured, reaction conditions were designed such that all the cargos have passed the previous steps.

5.4.8.1 Cargo Binding to the SRP (Fig. 5.1a, Step 1)

The equilibrium binding affinity of SRP for various cargos was determined by equilibrium titration using the change in the fluorescence anisotropy of F5M-labeled SRP(C421). In general, 5–20 nM SRP and 100 μM GMPPNP were used in the titrations. We found that cargos bind to and dissociate from the SRP on a time scale faster than manual mixing (30 s to 1 min). Therefore, all samples were incubated for 2–5 min to ensure that equilibrium has been established. In each measurement, increasing amounts of cargo were added to a fixed amount of fluorescently labeled SRP. The anisotropy value (A) at different SRP concentrations were plotted as a function of cargo concentration ([RNC]). The data were fit to single binding (Eq. 5.2) or quadratic (Eq. 5.3) equations,

$$A = A_0 + (A_1 - A_0) \times \frac{[\mathrm{RNC}]}{K_d + [\mathrm{RNC}]} \tag{5.2}$$

$$A = A_0 + (A_1 - A_0)\left\{\frac{c_0 + [\mathrm{RNC}] + K_d - \sqrt{(c_0 + [\mathrm{RNC}] + K_d)^2 - 4c_0[\mathrm{RNC}]}}{2c_0}\right\} \tag{5.3}$$

in which A_0 is the anisotropy value of free SRP, A_1 is the anisotropy value when SRP is bound to cargo, c_0 is the concentration of total SRP, and K_d is the equilibrium dissociation constant of SRP for the RNC. No significant changes were found in fluorescence intensity of free- and bound-SRP after photo-bleaching effect was corrected.

5.4.8.2 Formation of the SRP–SR Early Intermediate (Fig. 5.1a, Step 2)

During the measurement of this and all subsequent steps, all reactions were carried out in the presence of saturating cargo concentrations (100 nM RNC_{1A9L} and RNC_{2A8L}, 200 nM RNC_{3A7L} and RNC_{EspP}, 500 nM RNC_{phoA}, RNC_{5A5L} and RNC_{8A2L}, 600 nM $RNC_{luciferase}$, and 1 μM ribosome). This ensures that 80–99% of the SRP are bound to the cargos so that the differences in cargo binding affinities contribute less than 20% to our measurements.

Our previous work showed that the rate constant of *early* complex formation is rapid and affected only twofold by a strong cargo, and that the primary effect of cargo is on the stability of the *early* complex. We therefore measured the equilibrium stability of the *early* complex formed by different cargos using the FRET assay. Equilibrium titrations were carried out in the presence of a small, fixed amount of RNC-bound, donor-labeled SRP and increasing amounts of acceptor-labeled SR in the absence of GTP or GTP analogues. Equilibrium was established upon manual mixing. FRET efficiency was calculated as described and plotted as a function of SR concentration ([SR]). The data were fit to Eq. 5.4,

$$E = E_1 \times \frac{[\mathrm{SR}]}{K_d + [\mathrm{SR}]} \tag{5.4}$$

in which E_1 is the FRET value (end point) when all the cargo–SRP complexes are bound to SR, and K_d is the equilibrium dissociation constant of the *early* intermediate.

*The early → closed rearrangement (*Fig. 5.1a, step 3*).* This rearrangement was measured using acrylodan-labeled SRP(C235), which specifically detects the *closed* complex [8]. The *early* cargo–SRP–SR complexes were pre-assembled in the presence of 0.1–0.25 μM acrylodan-labeled SRP(C235), saturating cargo and SR with respect to their K_d values, and in the absence of nucleotides. An excess of GMPPNP (400 μM) was added to initiate the rearrangement to the *closed* complex

and the fluorescence intensity of acrylodan (I) was monitored over time. The time courses were single exponential and fit to Eq. 5.5,

$$I(t) = I_1 + (I_0 - I_1) \times \exp(-k_{obsd}t) \tag{5.5}$$

in which I_0 is the fluorescence before addition of GMPPNP, I_1 is the fluorescence value at $t \rightarrow \infty$, and k_{obsd} is the observed rate constant. In all cases, we ensured that SR concentrations were sufficiently high such that the values of k_{obsd} were independent of SR concentration, confirming that the unimolecular rearrangement within the GTPase complex was isolated. With free SRP, this method gives the same rate constant for this rearrangement (1.5 s^{-1}) as that previously measured during a continuous FRET assay in which the *early* complex was not first stalled by leaving out GTP (1–2 s^{-1}) [7]. Further, when acrylodan-labeled SRP(C235) was used to monitor SRP–SR complex assembly with RNC_{1A9L}, at high SR concentrations the observed assembly rate constant deviated from linearity and plateaued, indicating that the reaction was rate limited by the early to closed rearrangement at saturating SR concentrations. The rate of the rearrangement obtained from this plateau was 0.34 s^{-1} (Fig. 5.12), comparable to that of 0.31 s^{-1} measured using the pulse-chase experiment (Fig. 5.4e, g). Together, the remarkable agreement between the different methods indicates that: (i) the *early* intermediate isolated in the absence of nucleotides is kinetically competent for subsequent rearrangements; and (ii) our approach of isolating the *early* intermediate and chasing it to the *closed* complex provides a valid method to measure the rate of this conformational rearrangement.

*Rate constants for GTP-dependent SRP–SR complex assembly (*Fig. 5.1a, steps 2 + 3*).* The second-order rate constant for SRP–SR association to form the GTP-stabilized *closed* complex was measured using acrylodan-labeled SRP(C235). A constant concentration of cargo-bound, labeled SRP was mixed with varying concentrations of SR to initiate complex assembly, and the changes in the fluorescence of acrylodan-labeled SRP(C235) was monitored over time. The data were fit to Eq. 5.5 above to obtain the observed rate constants (k_{obsd}) at individual SR concentrations. The values of k_{obsd} were plotted as a function of SR concentrations of SR ([SR]) and fit to Eq. 5.6,

$$k_{obsd} = k_{on}[SR] + k_{off} \tag{5.6}$$

in which k_{on} and k_{off} are the rate constants for complex assembly and disassembly, respectively. Fast reactions were measured on a Kintek stopped-flow apparatus. As an independent way to measure the second order rate constant for stable SRP–SR complex assembly, FRET instead of the environmentally sensitive probes was used and the rate constants were determined analogously. The conditions for measuring complex assembly rate constants are: 100 μM GMPPNP; 80 nM SRP and 100 nM RNC_{1A9L} or RNC_{2A8L}; 100 nM SRP and 200 nM RNC_{3A7L} or RNC_{EspP}; 200 nM SRP and 500 nM RNC_{phoA}, RNC_{5A5L} or RNC_{8A2L}, 300 nM SRP and 600 nM $RNC_{luciferase}$.

These two methods provide independent and complementary information about the rate constants of complex assembly. Acrylodan-labeled SRP(C235)

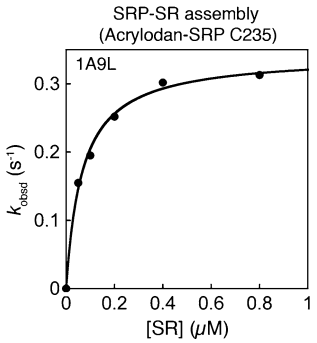

Fig. 5.12 Acrylodan-labeled SRP C235 monitors two-step assembly of the SRP–SR closed complex. Observed complex assembly rate constants were determined using acrylodan-labeled SRP(C235) as described in Sect. 5.4. The deviation from linearity of the observed rates indicate that assembly of the closed complex is a two-step process, with a unimolecular rearrangement rate-limiting at saturating SR concentrations. Nonlinear fits of data to Eq. 5.7 gave the rearrangement rate from the early to the closed complex as 0.34 s^{-1} with RNC_{1A9L}

allows us to specifically measure the assembly rate of the *closed* complex. FRET, on the other hand, reports on the formation of a stable targeting complex that includes both the *early* and *closed* conformational states. For most of the cargos, these two methods yield the same rate constants within experimental error (cf. Fig. 5.7c vs Fig. 5.8e). For RNC_{1A9L} and RNC_{2A8L}, the rate constants measured by FRET is ~10-fold faster than by acrylodan-labeled SRP(C235). This is because with these two cargos, the *early* intermediate is similar in stability to the *closed* complex; hence the SRP–SR complex formed by these cargos in GMPPNP is a roughly equal mixture of the *early* and *closed* states, both of which are detected by FRET but only the latter was detected by acrylodan-labeled SRP(C235). Because stable complex formation bypasses the *early* → *closed* rearrangement with these two cargos, their rate constant for GTP-dependent complex assembly detected by FRET is faster than that detected by acrylodan-labeled SRP(C235). In contrast, for cargos weaker than RNC_{3A7L}, the *closed* complex is the predominant conformation and its formation was monitored by both probes. Because complex assembly is rapid and not rate-limiting for the GTPase cycles and for protein targeting with RNC_{1A9L} and RNC_{2A8L}, roughly the same results (with differences of <2%) were obtained in numerical analysis of their protein targeting efficiencies regardless of whether the complex assembly rate constants measured by the FRET or acrylodan probes were used for the calculation.

*GTP hydrolysis from the SRP–SR complex (*Fig. 5.1a, step 4*).* The GTPase assay to measure the stimulated GTP hydrolysis reaction between SRP and FtsY was carried out and analyzed as described [30]. 40–50 nM SRP were loaded with cargo in the presence of increasing SR concentrations, and the reactions were initiated by addition of 100 μM GTP doped with γ-^{32}P-GTP. The SR concentration dependence of the observed GTPase rate constant (k_{obsd}) was fit to Eq. 5.7,

$$k_{\text{obsd}} = k_{\text{cat}} \times \frac{[\text{SR}]}{[\text{SR}] + K_m} \tag{5.7}$$

in which k_{cat} is the rate constant at saturating SR concentration, and K_m is the SR concentration required to reach half saturation. It should be noted that in this assay, the observed rate constants at subsaturating SR concentrations represents the second order reaction: $^{\text{GTP}}\text{SRP} + \text{SR}^{\text{GTP}} \rightarrow 2\text{GDP} + 2\text{P}_\text{i}$, and is rate-limited by complex assembly between the SRP and SR. The rate constant observed at saturating SR concentrations (k_{cat}) represents the GTPase rate constant from a fully formed, stable cargo–SRP–SR complex, and is the parameter relevant in this study. Nikkol was included in the GTPase assay as the rate of GTP hydrolysis from the SRP–FtsY complex was not affected by Nikkol [22], and inclusion of Nikkol allows saturation to be achieved at much lower FtsY concentrations.

5.4.9 Co-translational Protein Targeting and Translocation

A previously established heterologous protein targeting assay [34, 35], based on the ability of *E. coli* SRP and FtsY to mediate the targeting of preprolactin (pPL) to microsomal membranes, was used in this study. Bacterial SRP and SR mediate pPL targeting as efficiently as their mammalian homologues despite the heterologous nature of this assay [35]; this highlights the remarkable conservation of the SRP pathway and allows us to test insights from biophysical studies of bacterial SRP and SR in the context of a complete and functional targeting reaction. Importantly, as both substrates and products are quantitated, this assay provides the most accurate measure of targeting efficiency. Therefore, it is by far the most suitable assay for the purpose of this study.

ER microsomal membranes have been washed with EDTA, high salt, and digested with trypsin to remove the endogenous SRP and SR, as described previously [35]. 200 nM SRP and four equiv. of washed and trypsin-digested microsomal membrane were used in the targeting reaction. *E. coli* SRP binds to *E. coli* ribosomes with similar affinity ($K_d = 80$ nM) as those measured previously for the binding of SRP to wheat germ ribosomes ($K_d = 71$ nM) [31]. Further, *E. coli* SRP and FtsY can mediate the targeting and translocation of preproteins as efficiently as mammalian SRP and SR despite the heterologous nature of this assay [35]. This strongly suggests that the SRP–ribosome interactions are highly conserved across species and that the heterologous targeting assay provides a reasonable system to test insights from our biophysical measurements in the bacterial system in the context of a complete and functional targeting reaction. Constructs for the protein translocation assay were based on the plasmid pSPBP4. The hydrophobic core of the pPL signal sequence was replaced with the model signal sequences (Fig. 5.11) using the QuickChange mutagenesis procedure (Stratagene).

5.4.10 Numerical Analysis of Protein Targeting Efficiency

This analysis estimates the fraction of each cargo that can be successfully targeted by the SRP pathway within a limited time window, t_w, before the nascent chain exceeds ~110 residues [32]. This time window was based on the consideration that the SRP loses its ability to target substrates when the nascent chain exceeds ~110 residues [31, 32]. Since the bacterial SRP does not arrest translation [1], this gives a t_w of ~3 s (or 6 s when eukaryotic ribosome was used) for the SRP to complete protein targeting [29], assuming that SRP begins to recognize cargos when the nascent chain is ~35 amino acids long and a translation elongation rate of ~20–30 amino acids/s in bacteria (or 10–15 amino acids/s for eukaryotic ribosome) [33].

During the first step, the fraction of cargos that bind to SRP is calculated from: $P(1) = [SRP]/(K_d + [SRP])$, using a cellular SRP concentration of 400 nM [24] and the K_d values from Fig. 5.1. During the second step, the fraction of cargos that are delivered to the membrane after stable SRP–SR complex assembly is calculated from: $P[2] = P[1] \times \exp(-k_{on}[SR] \times t_w)$, using a SR concentration of 2 μM (as was the condition used in the protein targeting reactions in Figs. 5.10b and 5.11), the k_{on} values determined in Fig. 5.7c, and a time window (t_w) of 3- or 6-s for *E. coli* and eukaryotic ribosomes, respectively. During the last step, the fraction of cargos that can be unloaded to the protein conducting channel (PCC) before GTP hydrolysis is calculated from: $P[3] = P[2] \times [1 - \exp(-k_{GTPase} \times t_{PCC})]$, using the GTP hydrolysis rate constants (k_{GTPase}) determined in Fig. 5.7f. t_{PCC} denotes the lifetime for cargo unloading and was estimated to be ~3 s, as in the presence of the correct cargos the late conformational changes in the SRP–SR GTPase complex that are important for driving cargo unloading become rate limiting [8] and likely takes the majority of the 3 s time window for protein targeting.

5.5 Supplementary Text

5.5.1 A Sequential Model for Rejection of Incorrect Cargos by Additional Checkpoints in the SRP Pathway Following the Cargo-Binding Step

In this chapter, we postulated and tested the model that after the cargos are loaded on the SRP, the incorrect cargos could be less efficient during subsequent steps of targeting; these steps thereby provide additional checkpoints to help reject incorrect cargos [21]. We considered the following potential checkpoints: (1) Formation of the *early* SRP–SR complex (Fig. 5.1a, step 2), an obligatory intermediate preceding the formation of subsequent complexes [7, 8]. This intermediate is highly unstable with free SRP, and >98% of it dissociates before rearranging into the subsequent complex. A strong cargo could stabilize the *early* intermediate

and prevent its premature disassembly [8]. If incorrect cargos could not provide such a stabilization, then their *early* targeting complexes would be more likely to disassemble and exit the SRP pathway prematurely (Fig. 5.1a, arrow b). (2) Rearrangement of the *early* intermediate to the *closed* complex (Fig. 5.1a, step 3), which is essential for switching the SRP from a cargo-binding to a cargo-releasing mode and primes the cargo for unloading [8]. If incorrect cargos were less efficient in this rearrangement, then their late stages of targeting would be delayed (Fig. 5.1a, arrow c). (3) GTP hydrolysis from the SRP–SR complex, which occurs rapidly in the absence of cargo [30]. A strong cargo could delay GTP hydrolysis, providing the cargo–SRP–SR complex an important time window to search for the target membrane and the PCC before GTP hydrolysis drives the irreversible disassembly of the targeting complex (Fig. 5.1a, steps 4 vs. 5) [8]. If incorrect cargos could not delay GTP hydrolysis as effectively, they would be more likely to be rejected through premature GTP hydrolysis (Fig. 5.1a, arrow d). This would further improve the fidelity of targeting via kinetic proofreading. Beside SRP, the protein translocation machinery also discriminates against incorrect cargos [26, 27]. However, the translocation machinery mediates translocation of proteins from both the SRP- and SecB-pathways, including EspP [28]. Thus it is unlikely to be solely responsible for the stringent substrate selection by the SRP.

5.5.2 *E. coli* Cytosolic Factors Do Not Compete With SRP for Binding the RNC

It has been suggested that cellular chaperones that interact with translating ribosomes, such as trigger factor (TF), can compete with SRP for binding to the RNCs and thus increase the specificity of SRP–cargo binding [23, 110]. However, the presence of up to 80 μM TF did not compete away the binding of SRP to either the correct (RNC_{ftsQ}), borderline (RNC_{phoA}), or incorrect ($RNC_{luciferase}$) cargos (Fig. 5.3a), consistent with previous findings [25]. Even in the presence of SRP- and ribosome-free *E. coli* total cytosolic extract (see Sect. 5.4), SRP–RNC binding affinities were not significantly affected (Fig. 5.3b, c). These results strongly suggest that cytosolic factors do not compete with SRP to increase the specificity of SRP–cargo binding.

5.5.3 Additional Considerations of Substrate Selection by the SRP In Vivo

The analyses in this work considered how the SRP handles each substrate protein during a single round of protein targeting. In vivo, a higher fidelity could be achieved by the SRP because of several factors. First, correct cargos are delivered more rapidly than the incorrect cargos; this would allow a larger

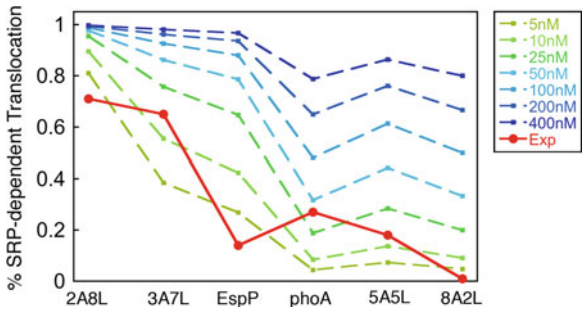

Fig. 5.13 Models based solely on discrimination in cargo-binding affinities would not reproduce the experimentally observed pattern of substrate selection by the SRP pathway. Numerical analysis for protein targeting and translocation efficiencies was carried out as described in Sect. 5.4 assuming a one-step mechanism of substrate selection based on the binding affinities of SRP to different cargo substrates. Different effective concentrations of free SRP ranging from 5 to 400 nM (specified in the *top right panel*) were used. The *red line* depicts the experimentally determined protein targeting and translocation efficiencies (from Fig. 5.10c in main text) and was shown for comparison

number of the correct than incorrect cargos to be targeted within a given time window during multiple rounds of protein targeting. Second, the SRP–SR interaction kinetics could be slower in vivo than in vitro, as protein diffusion rates tend to be slower within the crowded cellular environment. This would render the SRP–SR complex assembly step more rate-limiting for the targeting reaction in vivo and thus increase the contribution of this step to rejection of borderline substrates such as phoA. On the other hand, the membrane association of the SRP receptor FtsY could also affect the kinetics of SRP–SR interactions and the cargo unloading steps, rendering these downstream step(s) more or less rate-limiting. However, FtsY's localization could not affect the interaction of free SRP with the RNC, and thus would not change the conclusion that differences in SRP–cargo binding affinities do not provide sufficient discrimination against the incorrect cargos. Finally, competition between the strong and weak cargos may lower the effective concentration of free SRP in vivo; this would allow some of the discrimination in SRP's cargo binding affinities to be realized. Nevertheless, regardless of the effective SRP concentration in vivo, mechanisms based solely on discrimination in SRP–cargo binding affinities would not be able to reproduce the experimentally observed pattern of substrate selection (Fig. 5.13). Under all conditions, such a mechanism predicts that EspP would be targeted with similar efficiency as phoA-3A7L, and that phoA, phoA-5A5L and phoA-8A2L would be targeted with the same efficiencies (Fig. 5.13, dashed lines); these predictions are not supported by experimental data (Fig. 5.13, red). Thus subsequent steps following cargo binding would be essential for the SRP to select the correct set of substrate proteins even in the presence of competition between correct and incorrect cargos. In addition, the secY translocation machinery provides another important checkpoint to discriminate against

incorrect cargos such as phoA-8A2L [26, 27]; we could not detect this additional discrimination as the targeting efficiency of this substrate before arrival at the translocation machinery is already $\leq 1\%$.

Acknowledgments We thank C. Schaffitzel and N. Ban for help with the purification of RNCs and trigger factor, J. Luirink for plasmids encoding the phoA signal sequence variants, L. Randall for the plasmid encoding luciferase, B. Bukau and E. Deurling for the plasmid encoding trigger factor, H. D. Bernstein for the strain HDB51, and R. J. Deshaies, A. Varshavsky, W. Zhong, N. Pierce, and the Shan laboratory for comments on the manuscript. This work was supported by NIH grant GM078024, career awards from the Burroughs Welcome Foundation, the Henry and Camille Dreyfus foundation, the Beckman foundation, and the Packard foundation to S. S.

References

1. Walter P, Johnson AE (1994) Annu Rev Cell Biol 10:87
2. Rapoport TA (2007) Nature 450:663
3. Schaffitzel C et al (2006) Nature 444:503
4. Halic M et al (2006) Science 312:745
5. Halic M et al (2006) Nature 444:507
6. Pool MR, Stumm J, Fulga TA, Sinning I, Dobberstein B (2002) Science 297:1345
7. Zhang X, Kung S, Shan SO (2008) J Mol Biol 381:581
8. Zhang X, Schaffitzel C, Ban N, Shan SO (2009) Proc Natl Acad Sci U S A 106:1754
9. Connolly T, Gilmore R (1989) Cell 57:599
10. Kaiser CA, Preuss D, Grisafi P, Botstein D (1987) Science 235:312
11. Gierasch LM (1989) Biochem 28:923
12. Hegde RS, Bernstein HD (2006) Trends Biochem Sci 31:563
13. von Heijne G (1985) J Mol Biol 184:99
14. Keenan RJ, Freymann DM, Walter P, Stroud RM (1998) Cell 94:181
15. Bernstein HD et al (1989) Nature 340:482
16. Huber D et al (2005) J Bacteriol 187:2983
17. Valent QA et al (1995) EMBO J 14:5494
18. Doud SK, Chou MM, Kendall DA (1993) Biochem 32:1251
19. Peterson JH, Szabady RL, Bernstein HD (2006) J Biol Chem 281:9038
20. Schaffitzel C, Ban N (2007) J Struct Biol 158:463
21. Zheng N, Gierasch LM (1997) Mol Cell 1:79
22. Bradshaw N, Neher SB, Booth DS, Walter P (2009) Science 323:127
23. Gu SQ, Peske F, Wieden HJ, Rodnina MV, Wintermeyer W (2003) RNA Publ RNA Soc 9:566
24. Jensen CG, Pedersen S (1994) J Bacteriol 176:7148
25. Buskiewicz I et al (2004) Proc Natl Acad Sci U S A 101:7902
26. Jungnickel B, Rapoport TA (1995) Cell 82:261
27. Hegde RS, Kang SW (2008) J Cell Biol 182:225
28. Valent QA et al (1998) EMBO J 17:2504
29. Zheng N, Gierasch LM (1996) Cell 86:849
30. Peluso P, Shan SO, Nock S, Herschlag D, Walter P (2001) Biochem 40:15224
31. Flanagan JJ et al (2003) J Biol Chem 278:18628
32. Siegel V, Walter P (1988) EMBO J 7:1769
33. Dennis PP, Nomura M (1974) Proc Natl Acad Sci U S A 71:3819
34. Shan SO, Chandrasekar S, Walter P (2007) J Cell Biol 178:611
35. Powers T, Walter P (1997) EMBO J 16:4880

36. Rodnina MV, Wintermeyer W (2001) Trends Biochem Sci 26:124
37. Cochella L, Green R (2005) Curr Biol 15:R536
38. Fersht AR, Kaethner MM (1976) Biochem 15:3342
39. Kunkel TA, Bebenek K (2000) Annu Rev Biochem 69:497
40. Uptain SM, Kane CM, Chamberlin MJ (1997) Annu Rev Biochem 66:117
41. Kramer G et al (2004) J Bacteriol 186:3777
42. Alberts B (1998) Cell 92:291
43. Shan SO, Schmid SL, Zhang X (2009) Biochem 48:6696
44. Matlack KES, Mothes W, Rapoport TA (1998) Cell 92:381
45. Johnson AE, van Waes MA (1999) Annu Rev Cell Dev Biol 15:799
46. Shan SO, Walter P (2005) FEBS Lett 579:921
47. Shan SO, Stroud RM, Walter P (2004) PLoS Biol 2:1572
48. Walter P, Ibrahimi I, Blobel G (1981) J Cell Biol 91:545
49. Walter P, Blobel G (1981) J Cell Biol 91:551
50. Walter P, Blobel G (1981) J Cell Biol 91:557
51. Batey RT, Rambo RP, Lucast L, Rha B, Doudna JA (2000) Science 287:1232
52. Krieg UC, Walter P, Johnson AE (1986) Proc Natl Acad Sci U S A 83:8604
53. Kurzchalia TV et al (1986) Nature 320:634
54. Zopf D, Bernstein HD, Johnson AE, Walter P (1990) EMBO J 9:4511
55. Connolly T, Rapiejko PJ, Gilmore R (1991) Science 252:1171
56. Egea PF et al (2004) Nature 427:215
57. Peluso P et al (2000) Science 288:1640
58. Powers T, Walter P (1995) Science 269:1422
59. Cleverley RM, Gierasch LM (2002) J Biol Chem 277:46763
60. Bourne HR, Sanders DA, Mccormick F (1991) Nature 349:117
61. Gawronski-Salerno J, Coon JSV, Focia PJ, Freymann DM (2007) Proteins 66:984
62. Focia PJ, Gawronski-Salerno J, Coon JS, Freymann DM (2006) J Mol Biol 360:631
63. Freymann DM, Keenan RJ, Stroud RM, Walter P (1999) Nat Struct Biol 6:793
64. Freymann DM, Keenan RJ, Stroud RM, Walter P (1997) Nature 385:361
65. Gu SQ et al (2005) RNA Publ RNA Soc 11:1374
66. Siu FY, Spanggord RJ, Doudna JA (2007) RNA 13:240
67. Sagar MB, Lucast L, Doudna JA (2004) RNA 10:772
68. Brown S, Fournier MJ (1984) J Mol Biol 178:533
69. Jagath JR et al (2001) RNA Publ RNA Soc 7:293
70. Poritz MA, Strub K, Walter P (1988) Cell 55:4
71. Poritz MA et al (1990) Science 250:1111
72. Batey RT, Sagar MB, Doudna JA (2001) J Mol Biol 307:229
73. Hainzl T, Huang S, Sauer-Eriksson AE (2007) Proc Natl Acad Sci U S A 104:14911
74. Stroud RM, Walter P (1999) Curr Opin Struct Biol 9:754
75. Spanggord RJ, Siu F, Ke AL, Doudna JA (2005) Nat Struct Mol Biol 12:1116
76. Mandon EC, Jiang Y, Gilmore R (2003) J Cell Biol 162:575
77. Buskiewicz I et al (2005) J Mol Biol 351:417
78. Rapiejko PJ, Gilmore R (1992) J Cell Biol 117:493
79. Zopf D, Bernstein HD, Walter P (1993) J Cell Biol 120:1113
80. Jagath JR, Rodnina MV, Wintermeyer W (2000) J Mol Biol 295:745
81. Padmanabhan S, Freymann DM (2001) Structure 9:859
82. Ramirez UD et al (2002) J Mol Biol 320:783
83. Focia PJ, Alam H, Lu T, Ramirez UD, Freymann DM (2004) Proteins 54:222
84. Lakowicz JR (1999) Principles of fluorescence spectroscopy. Kluwer Academic Publishers, London
85. Blundell TL, Fernandez-Recio J (2006) Nature 444:279
86. Boehr DD, Wright PE (2008) Science 320:1429
87. Schreiber G, Haran G, Zhou HX (2009) Chem Rev 109:839
88. Ubbink M (2009) FEBS Lett 583:1060

89. Janin J (1997) Proteins 28:153
90. Koshland DE (1958) Proc Natl Acad Sci U S A 44:98
91. Ma B, Kumar S, Tsai CJ, Nussinov R (1999) Protein Eng 12:713
92. Iwahara J, Clore GM (2006) Nature 440:1227
93. Tang C, Iwahara J, Clore GM (2006) Nature 444:383
94. Volkov AN, Worrall JA, Holtzmann E, Ubbink M (2006) Proc Natl Acad Sci U S A 103:18945
95. Tang C, Schwieters CD, Clore GM (2007) Nature 449:1078–1082
96. Lange OF et al (2008) Science 320:1471
97. Tang C, Louis JM, Aniana A, Suh JY, Clore GM (2008) Nature 455:693
98. Fawzi NL, Doucleff M, Suh JY, Clore GM (2010) Proc Natl Acad Sci U S A 107:1379
99. Crowley PB, Ubbink M (2003) Acc Chem Res 36:723
100. Zhang X, Rashid R, Wang K, Shan SO (2010) Science 328:757–760
101. Crane JM, Lilly AA, Randall LL (2010) Methods Mol Biol 619:173
102. Kimura T, Lee JC, Gray HB, Winkler JR (2009) Proc Natl Acad Sci U S A 106:7834
103. Kimura T, Lee JC, Gray HB, Winkler JR (2007) Proc Natl Acad Sci U S A 104:117
104. Schreiber G, Fersht AR (1996) Nat Struct Biol 3:427
105. Baker NA, Sept D, Joseph S, Holst MJ, McCammon JA (2001) Proc Natl Acad Sci U S A 98:10037
106. Comeau SR et al (2007) Proteins 69:781
107. Moazed D, Noller HF (1989) Cell 57:585
108. Bornemann T, Jockel J, Rodnina MV, Wintermeyer W (2008) Nat Struct Mol Biol 15:494
109. Lee HC, Bernstein HD (2001) Proc Natl Acad Sci U S A 98:3471
110. Ullers RS et al (2003) J Cell Biol 161:679
111. Bonven B, Gullov K (1979) Mol Gen Genet 170:225